

12-2018

The EMAC scheme for Navier-Stokes simulations, and application to flow past bluff bodies

Sergey Charnyi

Clemson University, scharny@g.clemson.edu

Follow this and additional works at: https://tigerprints.clemson.edu/all_dissertations

Recommended Citation

Charnyi, Sergey, "The EMAC scheme for Navier-Stokes simulations, and application to flow past bluff bodies" (2018). *All Dissertations*. 2243.

https://tigerprints.clemson.edu/all_dissertations/2243

This Dissertation is brought to you for free and open access by the Dissertations at TigerPrints. It has been accepted for inclusion in All Dissertations by an authorized administrator of TigerPrints. For more information, please contact kokeefe@clemson.edu.

THE EMAC SCHEME FOR NAVIER-STOKES SIMULATIONS, AND APPLICATION TO FLOW PAST BLUFF BODIES

A Thesis
Presented to
the Graduate School of
Clemson University

In Partial Fulfillment
of the Requirements for the Degree
Doctor of Philosophy
Mathematical sciences

by
Sergey Charnyi
December 2018

Accepted by:
Dr. Leo Rebholz, Committee Chair
Dr. Timo Heister, co-chair
Dr. Qingshan Chen
Dr. Fei Xue

ABSTRACT

The Navier-Stokes equations model the evolution of water, oil, and air flow (air under 220 m.p.h.), and therefore the ability to solve them is important in a wide array of engineering design problems. However, analytic solution of these equations is generally not possible, except for a few trivial cases, and therefore numerical methods must be employed to obtain solutions. In the present dissertation we address several important issues in the area of computational fluid dynamics.

The first issue is that in typical discretizations of the Navier-Stokes equations such as the mixed finite element method, the conservation of mass is enforced only weakly, and this leads to discrete solutions which may not conserve energy, momentum, angular momentum, helicity, or vorticity, even though the physics of the Navier-Stokes equations dictate that they do. It is widely believed in the computational fluid dynamics community that the more physics is built into the discretization, the more accurate and stable the discrete solutions are, especially over longer time intervals. In chapter 3 we study conservation properties of Galerkin methods for the incompressible Navier-Stokes equations, without the divergence constraint strongly enforced. We show that none of the commonly used formulations (*convective*, *conservative*, *rotational*, and *skew-symmetric*) conserve each of energy, momentum, and angular momentum (for a general finite element choice). We aim to construct discrete formulations that conserve as many physical laws as possible without utilizing a strong enforcement of the divergence constraint, and doing so leads us to a new formulation that conserves each of energy, momentum, angular momentum, enstrophy in 2D, helicity and vorticity (for reference, the usual convective formulation does not conserve most of these quantities). In chapter 3 we also perform a number of numerical experiments, which verify the theory and test the new formulation.

To study the performance of our novel formulation of the Navier-Stokes equations, we need reliable reference solutions/statistics. However, there is not a significant amount of reliable reference solutions for the Navier-Stokes equations in the literature. Accurate reference solutions/statistics

are difficult to obtain due to a number of reasons. First, one has to use several millions of degrees of freedom even for a two-dimensional simulation (for 3D one needs at least tens of millions of degrees of freedom). Second, it usually takes a long time before the flow becomes fully periodic and/or stationary. Third, in order to obtain reliable solutions, the time step must be very small. This results in a very large number of time steps. All of this results in weeks of computational time, even with the highly parallel code and efficient linear solvers (and in months for a single-threaded code). Finally, one has to run a simulation for multiple meshes and time steps in order to show the convergence of solutions. In the second chapter we perform a careful, very fine discretization simulations for a channel flow past a flat plate. We derive new, more precise reference values for the averaged drag coefficient, recirculation length, and the Strouhal number from the computational results. We verify these statistics by numerical computations with the three time stepping schemes (BDF2, BDF3 and Crank-Nicolson). We carry out the same numerical simulations independently using deal.II and Freefem++ software. In addition both deal.II/ Q_2Q_1 and Freefem/ P_2P_1 element types were used to verify the results. We also verify results by numerical simulations with multiple meshes, and different time step sizes.

Finally, in chapter 4 we compute reference values for the three-dimensional channel flow past a circular cylinder obstacle, with both time-dependent inflow and with constant inflow using up to *70.5 million degrees of freedom*. In contrast to the linearization approach used in chapter 2, in chapter 4 we numerically study *fully nonlinear schemes*, which we linearize using Newton's method. In chapter 4 we also compare the performance of our novel EMAC scheme with the four most commonly used formulations of the Navier-Stokes equations (rotational, skew-symmetric, convective and conservative) for the three-dimensional channel flow past circular cylinder both with the time-dependent inflow and with constant inflow.

Table of Contents

Title Page	i
ABSTRACT	ii
List of Tables	vi
List of Figures	vi
1 Introduction	1
1.1 Navier-Stokes equations	2
1.1.1 Reynolds number	3
1.1.2 Navier-Stokes equations derivation	3
1.1.3 Kolmogorov results	8
1.1.4 NSE Conservation laws	8
1.2 Improved physics in discretizations	13
1.2.1 Problems with standard schemes	14
1.3 Reference solutions	15
1.4 Thesis structure	16
2 Reference values for drag, recirculation point and Strouhal number of a two-dimensional time-dependent flow past vertical flat plate	18
2.1 Introduction	18
2.2 The test problem	18
2.3 Discretization details	20
2.4 The temporal-spatial discretizations	22
2.5 Statistics of interest	24
2.5.1 Drag	24
2.5.2 Recirculation length	24
2.5.3 Strouhal number	24
2.6 Averaging interval	25
2.7 Numerical simulations	26
2.8 Computational Results	26
2.8.1 Reynolds number 50	27
2.8.2 Reynolds number 100	30
2.8.3 Reynolds number 150	34
2.9 Evaluation of the computational results	40
2.10 Summary	40
3 Energy, momentum and angular momentum conserving formulation	42
3.1 Notation and preliminaries	44
3.2 Conservation properties and the EMA formulation for Navier-Stokes	46
3.2.1 Energy, momentum and angular momentum	48
3.2.2 Discussion	54

3.3	Numerical Experiments	54
3.3.1	Gresho Problem	56
3.3.2	Channel flow around a cylinder	58
3.3.3	Channel flow past a flat plate	61
3.4	Conclusions	63
4	3D Channel Flows Past Cylinder	64
4.1	The test problem	64
4.2	Statistics of interest	65
4.3	Sine inflow past circular cylinder	65
4.3.1	Newton method derivation	67
4.3.2	Discretization details	69
4.3.3	Reference values from literature for sine inflow	72
4.3.4	Computational results for sine inflow	72
4.3.5	Summary	89
4.4	Constant inflow past circular cylinder	90
4.4.1	Computational results	91
4.4.2	Summary	102
	Bibliography	106

List of Tables

2.1	Reynolds number 50 results.	28
2.2	Reynolds number 100 results	31
2.3	Reynolds number 150 results	34
2.5	Statistics for Reynolds numbers 50, 100, 150 obtained with 4 million DOF space resolution, with (Q_2, Q_1) finite element.	40
3.1	Cylinder problem results.	60
3.2	Flat plate problem results.	63
4.1	Reference values from literature for 3D-3Z case	73
4.2	Statistics for the 5 formulations. 23.5 million mesh DOF	73
4.3	Statistics for the 5 formulations. 7.42 million mesh DOF	74
4.4	Statistics for the rotational formulation. Part 1	74
4.5	Statistics for the rotational formulation. Part 2	74
4.6	Statistics for the skew-symmetric formulation. Part 1	75
4.7	Statistics for the skew-symmetric formulation. Part 2	75
4.8	Statistics for the convective formulation. Part 1	76
4.9	Statistics for the convective formulation. Part 2	76
4.10	Statistics for the conservative formulation. Part 1	76
4.11	Statistics for the conservative formulation. Part 2	77
4.12	Statistics for the EMAC formulation. Part 1	77
4.13	Statistics for the EMAC formulation. Part 2	78
4.14	EMAC statistics for 1, 2, and ‘as many as necessary’ Newton steps take at each time steps	87
4.15	Statistics for the 5 formulations, 22.5 million mesh DOF	88
4.16	Statistics for the 5 formulations. 22.4 million DOF	91
4.17	Statistics for the 5 formulations, 7.2 million DOF	91
4.18	Statistics for the conservative formulation	92
4.19	Statistics for the EMAC formulation	92
4.20	Statistics for the rotational formulation	93
4.21	Statistics for the skew-symmetric formulation	93
4.22	Interval obtained with 5 formulations, where the nonlinear problem is fully resolved at each time step. 22.4 million mesh DOF. $\Delta t = 0.005$	102

List of Figures

2.1	Channel and Boundary Conditions	20
2.2	Mesh around the flat plate in Freefem++.	21
2.3	Mesh of the whole channel in Freefem++.	22
2.4	Drag for 290K DOF mesh, Reynolds 50.	29
2.5	Averaged velocity figure for Reynolds number 50	29
2.6	Strouhal number for 4M DOF mesh, Reynolds 50.	30
2.7	Drag for 4M DOF mesh, Reynolds 100.	32
2.8	Averaged velocity for 290K DOF mesh, Reynolds 100.	32
2.9	Strouhal number for 4M DOF mesh, Reynolds 100.	33
2.10	Average velocity for 290K DOF mesh, Reynolds 150.	35
2.11	Drag for 4M DOF mesh, Reynolds 150.	35
2.12	Strouhal number for 2M DOF mesh, Reynolds 150.	36
3.1	True velocity solution for the Gresho problem	56
3.2	Gresho problem plots	59
3.3	Channel flow around a cylinder domain, resolved velocity field	60
3.4	Setup for the flow past a normal flat plate.	62
4.1	The channel with the circular cylinder.	64
4.2	Mesh generated with Gmsh software on midplane.	69
4.3	Mesh generated with Gmsh software, around circular cylinder.	70
4.4	Coarse 2D mesh.	70
4.5	3D mesh after extrusion.	71
4.6	Refined mesh on midplane around the circular cylinder.	71
4.7	Refined mesh on midplane around the circular cylinder (closer to the cylinder).	72
4.8	The drag coefficient in time for the EMAC scheme, $\Delta t = 0.005$	78
4.9	The lift coefficient in time for the EMAC scheme, $\Delta t = 0.005$	79
4.10	Pressure drop in time for the EMAC scheme, $\Delta t = 0.005$	79
4.11	Kinetic Energy in time for the EMAC scheme, $\Delta t = 0.005$	80
4.12	Linear Momentum in time for the EMAC scheme, $\Delta t = 0.005$	81
4.13	Angular Momentum in time for the EMAC scheme, $\Delta t = 0.005$	81
4.14	The maximum drag coefficient figure	82
4.15	The maximum lift coefficient figure	83
4.16	Maximum pressure drop figure	83
4.17	Minimum lift figure	84
4.18	Vorticity iso-contours with streamlines	85
4.19	Pressure iso-contours in 3D	85

4.20	Velocity magnitude iso-contours on midplane	86
4.21	Pressure iso-contours on midplane.	86
4.22	The drag coefficient for all schemes, start time $T = 0$	94
4.23	The drag coefficient for all 5 schemes, start time $T = 1$	94
4.24	The lift coefficient for all 5 schemes, start time $T = 0$	95
4.25	The lift coefficient for all 5 schemes, start time $T = 1$	96
4.26	Pressure drop for all 5 schemes, start time $T = 0$	96
4.27	Pressure drop for all 5 schemes, start time $T = 1$	97
4.28	The drag coefficient figure	98
4.29	The lift coefficient figure	98
4.30	Pressure drop figure	99
4.31	Vorticity iso-contours with streamlines	100
4.32	Pressure iso-contours in 3D	101
4.33	Velocity magnitude iso-contours on midplane	101
4.34	Pressure iso-contours on midplane at $T = 5$ sec.	102

Chapter 1

Introduction

The ability to efficiently and accurately perform simulations of fluids is important in a wide array of engineering design problems, including model/design selection (e.g. car and airplane design, tire design), weather prediction, polymerization, crystallization, blood flow simulation, ocean currents, plasma physics, nuclear reactors, astrophysics, fluid flows in pipes and channels, blood flow in arteries, and in the petroleum industry.

However, experimental simulations of fluids are usually time-consuming and expensive. Consider for example an airflow simulation around an airplane in a wind tunnel. An airplane model of a real size is expensive, takes a long time to build, and requires a wind tunnel that is many times larger than the airplane model, so that the walls of the tunnel do not affect the results of a simulation. Another approach is to use a small airplane model, but in this case one has to reach a much faster air speed than the regular speed of an airplane in order to obtain the correct Reynolds number, which is usually not possible to achieve with air [31].

Numerical simulations of fluid and gas allow savings of money and time in many engineering design problems. On the other hand, an accurate numerical simulation is still very challenging. Kolmogorov in 1941 showed [30] that the smallest stable eddy has length scale of order $O(Re^{-\frac{3}{4}})$. For example, Reynolds number for a subcompact car is $\approx 6 \times 10^5$ [31], therefore one needs the order of 10^{12} degrees of freedom to fully resolve such a numerical simulation. This in its turn requires solving a nonsymmetric system of linear equations with the order of 10^{12} unknowns, which is not feasible at the present time.

1.1 Navier-Stokes equations

The equations that govern the evolution of an incompressible, Newtonian fluid are the Navier-Stokes equations (**NSE**). Let u denote fluid velocity, and p denote pressure. Let ν be the kinematic viscosity, and f be the external force. In the dimensionless form, the NSE read:

$$\begin{aligned} u_t + u \cdot \nabla u + \nabla p - \nu \Delta u &= f, \\ \nabla \cdot u &= 0. \end{aligned} \tag{1.1}$$

The first equation of (1.1) is the momentum equation, and represents the conservation of linear momentum. The second equation of (1.1) is the conservation of mass equation, which is also called the continuity equation or the incompressibility constraint. The NSE models, for example, the evolution of water, oil, and air flow (air under 220 m.p.h.). However, analytic solutions of these equations is generally not possible, except for a few trivial cases, and therefore numerical methods must be employed to obtain solutions. Despite significant developments in the numerical methods and computer hardware, the numerical solution of the NSE is still very challenging, especially for high Reynolds numbers.

The NSE were derived in the nineteenth century, and have been studied by many scientists [23, 31, 36, 51]. However, even the theory of analytical solutions for the NSE is incomplete. It is an open question whether strong solutions of the NSE exist in three dimensions; if they exist, their regularity is not known. The Clay Mathematics Institute offers US \$1 million prize for a proof or a counterexample [19]. On the other hand, it was shown that weak solution exist, but there is no proof of their uniqueness.

The NSE conserves many physical quantities, including kinetic energy, linear momentum, and angular momentum. However, finite element discretizations of the NSE do not conserve all of these quantities, if any (usually energy only). There is a long history of numerical methods for the NSE that better obey physical laws to give more accurate solutions in any measure. We discuss this in chapter 3.

This thesis is a study of a novel finite element scheme for the incompressible NSE, which

conserves kinetic energy, linear momentum and angular momentum, even when the divergence-free condition is only weakly enforced, and independently of the choice of finite elements.

1.1.1 Reynolds number

The Reynolds number is defined as the ratio of the inertial forces to viscous forces:

$$Re = \frac{\text{inertial forces}}{\text{viscous forces}} = \frac{vL}{\nu}, \quad (1.2)$$

where v is the maximum velocity of the fluid, L is a characteristic linear dimension, ν is the kinematic viscosity ($\nu = \frac{\mu}{\rho}$), μ is the dynamic viscosity of the fluid, and ρ is fluid density.

1.1.2 Navier-Stokes equations derivation

We denote the usual $L^2(\Omega)$ norm and its inner product by $\|\cdot\|$ and (\cdot, \cdot) respectively. For the derivation of the NSE, we will use the following theorem.

Theorem 1 (Divergence Theorem). *Let F be a differentiable vector field in domain $\Omega \subset \mathbb{R}^3$ with smooth boundary $\partial\Omega$. Then*

$$\int_{\Omega} (\nabla \cdot F) \, dx = \int_{\partial\Omega} F \cdot n \, ds. \quad (1.3)$$

1.1.2.1 Derivation of the conservation of mass equation

Let V be an arbitrary chosen control volume in domain $\Omega \subset \mathbb{R}^3$ with a smooth surface ∂V . According to the Eulerian approach, the velocity of the fluid and its mass density are defined as functions of time t and space x . Then, the total mass in the control volume is

$$m(t) = \int_V \rho(t, x) \, dx, \quad (1.4)$$

and the rate of change of mass in Ω is given by

$$\frac{dm(t)}{dt} = \frac{d}{dt} \int_V \rho(t, x) \, dx = \int_V \frac{\partial \rho(t, x)}{\partial t} \, dx. \quad (1.5)$$

The physical law of conservation of mass is that for any system closed to all transfers of matter and energy, the mass of the system must remain constant over time. Since mass is conserved inside the control volume V , the rate of change of mass in V is equal to the flux of mass $\rho u(t, x)$ across the boundary ∂V . Therefore, we obtain

$$\frac{dm(t)}{dt} = - \int_{\partial V} (\rho u)(t, s) \cdot n(s) ds. \quad (1.6)$$

Now use (1.5) and apply the divergence theorem to the right hand side, which gives

$$\int_V \left(\nabla \cdot (\rho u)(t, x) + \frac{\partial \rho(t, x)}{\partial t} \right) dx = 0. \quad (1.7)$$

Since the control volume V is arbitrary, we obtain

$$\nabla \cdot (\rho u) + \frac{\partial \rho}{\partial t} = 0, \forall (t, x) \in (0, T] \times \Omega. \quad (1.8)$$

Since we assume the fluid is homogeneous and incompressible, the mass density is constant and the continuity equation follows:

$$\nabla \cdot u = 0 \text{ in } (0, T] \times \Omega. \quad (1.9)$$

1.1.2.2 Derivation of the Conservation of Linear Momentum Equation

Denote the position of a fluid particle and its velocity at time t as follows,

$$\begin{aligned} x &= (x(t), y(t), z(t)), \\ u &= (u_1(x(t), y(t), z(t)), u_2(x(t), y(t), z(t)), u_3(x(t), y(t), z(t))). \end{aligned}$$

The linear momentum in a control volume V is

$$\int_V (\rho u)(t, x) dx.$$

Let $F_{net}(t, x)$ be the net force acting on the fluid, and $F_{ext}(t, x)$ be the body (external) forces. Newton's second law states that the rate of change of linear momentum inside V is equal to the net force acting on the fluid [13]. Applying it to control volume V , we obtain

$$\frac{d}{dt}(\rho u)(t, x) = - \int_{\partial V} (\rho u)(u \cdot n)(t, s) ds + \int_V F_{net}(t, x) dx. \quad (1.10)$$

Now apply the divergence theorem to the first term on the right hand side of (1.10), and using the following equation

$$u(u \cdot n) = \begin{pmatrix} u_1 \\ u_2 \\ u_3 \end{pmatrix} (u_1 n_1 + u_2 n_2 + u_3 n_3) = \begin{pmatrix} u_1^2 n_1 + u_1 u_2 n_2 + u_1 u_3 n_3 \\ u_2 u_1 n_1 + u_2^2 n_2 + u_2 u_3 n_3 \\ u_3 u_1 n_1 + u_3 u_2 n_2 + u_3^2 n_3 \end{pmatrix} = uu^T n, \quad (1.11)$$

we obtain

$$\int_V \left[\frac{\partial}{\partial t}(\rho u) + \nabla \cdot (\rho uu^T)(t, x) \right] dx = \int_V F_{net}(t, x) dx. \quad (1.12)$$

Since the fluid is incompressible, and by the product rule, we have

$$\begin{aligned} \nabla \cdot (\rho uu^T) &= uu^T \nabla \rho + \rho(\nabla \cdot u)u + \rho(u \nabla \cdot)u = \rho(u \nabla \cdot)u, \\ \frac{\partial}{\partial t}(\rho u) &= \frac{\partial \rho}{\partial t}u + \rho \frac{\partial u}{\partial t} = \rho \frac{\partial u}{\partial t}. \end{aligned} \quad (1.13)$$

Now from (1.13) and (1.12), it follows that

$$\int_V \rho \left[\frac{\partial u}{\partial t} + (u \cdot \nabla)u \right] (t, x) dx = \int_V F_{net}(t, x) dx. \quad (1.14)$$

The net force acting on the fluid inside control volume is a sum of internal forces and body (external) forces, therefore

$$\int_V F_{net}(t, x) dx = \int_V F_{ext}(t, x) dx + \int_{\partial V} \vec{t}(t, x) dx. \quad (1.15)$$

Let \vec{t} denote the Cauchy stress vector (internal force vector), σ_{ii} the normal stress tensor, τ_{ij} the shear stresses, and by \mathbb{S} the Cauchy stress vector that is defined as:

$$\mathbb{S} = \begin{pmatrix} \sigma_{11} & \tau_{12} & \tau_{13} \\ \tau_{21} & \sigma_{22} & \tau_{23} \\ \tau_{31} & \tau_{32} & \sigma_{33} \end{pmatrix}, \tau_{ij} = \tau_{ji}; \quad i, j = 1, 2, 3 \quad (i \neq j). \quad (1.16)$$

Then from the assumed linear dependence of Cauchy stress vector it follows that

$$\mathbb{S}n = \vec{t}. \quad (1.17)$$

Let P be the pressure, and \mathbb{V} be viscous stress tensor. Then Cauchy stress tensor can be decomposed as

$$\mathbb{S} = \mathbb{S} - P\mathbb{I}. \quad (1.18)$$

Since pressure P acts on a surface of control volume V , directed into the control volume, and normal to the surface, we obtain

$$-\int_{\partial V} P n ds = -\int_V \nabla P dx = -\int_V \nabla \cdot (P\mathbb{I}) dx. \quad (1.19)$$

Let $D(u)$ denote velocity deformation tensor, $D(u) := \frac{\nabla u + (\nabla u)^T}{2}$. Let μ be the first order viscosity (also called dynamic viscosity or shear viscosity). We consider incompressible ($\nabla \cdot u = 0$), Newtonian fluids, for which viscous stress tensor is given by

$$\mathbb{V} = 2\mu D(u). \quad (1.20)$$

Therefore, using the divergence theorem, we obtain

$$\begin{aligned}
\int_{\partial V} \vec{t}(t, s) ds &= \int_{\partial V} (\mathbb{S}n)(t, s) ds \\
&= \int_V (\nabla \cdot S) dx = \int_V \nabla \cdot (2\mu D(u)) dx - \int_V \nabla \cdot (P\mathbb{I}) dx \\
&= \int_V \nabla \cdot (2\mu D(u)) dx - \int_V \nabla P dx.
\end{aligned} \tag{1.21}$$

Since the flow is incompressible, and μ is constant, from the definition of deformation tensor it follows that

$$\begin{aligned}
\nabla \cdot (2\mu D(u)) &= \nabla \cdot \left(2\mu \frac{\nabla u + (\nabla u)^T}{2} \right) = \mu \nabla \cdot (\nabla u + (\nabla u)^T) \\
&= \mu \nabla \cdot (\nabla u) + \mu \nabla \cdot (\nabla u)^T = \mu \Delta u.
\end{aligned} \tag{1.22}$$

From (1.21) and the last equation we obtain

$$\int_{\partial V} \vec{t}(t, s) ds = \int_V \mu \Delta dx - \int_V \nabla P dx. \tag{1.23}$$

Now substitute (1.23) into (1.15), and then substitute (1.15) into (1.14). Equation (1.14) becomes

$$\int_V \left(\rho \left[\frac{\partial u}{\partial t} + (u \cdot \nabla)u \right] - \mu \Delta u + \nabla P \right) (t, x) dx = \int_V F_{ext}(t, x) dx. \tag{1.24}$$

Since the control volume is arbitrary, the subintegral functions must be equal as well

$$\rho \left[\frac{\partial u}{\partial t} + (u \cdot \nabla)u \right] - \mu \Delta u + \nabla P = F_{ext} \text{ in } (0, T] \times \Omega. \tag{1.25}$$

Now divide both sides by ρ , and denote by $p := \frac{P}{\rho}$ and $f := \frac{F_{ext}}{\rho}$:

$$\frac{\partial u}{\partial t} + (u \cdot \nabla)u - \frac{\mu}{\rho} \Delta u + \nabla p = f \text{ in } (0, T] \times \Omega. \tag{1.26}$$

Equation (1.26) together with (1.9) gives the NSE for unsteady flow of Newtonian, incompressible, viscous fluid:

$$\frac{\partial u}{\partial t} + (u \cdot \nabla)u - \nu \Delta u + \nabla p = f, \quad (1.27)$$

$$\nabla \cdot u = 0, \quad (1.28)$$

in $(0, T] \times \Omega$. The equation (1.27) is called the momentum equation. The second equation (1.28) is the continuity equation, which is also called the incompressibility constraint or conservation of mass equation.

1.1.3 Kolmogorov results

It was discovered by Kolmogorov in 1941 [30] (and further analyzed in [32]) that for large Reynolds numbers, the smallest stable eddy has length scale of order $O(Re^{-\frac{3}{4}})$. Therefore for a numerical simulation to capture the smallest possible eddy, one needs to choose a mesh that satisfies the following conditions,

$$\Delta x = \Delta y = \Delta z = O(Re^{-\frac{3}{4}}).$$

Hence the number of mesh points in a 3D simulation must be of the order $Re^{9/4}$ in order to capture all the physics.

1.1.4 NSE Conservation laws

It is well-known that the NSE conserve kinetic energy ($E = \frac{1}{2} \int_{\Omega} |u|^2 dx$), linear momentum ($M := \int_{\Omega} u dx$) and angular momentum ($M_x := \int_{\Omega} (u \times x) dx$), when viscosity is zero and there is no external force. We now derive conservation laws for the NSE at the continuous level, assuming $u = 0$ in a strip along $\partial\Omega$.

1.1.4.1 Linear momentum

Integrating the momentum equation over Ω gives

$$\int_{\Omega} u_t \, dx + \int_{\Omega} u \cdot \nabla u \, dx + \int_{\Omega} \nabla p \, dx - \nu \int_{\Omega} \Delta u \, dx = \int_{\Omega} f \, dx. \quad (1.29)$$

Since $\nabla \cdot u = 0$, and by Green's theorem

$$\int_{\Omega} u \cdot \nabla u \, dx = \int_{\Omega} \nabla \cdot (uu) \cdot 1 \, dx = -(uu, \nabla 1) + \int_{\partial\Omega} (uu \cdot n) \cdot 1 \, ds = 0. \quad (1.30)$$

By Green's theorem and since $u = 0$ along $\partial\Omega$

$$\int_{\Omega} \Delta u \, dx = (\Delta u, 1) = (\nabla u, \nabla 1) - \int_{\partial\Omega} ((\nabla u) \cdot n) \cdot 1 \, ds = 0. \quad (1.31)$$

By Green's theorem and since $p = 0$ along $\partial\Omega$

$$\int_{\Omega} \nabla p \, dx = (\nabla p, 1) = -(p, \nabla \cdot 1) + \int_{\partial\Omega} p(1 \cdot n) \, ds = 0. \quad (1.32)$$

Therefore

$$\frac{d}{dt} \int_{\Omega} u \, dx = \int_{\Omega} f \, dx. \quad (1.33)$$

If $\int_{\Omega} f \, dx = 0$, then linear momentum is conserved:

$$\int_{\Omega} u(T) \, dx = \int_{\Omega} u(0) \, dx. \quad (1.34)$$

1.1.4.2 Kinetic Energy

Kinetic energy is defined as $E = \frac{1}{2}(u, u) := \frac{1}{2} \int_{\Omega} |u|^2 \, dx$. Multiply the NSE momentum equation by u and integrate it over Ω , then use Green's theorem:

$$(u_t, u) + (u \cdot \nabla u, u) + (\nabla p, u) + \nu \|\nabla u\|^2 = (f, u). \quad (1.35)$$

By Green's theorem

$$(\nabla p, u) = -(p, \nabla \cdot u) + \int_{\partial\Omega} p(u \cdot n) ds.$$

Since $\nabla \cdot u = 0$, and we assume $u = 0$ on the boundary, then $(\nabla p, u) = 0$. Since

$$(u \cdot \nabla u, u) = -\frac{1}{2}((\operatorname{div} u)u, u) = 0,$$

we obtain from (1.35) that

$$\frac{1}{2} \frac{d}{dt} \|u\|^2 + \nu \|\nabla u\|^2 = (f, u). \quad (1.36)$$

Kinetic energy is thus preserved for $\nu = 0$ and $f = 0$, that is

$$\frac{1}{2} \|u(T)\|^2 = \frac{1}{2} \|u(0)\|^2. \quad (1.37)$$

1.1.4.3 Angular Momentum

Angular momentum is defined as $M_x := \int_{\Omega} u \times x \, dx$. Let $\phi_i(x) := x \times e_i$, $i = 1, 2, 3$.

Multiply the NSE by ϕ_i , for $i = 1, 2, 3$ and integrate it over Ω :

$$(u_t, \phi_i) + (u \cdot \nabla u, \phi_i) + (\nabla p, \phi_i) - \nu(\Delta u, \phi_i) = (f, \phi_i). \quad (1.38)$$

Using Green's theorem and that $u = 0$ along $\partial\Omega$, we show

$$(\nabla p, \phi_i) = - \int_{\Omega} p \cdot (\nabla \cdot \phi_i) \, dx = - \int_{\Omega} p \cdot (\nabla \cdot (x \times e_i)) \, dx. \quad (1.39)$$

Using the identity

$$\nabla \cdot (A \times B) = (\operatorname{curl} A) \cdot B - A \cdot (\operatorname{curl} B), \quad (1.40)$$

we obtain

$$\nabla \cdot (x \times e_i) = (\operatorname{curl} x) \cdot e_i - x \cdot (\operatorname{curl} e_i) = 0. \quad (1.41)$$

because e_i is constant vector, and $\text{curl } x = 0$. For the nonlinear term, we use the following identity:

$$b(u, u, \phi_i) = -((\text{div } u)u, \phi_i). \quad (1.42)$$

Using $\text{div } u = 0$, we obtain

$$(u \cdot \nabla u, \phi_i) := b(u, u, \phi_i) = -((\text{div } u)u, \phi_i) = 0. \quad (1.43)$$

Since both viscosity and external force affect angular momentum, assume $\nu = 0$ and $(f, \phi_i) = 0$, we obtain from (1.38):

$$\left(\frac{\partial u}{\partial t}, \phi_i \right) = 0, \quad i = 1, 2, 3.$$

But since also

$$\left(\frac{\partial u}{\partial t}, \phi_i \right) = \frac{\partial u}{\partial t} [(M_x)_i], \quad i = 1, 2, 3, \quad (1.44)$$

angular momentum is conserved.

1.1.4.4 Helicity

Helicity is defined as $H = (u, \text{curl } u)$. Now we show that helicity is conserved by the NSE. Assuming sufficient smoothness of u and p , we obtain

$$\begin{aligned} \frac{dH}{dt} &= \int_{\Omega} \frac{d}{dt} (u \cdot \text{curl } u) \, dx = \int_{\Omega} \frac{\partial}{\partial t} (u \cdot \text{curl } u) \, dx \\ &= \int_{\Omega} \frac{\partial u}{\partial t} \cdot \text{curl } u \, dx + \int_{\Omega} u \cdot \frac{\partial}{\partial t} (\text{curl } u) \, dx. \end{aligned} \quad (1.45)$$

Since curl involves only spatial derivatives, we can exchange the order of time derivative and curl , and use the fact that curl is self-adjoint operator, we obtain

$$\int_{\Omega} u \cdot \frac{\partial}{\partial t} (\text{curl } u) \, dx = \int_{\Omega} u \cdot \text{curl} \left(\frac{\partial u}{\partial t} \right) \, dx = \left(u, \text{curl} \left(\frac{\partial u}{\partial t} \right) \right) = \left(\text{curl } u, \frac{\partial u}{\partial t} \right). \quad (1.46)$$

From (1.45) and (1.46) it follows that

$$\frac{dH}{dt} = 2 \left(\operatorname{curl} u, \frac{\partial u}{\partial t} \right). \quad (1.47)$$

Multiply the NSE momentum equation by $\operatorname{curl} u$ and integrate it over Ω :

$$(u_t, \operatorname{curl} u) + (u \cdot \nabla u, \operatorname{curl} u) + (\nabla p, \operatorname{curl} u) - \nu(\Delta u, \operatorname{curl} u) = (f, \operatorname{curl} u). \quad (1.48)$$

We use the following identity for the nonlinear term:

$$u \cdot \nabla u = (\operatorname{curl} u) \times u + \frac{1}{2} \nabla |u|^2, \quad (1.49)$$

which provides

$$\begin{aligned} (u \cdot \nabla u, \operatorname{curl} u) &= \left((\operatorname{curl} u) \times u + \frac{1}{2} \nabla |u|^2, \operatorname{curl} u \right) \\ &= ((\operatorname{curl} u) \times u, \operatorname{curl} u) + \left(\frac{1}{2} \nabla |u|^2, \operatorname{curl} u \right). \end{aligned} \quad (1.50)$$

Since $(b \times a) \perp b = 0$ and applying Green's theorem to (1.50), we obtain

$$(u \cdot \nabla u, \operatorname{curl} u) = -\frac{1}{2}(|u|^2, \nabla \cdot (\operatorname{curl} u)) + \frac{1}{2} \int_{\partial\Omega} |u|^2 (\operatorname{curl} u) \cdot n \, ds. \quad (1.51)$$

From vector identity $\nabla \cdot (\operatorname{curl} u) = 0$, and as $u = 0$ along $\partial\Omega$, it follows that

$$(u \cdot \nabla u, \operatorname{curl} u) = 0. \quad (1.52)$$

Using Green's theorem, and as $u = 0$ and $p = 0$ along $\partial\Omega$, we obtain

$$(\nabla p, \operatorname{curl} u) = -(p, \nabla \cdot (\operatorname{curl} u)) + \int_{\partial\Omega} p (\operatorname{curl} u \cdot n) \, ds = 0. \quad (1.53)$$

Assuming no viscosity and no forcing, from (1.48) we obtain

$$\left(\frac{\partial u}{\partial t}, \operatorname{curl} u\right) = 0. \quad (1.54)$$

From (1.47) and (1.54) we obtain

$$\frac{dH}{dt} = 0. \quad (1.55)$$

Helicity is thus conserved by the NSE.

1.2 Improved physics in discretizations

It is widely believed in the computational fluid dynamics (**CFD**) community that the more physics is built into the discretization, the more accurate and stable the discrete solutions are, especially over longer time intervals. N. Phillips in 1959 [42] constructed an example for the barotropic nonlinear vorticity equation (using a finite-difference scheme), where the long-time integration of the convection terms results in a failure of numerical simulations for any time step. In [4] Arakawa showed that one can avoid instability issues with integration over long time if kinetic energy and enstrophy (in 2D) are conserved by a discretization scheme. For a two-dimensional flow, Arakawa [4] developed an energy and enstrophy conserving scheme in 1966 for the two-dimensional incompressible flows. Arakawa and Lamb in 1981 [5] introduced a scheme that conserves a potential enstrophy and kinetic energy for the shallow water equations. In 2004, Liu and Wang developed that conserves helicity and energy for three-dimensional flows. In [35], they present an energy and helicity-preserving scheme for axisymmetric flows. They also show that their dual conservation scheme eliminates the need for large nonphysical numerical viscosity. In 2007 R. Salmon [47] developed a finite-difference scheme for the shallow water equations that conserves energy, circulation, potential enstrophy and mass on an unstructured triangular mesh and on a regular square grid. In 2007 [43] a finite element scheme that conserves both energy and helicity for general, viscous flows has been developed, and in [40] it was discussed how an alternate (but equally valid) definition of helicity could be conserved by skew-symmetric formulations. In 2016 A. Palhaa and M. Gerritsma [41] presented a spectral element mimetic scheme for the two-dimensional incompressible NSE,

that preserves kinetic energy, total vorticity, mass and enstrophy on unstructured grids. Some other ‘clever’ discretizations, which ‘bring back’ conservation laws lost in standard discretizations, for the NSE and related equations can be found in [3, 17, 20, 35, 41, 48, 52].

Most finite element numerical schemes enforce global mass conservation only weakly, i.e.

$$\int_{\Omega} (\nabla \cdot u_h) q_h = 0,$$

for each q_h in a discrete pressure space Q_h . Depending on the choice of finite elements this can lead to significant disagreement with the mass conservation law [12]. It has been known for decades in CFD, that the more physical quantities are conserved by a finite element scheme, the more accurate the prediction, especially over the long time intervals. Thus the solutions provided by a more physically accurate scheme are also more physically relevant. If one could afford a fully resolved mesh and infinitely small time step, all commonly used finite element schemes are believed to provide the same numerical solutions. However, in practice one cannot afford a fully resolved mesh in 3D-simulations, especially for time-dependent problems. For example in chapter 2 we need 50-60 thousand time steps, where each time step requires solving a sparse linear system with 4 million unknowns. This required 2-3 weeks of computational time with highly parallel code on 5 nodes with 24 cores each.

We will develop in chapter 3 a scheme that is seemingly unconsidered in the literature, which conserves energy, linear momentum and angular momentum both for 2D and 3D flows for general meshes and element choices. Seemingly no commonly used schemes conserve each of these quantities. Thus we expect better accuracy, and observe it in tests.

1.2.1 Problems with standard schemes

In chapter 3 we consider these four commonly used formulations (for the case of homogeneous Dirichlet boundary conditions for simplicity):

Find $(u_h, p_h) \in (X_h, Q_h)$ such that for every $(v_h, q_h) \in (X_h, Q_h)$,

Convective formulation (CONV)

$$\begin{aligned} ((u_h)_t, v_h) + (u_h \cdot \nabla u_h, v_h) - (p_h, \operatorname{div} v_h) + \nu(\nabla u_h, \nabla v_h) &= (f, v_h), \\ (\operatorname{div} u_h, q_h) &= 0. \end{aligned}$$

Skew-symmetric formulation (SKEW)

$$\begin{aligned} ((u_h)_t, v_h) + (u_h \cdot \nabla u_h, v_h) + \frac{1}{2}((\operatorname{div} u_h)u_h, v_h) - (p_h, \operatorname{div} v_h) + \nu(\nabla u_h, \nabla v_h) &= (f, v_h), \\ (\operatorname{div} u_h, q_h) &= 0. \end{aligned}$$

Conservative formulation (CONS)

$$\begin{aligned} ((u_h)_t, v_h) + (u_h \cdot \nabla u_h, v_h) + ((\operatorname{div} u_h)u_h, v_h) - (p_h, \operatorname{div} v_h) + \nu(\nabla u_h, \nabla v_h) &= (f, v_h), \\ (\operatorname{div} u_h, q_h) &= 0. \end{aligned}$$

Rotational formulation (ROT)

$$\begin{aligned} ((u_h)_t, v_h) + ((\operatorname{curl} u_h) \times u_h, v) - (p_h, \operatorname{div} v_h) + \nu(\nabla u_h, \nabla v_h) &= (f, v_h), \\ (\operatorname{div} u_h, q_h) &= 0. \end{aligned}$$

In chapter 3 we show that *none* of the above formulations (convective, skew-symmetric, rotational, conservative), conserves all of kinetic energy, linear momentum and angular momentum. In chapter 3 we develop a novel *EMAC* scheme, which conserves all of kinetic energy, linear momentum and angular momentum.

1.3 Reference solutions

a significant amount of reliable reference solutions for the NSE in the literature. Reference values for drag and lift for two-dimensional channel flow past a cylinder are given by V. John in [28]. Three-dimensional channel flow past a circular cylinder for steady flow was suggested as

a benchmark problem by Schäfer and Turek [49], and further studied in [8, 9, 27, 38]. Results for two-dimensional channel flow past a flat plate in the literature are not reliable. The problem is considered in [46], however the precision of the statistics are low (only 3 digits are given), and it is not clear whether these statistics have converged or how many digits in the results are significant. Moreover, in [46], average drag is reported as 2.43 for Reynolds number 100, but for the same problem and Reynolds number, and by the same author in [45], average drag is reported as 2.60. We will perform a careful, much finer discretization simulation for channel flow past a flat plate in chapter 2. The reference solutions/statistics are very difficult to calculate due to a number of reasons. First, one has to use several millions of degrees of freedom even for two-dimensional simulation (for 3D one needs at least tens of millions of degrees of freedom). Second, it usually takes a long time before the flow becomes fully periodic (e.g. in the flat plate project we do not start collecting data for statistics until $T = 200$). Third, in order to obtain reliable solutions, the time step must be very small. This results in a very large number of time steps (e.g. in the flat plate project we do 50-60 thousand of iterations in time). All this results in weeks of computational time, even with a highly parallel code and efficient linear solvers (and in months for a single-threaded code). Finally, one has to run a simulation for multiple meshes and time steps in order to show the convergence of solutions.

1.4 Thesis structure

In chapter 2 we carry out large-scale numerical simulations for two-dimensional channel flow past a flat plate obstacle, and compute reliable statistics including averaged drag, recirculation point and Strouhal number for Reynolds numbers 50, 100 and 150. These statistics are used in chapter 3 to compare a novel EMAC scheme with other commonly used schemes. Furthermore, such statistics are of interest on themselves for verification of new finite element schemes as well as other numerical methods. In chapter 3 we study conservation properties of a novel finite element scheme for the NSE, which conserves kinetic energy, linear momentum and angular momentum, which we call the *EMAC* scheme. The statistics obtained in chapter 2 are used to compare the EMAC scheme with commonly used finite element schemes in chapter 3, and we also carry out several other numerical

tests.

In chapter 4 we carry out large-scale numerical simulations for three-dimensional channel flow past a circular cylinder obstacle, and compute reliable statistics including maximum and minimum drag, lift and pressure drop for Reynolds number 100. We study both time-dependent and constant-in-time inflow boundary conditions. In chapter 4 we also compare a novel EMAC scheme with other commonly used schemes.

Chapter 2

Reference values for drag, recirculation point and Strouhal number of a two-dimensional time-dependent flow past vertical flat plate

2.1 Introduction

In this chapter we calculate reference statistics for the two-dimensional time-dependent fluid flow in a channel past a vertical flat plate. These statistics can be used for verification of new models and/or discretization schemes for the incompressible NSE. As the plate has sharp corners it represents a significantly more challenging problem than the flow past a circular cylinder.

The problem is considered in [46], however the precision of the statistics are quite low (only 3 digits are given), and it is not clear whether these statistics have converged or how many digits in the results are significant. Moreover, in [46], the average drag is reported as 2.43 for Reynolds number 100, but for the same problem and Reynolds number, and by the same author in [45], average drag is reported as 2.60. Thus, we believe the flat plate problem requires additional study in order to more accurately determine these important statistics. We implemented and carried out numerical simulations using separately Freefem++ and deal.II libraries and very fine discretizations: up to 4 million spatial degrees of freedom, and time step 0.005, to obtain accurate statistics for Reynolds numbers 50, 100 and 150.

2.2 The test problem

We consider the incompressible NSE in a channel, with a constant inflow, no-slip walls, and a zero-traction outflow. The domain Ω is a box with dimensions 27×20 and flat plate obstacle has

dimensions 0.125×1 . A diagram is shown in figure 2.1. We denote Γ_w to be bottom and top walls of the channel and boundary of flat plate, Γ_{in} to be left boundary of the channel (inlet), and Γ_{out} to be the right boundary (outlet).

$$u_t - \nu \Delta u + (u \cdot \nabla)u + \nabla p = f \text{ on } (0, T] \times \Omega \quad (2.1)$$

$$\nabla \cdot u = 0 \text{ on } (0, T] \times \Omega \quad (2.2)$$

$$u(0, x) = 0 \text{ on } \Omega \quad (2.3)$$

$$(\nu \nabla u - pI) \cdot n|_{\Gamma_{out}} = 0 \text{ on } (0, T] \quad (2.4)$$

$$u|_{\Gamma_{in}} = 1 \text{ on } (0, T] \quad (2.5)$$

$$u|_{\Gamma_{walls}} = 0 \text{ on } (0, T] \quad (2.6)$$

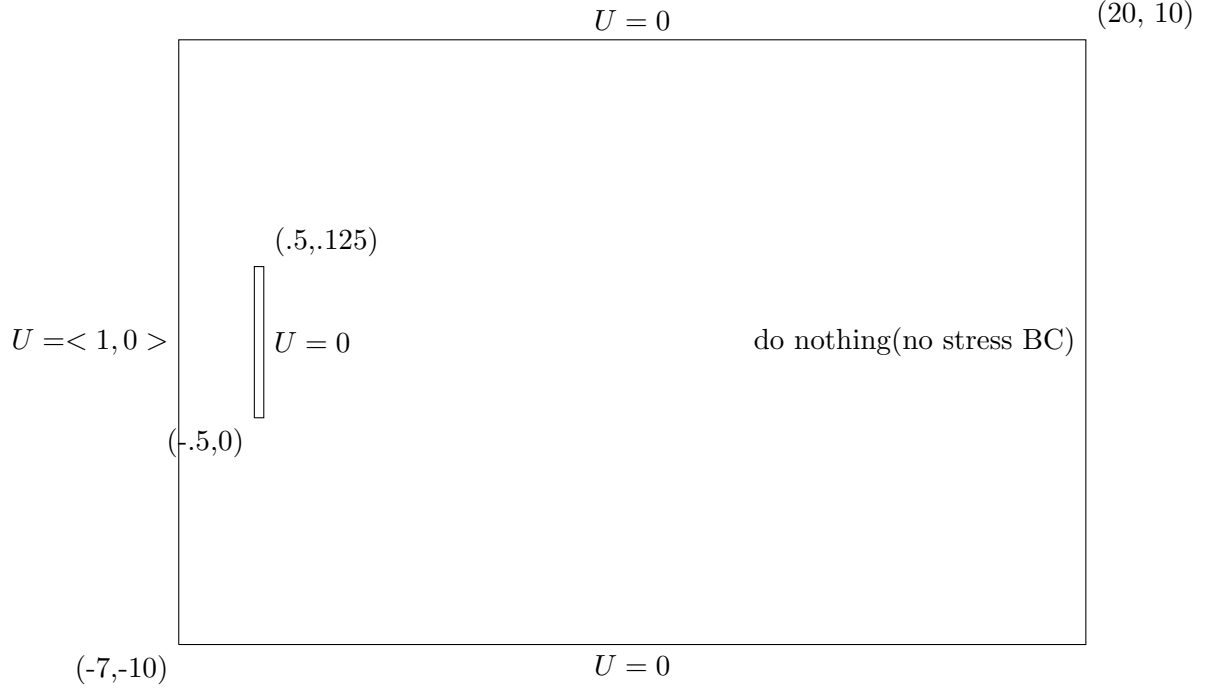
where u is velocity, p is pressure, ν is kinematic viscosity, f is external force applied to the fluid. The constant inflow comes from the left boundary. There is no stress boundary condition at the right outflow boundary and no slip boundary conditions at the walls and at the boundaries of flat plate obstacle. There is no external force on the fluid, that is, $f = 0$.

From this setup, we calculate the Reynolds number using the height of the plate L_{plate} to be

$$Re = \frac{U_{in} L_{plate}}{\nu} = \nu^{-1},$$

where U_{in} is inlet velocity. We will consider $Re = 50, 100$ and 150 .

Figure 2.1: Channel and Boundary Conditions



2.3 Discretization details

DOF stands for “number of degrees of freedom”. We denote the usual $L^2(\Omega)$ norm and its inner product by $||\cdot||$ and (\cdot, \cdot) respectively. Let τ_h be regular, conforming triangulation of the domain Ω .

We use the following notations

$$X^0(\Omega) = \{v \in (H^1(\Omega))^2 \mid v|_{\Gamma_{walls}} = 0, v|_{\Gamma_{in}} = 0\},$$

$$X(\Omega) = \{v \in (H^1(\Omega))^2 \mid v|_{\Gamma_{walls}} = 0, v|_{\Gamma_{in}} = \langle 1, 0 \rangle^T\}.$$

The natural function spaces for this problem is

$$Q := L^2(\Omega).$$

Denote conforming velocity and pressure finite element spaces, based on an edge to edge

triangulation of Ω with the maximum triangle diameter h :

$$X_h := X \cap P_k(\tau_h)$$

$$X_h^0 := X^0 \cap P_k(\tau_h)$$

$$Q_h := Q \cap P_{k-1}(\tau_h),$$

where P_k denotes degree k piecewise polynomials over triangles (on quadrilateral meshes we use Q_k and Q_{k-1} respectively).

The elements used in our simulations are the lowest order Taylor-Hood, which are the most common choices. In Freefem++, these are (P_2, P_1) on triangular meshes, and in deal.II it is (Q_2, Q_1) on quadrilateral meshes.

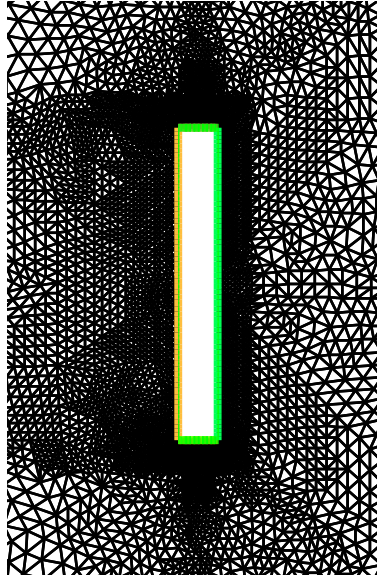


Figure 2.2: Mesh around the flat plate in Freefem++.

We use a non-uniform mesh created as follows. The mesh is refined first time in the area $x, y \in [-1, 3] \times [-2, 2]$, then mesh is refined again in a thin area around the plate. The Freefem++ results are given for meshes with 200K and 300K degrees of freedom. Figure 2.2 shows the Freefem++ mesh in a very small area around the flat plate. Figure 2.3 shows the Freefem++ mesh of the whole channel. As one can see, the mesh is very fine around the flat plate and becomes much more coarse near the channel boundaries. This is because fluid behavior is mostly complicated in a small area

around the flat plate.

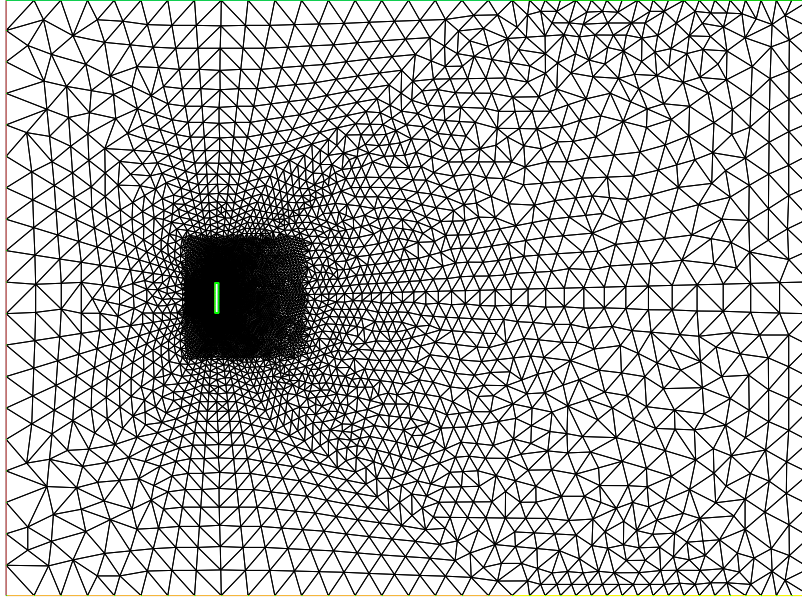


Figure 2.3: Mesh of the whole channel in Freefem++. The area around the plate looks completely black because mesh is very fine around the plate.

2.4 The temporal-spatial discretizations

The spatial discretization is constructed with finite elements, and for the temporal discretization we use (appropriately linearized) Crank-Nicolson, BDF2 and BDF3. They are defined as follows, at each time step, by:

Crank-Nicolson FEM:

Find $(u_h^{n+1}, p_h^{n+1}) \in (X_h, Q_h)$ such that

$$\begin{aligned} \frac{1}{\Delta t}(u_h^{n+1}, v_h) + ((\frac{3}{2}u_h^n - \frac{1}{2}u_h^{n-1}) \cdot \nabla u_h^{n+1}, v_h) - (p_h^{n+1}, \nabla \cdot v_h) + \frac{\nu}{2}(\nabla u_h^{n+1}, \nabla v_h) = \\ = \frac{1}{\Delta t}(u_h^n, v_h) - \frac{\nu}{2}(\nabla u_h^n, \nabla v_h) \quad \forall v_h \in X_h^0, \\ (\nabla \cdot u_h^{n+1}, q_h) = 0 \quad \forall q_h \in Q_h. \end{aligned}$$

BDF2 FEM:

Find $(u_h^{n+1}, p_h^{n+1}) \in (X_h, Q_h)$ such that

$$\begin{aligned} \frac{3}{2\Delta t}(u_h^{n+1}, v_h) + ((2u_h^n - u_h^{n-1}) \cdot \nabla u_h^{n+1}, v_h) - (p_h^{n+1}, \nabla \cdot v_h) + \nu(\nabla u_h^{n+1}, \nabla v_h) \\ + \gamma(\nabla \cdot u_h^{n+1}, \nabla \cdot v_h) = \frac{1}{2\Delta t}(4u_h^n - u_h^{n-1}, v_h) \quad \forall v_h \in X_h^0, \\ (\nabla \cdot u_h^{n+1}, q_h) = 0 \quad \forall q_h \in Q_h. \end{aligned}$$

BDF3 FEM:

Find $(u_h^{n+1}, p_h^{n+1}) \in (X_h, Q_h)$ such that

$$\begin{aligned} \frac{11}{6\Delta t}(u_h^{n+1}, v_h) + ((3u_h^n - 3u_h^{n-1} + u_h^{n-2}) \cdot \nabla u_h^{n+1}, v_h) - (p_h^{n+1}, \nabla \cdot v_h) + \nu(\nabla u_h^{n+1}, \nabla v_h) \\ + \gamma(\nabla \cdot u_h^{n+1}, \nabla \cdot v_h) = \frac{1}{\Delta t}((3u_h^n - 1.5u_h^{n-1} + \frac{1}{3}u_h^{n-2}), v_h) \quad \forall v_h \in X_h^0, \\ (\nabla \cdot u_h^{n+1}, q_h) = 0 \quad \forall q_h \in Q_h. \end{aligned}$$

We use $u_h^0 = u_h^{-1} = 0$ as the initial condition in the Freefem++ code, and a solution of the Stokes equations with the same parameters in the deal.II code. There is no forcing applied to the fluid in this problem, hence there is no forcing term ($f = 0$) in right hand side of formulations. We note that grad-div stabilization is used in the deal.II simulations, as it is an integral part of the built-in solver [26]. On fine meshes, this term has only a very minor effect on the statistics of interest. On coarse meshes (which are not our interest herein), it can have a more significant positive influence.

2.5 Statistics of interest

2.5.1 Drag

Let S denote boundaries of the flat plate, $n = (n_x, n_y)^T$ be the normal vector on S directing into Ω , $t_S = (n_y, -n_x)^T$ is the tangential vector. u_{t_S} is the tangential velocity ($u_{t_S} := t \cdot u$), where t is tangent vector to S . In reference [28], the drag coefficient is defined via the surface integral

$$c_d(t) = \frac{2}{\rho L U_{max}^2} \int_S \left(\rho \nu \frac{\partial u_{t_S}(t)}{\partial n} n_y - p(t) n_x \right) dS, \quad (2.7)$$

and for this problem, $\rho = 1$ is the density of fluid, $U_{max} = 1$ is inlet velocity and $L = 1$. Using this and converting to a global integral, the drag coefficient is defined as

$$c_d(t) = \int_{\Omega} [(u_t(t), v_d) + \nu(\nabla u(t) : \nabla v_d) + (u(t) \cdot \nabla)u(t)v_d - p(t)(\nabla \cdot v_d)] d\Omega,$$

where $v_d \in (H^1(\Omega))^2$ with $(v_d)|_S = (1, 0)^T$ and v_d vanishes on all other boundaries.

2.5.2 Recirculation length

The recirculation length is the distance from the left boundary of the flat plate to the point, where the recirculation region of the time averaged velocity behind the plate ends. This occurs, due to symmetry, along the x-axis.

2.5.3 Strouhal number

The Strouhal number is the dimensionless frequency of eddies shedding behind the plate, and can be calculated as the maximum frequency obtained by the FFT transformation of drag evolution in time. This frequency is called “primary frequency”. In case there is secondary dominant frequency, often it is called “secondary frequency” according to [45].

The data for FFT transformation is obtained from the velocity component in vertical direction at point $(4, 0)$. Note that the data should be used only after the flow gets into a periodic regime. Due to limited number of drag data-points, the frequency data obtained by FFT transformation

has finite resolution.

In [46] Strouhal number is defined as $\frac{fB}{u_{max}}$, where f is vortex shedding frequency, B is height of the plate, and u_{max} is maximum inflow velocity. In this test problem, $B = 1$, and $u_{max} = 1$.

2.6 Averaging interval

In order to compute the recirculation length and average drag statistics, one need to average velocity solutions over some time interval (we refer to such time intervals below as **averaging interval**).

The averaging interval needs to satisfy several criteria in order for calculated statistics to be reliable:

- The averaging interval should not start until fluid behavior becomes periodic, which for the problem at hand happens near time 200 seconds.
- The number of periods in an averaging interval needs to be an integer (whole), which can be achieved by starting averaging from one local maximum to another local maximum in drag evolution.
- Even when drag behavior becomes periodic, nearby periods for Reynolds number 150 do not repeat each other exactly. Only two/four drag periods taken together can be considered fully periodic. Therefore we use 16 number of periods for an averaging interval.

When a direct linear solver is used for solving of finite element linear system (as in the case of Freefem++ code), determining of local maximum/minimum in drag evolution is a trivial task, due to high precision of drag calculation. However, when an iterative solver is used, one cannot afford infinitely low relative accuracy of the iterative solver, hence the drag graph looks like a saw and automatic finding of local maximum/minimum becomes an issue. Additional difficulty, when using one-pass approach, is that we have to determine whether the current time step is a local minimum/maximum in drag evolution “on the fly”, since drag data after the current time step is not yet available. In order to overcome this issue we used least squares fit with quadratic

polynomial to approximate local evolution of drag at every time step, and use such approximation to determine whether there is local minimum/maximum at current iteration.

2.7 Numerical simulations

During the numerical simulations it appeared that for the first time steps, the required linear solver tolerance of 10^{-7} is hard to achieve, which is most likely due to difficulties in the initial spin up: we used zero velocity in Freefem++ code, and a solution of the Stokes equations as the initial condition in the deal.II code. Thus for Reynolds number 150 and a 4 million degrees of freedom (DOF) mesh, we could not achieve 10^{-7} for the very first time step. This issue gets worse with the increase of DOFs. For example (with the deal.II code) for a 500 thousand DOF mesh there were no issues with achieving 10^{-7} solver tolerance. But when we switched to 2 million DOFs, the iterative linear solver required 1000 outer iterations and even more during the first time steps. Therefore we had to reduce the outer solver tolerance to 10^{-3} at the first time steps and then gradually increase the solver tolerance with time until obtaining 10^{-7} . This allowed us to increase the mesh DOF to 4 million in the deal.II code. Since the averaging interval does not start until $t = 200$, this approach does not affect the precision of the obtained statistics. During the numerical simulations with the Freefem++ code and a direct solver, it was crashing for over 300 thousand DOFs for a single-threaded code (while working fine for up to 300 thousand DOF).

2.8 Computational Results

Algorithm for recirculation length search used in Freefem++ code:

Averaged velocity figures found in the literature and obtained in our study are symmetric across the line $y = 0$. We use this observation to conclude that recirculation length is located on the line $y = 0$. Therefore in Freefem++ we carry out a linear search along the line $y = 0$ starting from the right boundary of the flat plate.

Algorithm for recirculation length search used in deal.II code:

Since the mesh is distributed across many MPI workers, we need to carry out a linear search

separately on every MPI worker on the locally available part of the mesh, and then use collective MPI operation to find the minimum among all MPI workers. The obtained minimum point is reported as recirculation length.

On the figures below, the recirculation length is denoted by red *.

Strouhal number computation

In order to increase the resolution of FFT transformation for Strouhal number computation, we use spline interpolation of drag values (“spline” function in Matlab) to create $10N$ data points (where N is the number of data points), and then apply FFT transformation to interpolated data. After that if, in an area of frequency with maximum amplitude, there is a neighboring frequency that has close amplitude, we compute weighted average with the frequency with maximum amplitude and report it as Strouhal number.

2.8.1 Reynolds number 50

The (Q_2, Q_1) element results are in good compliance with Freefem++ results: thus average drag increases with finer mesh and seem to approach (Q_2, Q_1) element average drag computed with 4 million degrees of freedom from below.

Average drag for every fixed mesh has converged with respect to a time step in 4 digits. Therefore we conclude that $\Delta t = 0.005$ is small enough for precise computation of average drag (and similar with recirculation length and Strouhal number).

Note that in [45] for Reynolds number 50 average drag is reported as 2.47, but in [46] average drag for Reynolds number 35 is 1.87, and average drag for Reynolds number 75 is 2.26, hence it follows that the average drag value for Reynolds number 50 is expected to belong to interval $[1.87, 2.26]$. The average drag from the literature (computed on coarser mesh) significantly differs from all computed by the present project drag values. The Strouhal number from the literature coincides in the first two significant digits to our results.

When building statistics intervals below, we ignore Freefem++ results with 200 thousand DOF, due to the presence of Freefem++ results with 300 thousand DOF and the same other parameters. For Reynolds number 50, average drag $\in [2.213, 2.234]$, which is in good compli-

Method	Re	Δt	DOF	Software/Elt	C_d^{ave}	Recirc length	Strouhal	$c_d^{max} - c_d^{min}$ ($t > 200$)
BDF2	50	0.005	197781	Freefem/ P_2P_1	2.21062	2.04376	0.1565	0.0315
BDF3	50	0.005	197781	Freefem/ P_2P_1	2.21057	2.04390	0.1558	0.0314
CNLE	50	0.005	197781	Freefem/ P_2P_1	2.21060	2.04383	0.1589	0.0314
BDF2	50	0.005	290234	Freefem/ P_2P_1	2.21343	2.04251	0.1558	0.0315
BDF3	50	0.005	290234	Freefem/ P_2P_1	2.21338	2.04266	0.1526	0.0315
CNLE	50	0.005	290234	Freefem/ P_2P_1	2.21341	2.04258	0.1560	0.0315
BDF2	50	0.02	521632	deal.II/ Q_2Q_1	2.23375	2.03895	0.1555	0.0245
BDF2	50	0.01	521632	deal.II/ Q_2Q_1	2.23322	2.04056	0.1555	0.0245
BDF2	50	0.005	521632	deal.II/ Q_2Q_1	2.23313	2.04082	0.1559	0.0246
BDF2	50	0.02	2082368	deal.II/ Q_2Q_1	2.22794	2.03750	0.1558	0.0239
BDF2	50	0.01	2082368	deal.II/ Q_2Q_1	2.22741	2.03915	0.1558	0.0239
BDF2	50	0.005	2082368	deal.II/ Q_2Q_1	2.22730	2.03943	0.1558	0.0240
BDF2	50	0.005	4019895	deal.II/ Q_2Q_1	2.22485	2.03865	0.1559	0.0237
Saha [45], Adams- Bashforth forward scheme	50	$5 \cdot 10^{-4}$	426×162 stag- gered MAC grid		2.47		0.1526	

Table 2.1: Reynolds number 50 results.

ance with [46]. The lowest average drag value differs from the highest value by only 0.91%, which allows us to conclude that all average drag values are highly consistent for all discretization schemes/time steps/finite element types used herein. Recirculation length $\in [2.0375, 2.04266]$. The lowest recirculation length value differs from the highest value by only 0.25%. Strouhal number $\in [0.152588, 0.156009]$. The lowest Strouhal number differs by 2.19% comparing to the maximum Strouhal number.

As one can see from drag evolution figure 2.4, fluid behavior becomes periodic for some $t \in [150, 200]$. Therefore we start averaging from $t = 200$. Each period in drag evolution corresponds to 2 eddies shedding: one eddy from the upper part of the flat plate, and one from the bottom part. Then everything repeats.

The symmetry across line $y = 0$ on time-averaged velocity figure 2.5 confirms that fluid behavior after $t = 200$ is fully periodic. The recirculation length on the figure 2.5 is placed according to the data in table 2.1 and indeed corresponds to a steady point of averaged velocity field in figure 2.5.

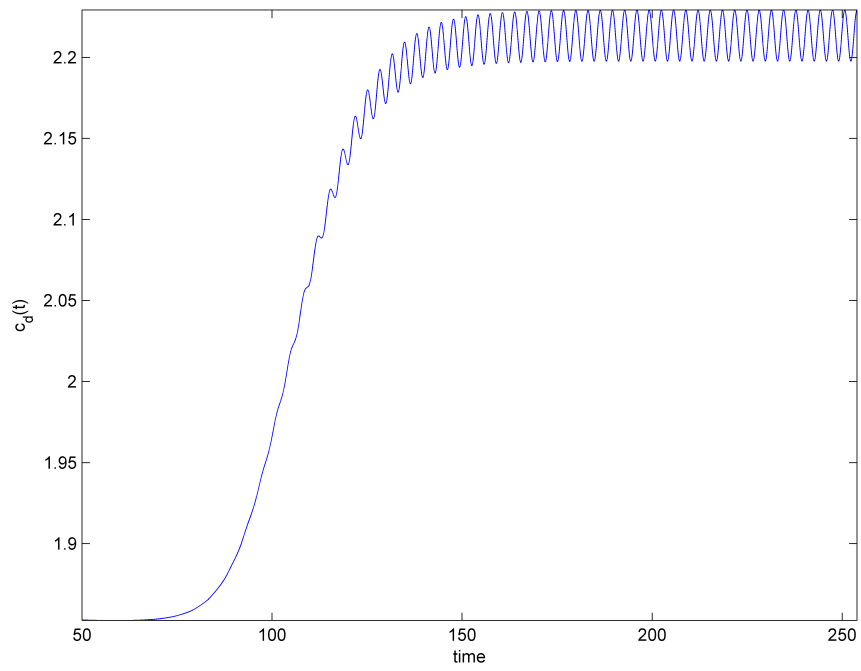


Figure 2.4: Drag for 290K DOF mesh, Reynolds 50.

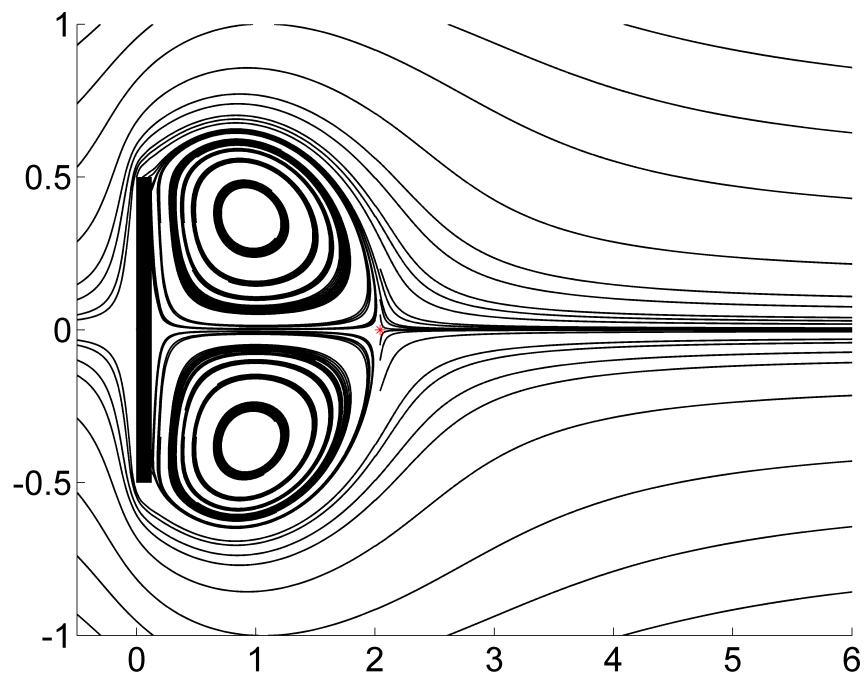


Figure 2.5: Averaged velocity figure for Reynolds number 50, red * denotes calculated recirculation point.

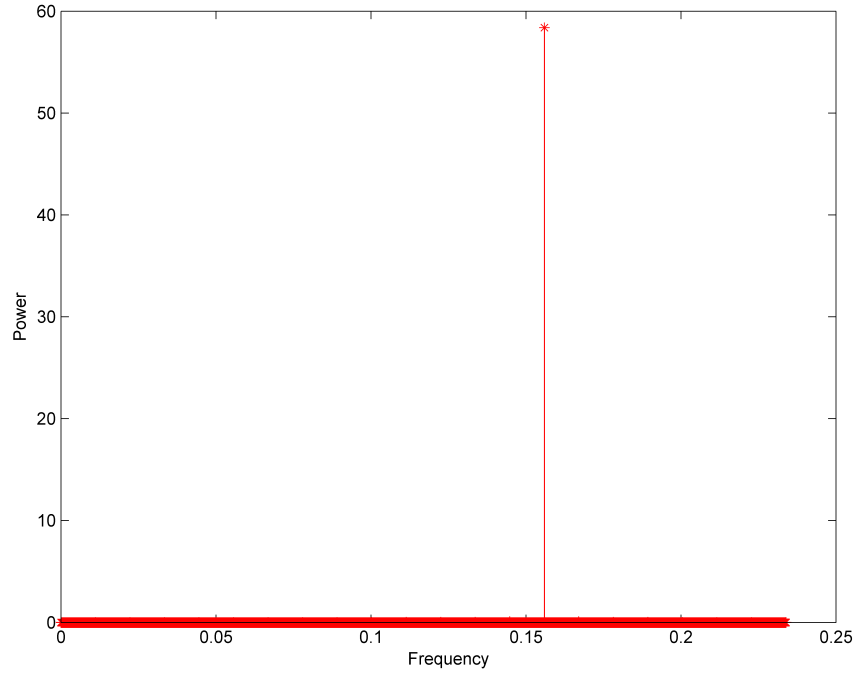


Figure 2.6: Strouhal number for 4M DOF mesh, Reynolds 50.

The Strouhal number shown in figure 2.6 has a clear dominant peak, which means that there is a primary frequency.

2.8.2 Reynolds number 100

Averaged drag increased comparing to Reynolds number 50. Strouhal number number increased comparing to Reynolds number 50. This means eddies shedding faster for Reynolds number 100, which is explained by the fact that higher Reynolds number corresponds to a faster moving fluid.

Method	Re	Δt	DOF	Software/Elt	C_d^{ave}	Recirc length	Strouhal	$c_d^{max} - c_d^{min}$ ($t > 200$)
BDF2	100	0.005	197781	Freefem/ P_2P_1	2.62181	1.14006	0.1907	0.3242
BDF3	100	0.005	197781	Freefem/ P_2P_1	2.62168	1.14014	0.1800	0.3242
CNLE	100	0.005	197781	Freefem/ P_2P_1	2.62173	1.14009	0.1876	0.3240
BDF2	100	0.005	290234	Freefem/ P_2P_1	2.62657	1.13928	0.1907	0.3250
BDF3	100	0.005	290234	Freefem/ P_2P_1	2.62648	1.13940	0.1907	0.3250
CNLE	100	0.005	290234	Freefem/ P_2P_1	2.62652	1.13935	0.1907	0.3248
BDF2	100	0.02	521632	deal.II/ Q_2Q_1	2.65943	1.13897	0.1894	0.2437
BDF2	100	0.01	521632	deal.II/ Q_2Q_1	2.65820	1.14024	0.1896	0.2435
BDF2	100	0.005	521632	deal.II/ Q_2Q_1	2.65795	1.14045	0.1895	0.2437
BDF2	100	0.02	2082368	deal.II/ Q_2Q_1	2.65072	1.13677	0.1900	0.2401
BDF2	100	0.01	2082368	deal.II/ Q_2Q_1	2.64951	1.13804	0.1901	0.2400
BDF2	100	0.005	2082368	deal.II/ Q_2Q_1	2.64924	1.13829	0.1901	0.2402
BDF2	100	0.005	4093417	deal.II/ Q_2Q_1	2.64541	1.13728	0.1903	0.2385
Saha in [45]	100	$5 \cdot 10^{-4}$			2.60		0.1826	
Saha in [46]	100				2.43	1.11	0.183	
Najjar & Vanka in [37]	100				2.43		0.166 (x=2,y=1)	

Table 2.2: Reynolds number 100 results

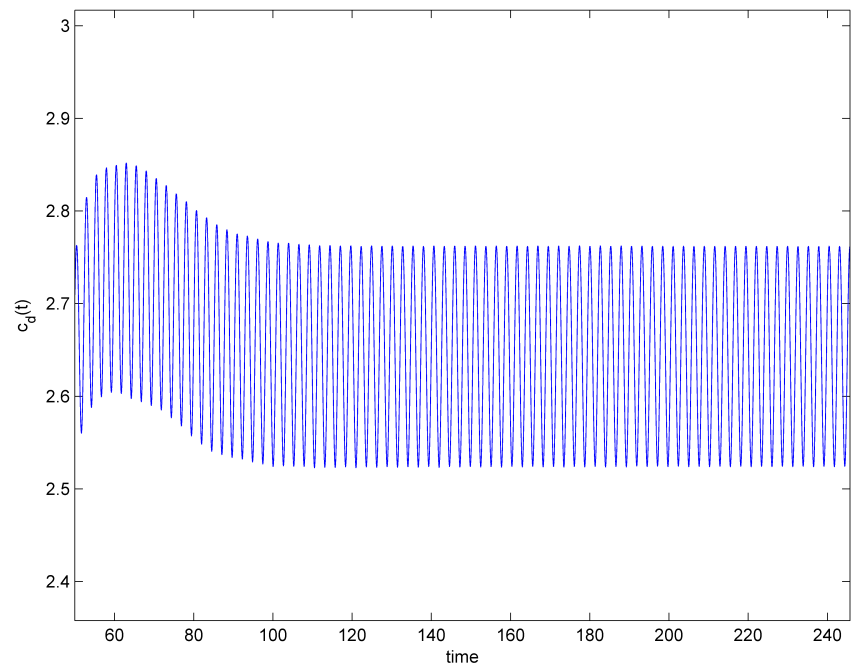


Figure 2.7: Drag for 4M DOF mesh, Reynolds 100.

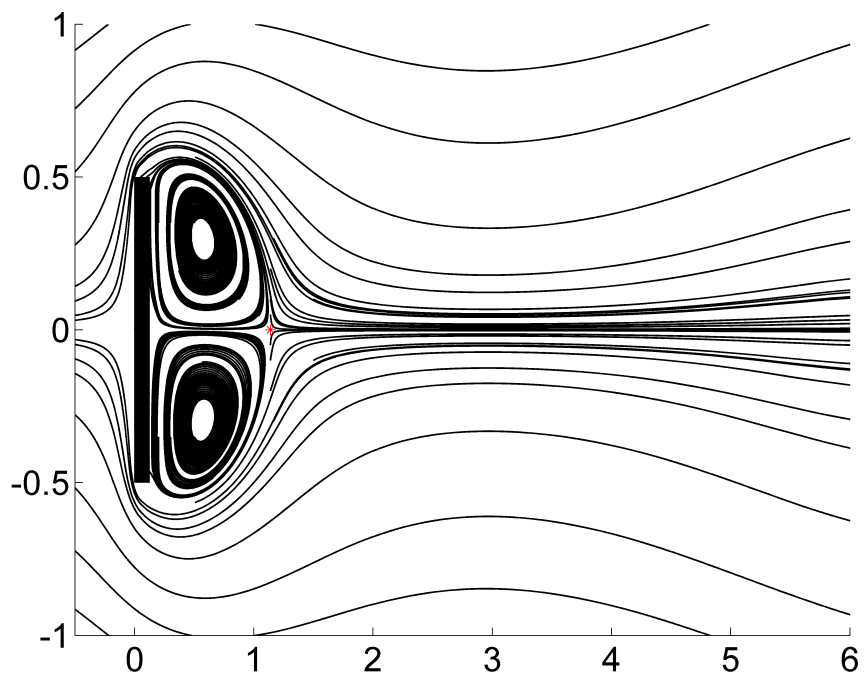


Figure 2.8: Averaged velocity for 290K DOF mesh, Reynolds 100.

Recirculation length is much closer to the flat plate comparing to Reynolds number 50.

Note that average drag values for Reynolds number 100 from the literature differs in second digit! Recirculation point coincides in 2 digits and Strouhal number coincides in 2 digits with values obtained by the current project.

As one can see from figure 2.7, drag evolution becomes periodic by $T = 180$.

The fact that calculated recirculation length is much closer to the plate than it is for Reynolds number 50 is supported by averaged velocity figure 2.8.

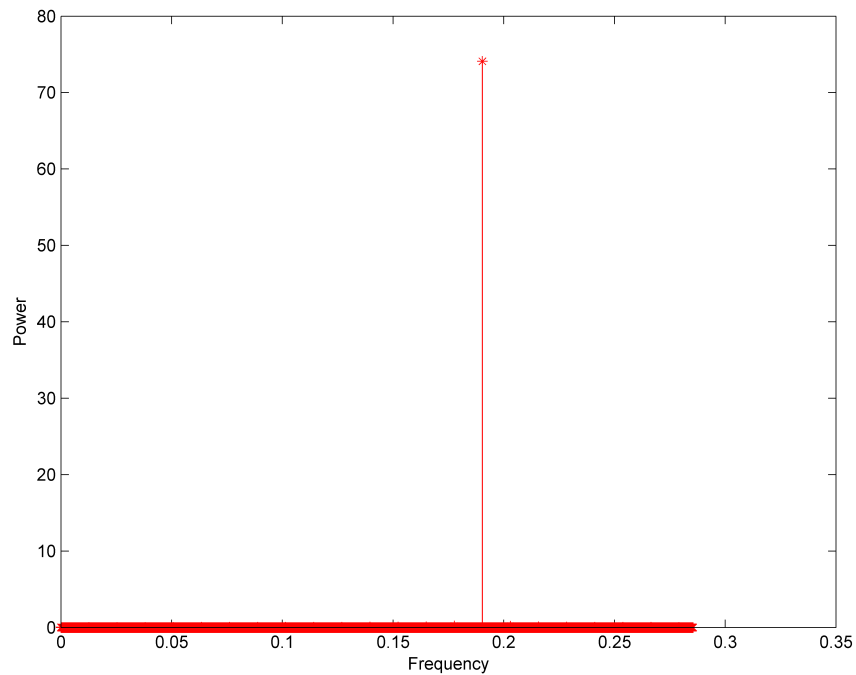


Figure 2.9: Strouhal number for 4M DOF mesh, Reynolds 100.

Method	Re	Δt	DOF	Software/Elt	C_d^{ave}	Recirc length	Strouhal	$c_d^{max} - c_d^{min}$ ($t > 200$)
BDF2	150	0.005	203928	Freefem/ P_2P_1	2.67926	1.14498	0.1755	0.5220
BDF3	150	0.005	203928	Freefem/ P_2P_1	2.67892	1.14523	0.1755	0.5222
CNLE	150	0.005	203928	Freefem/ P_2P_1	2.67922	1.14502	0.1755	0.5217
BDF2	150	0.005	299468	Freefem/ P_2P_1	2.68434	1.14455	0.1755	0.5230
BDF3	150	0.005	299468	Freefem/ P_2P_1	2.68459	1.14440	0.1755	0.5239
CNLE	150	0.005	299468	Freefem/ P_2P_1	2.68429	1.14460	0.1755	0.5227
BDF2	150	0.02	521632	deal.II/ Q_2Q_1	2.72322	1.14457	0.1751	0.3922
BDF2	150	0.01	521632	deal.II/ Q_2Q_1	2.72304	1.14552	0.1751	0.3926
BDF2	150	0.005	521632	deal.II/ Q_2Q_1	2.72242	1.14582	0.1750	0.3932
BDF2	150	0.02	2082368	deal.II/ Q_2Q_1	2.71223	1.14139	0.1759	0.3894
BDF2	150	0.01	2082368	deal.II/ Q_2Q_1	2.70974	1.14303	0.1757	0.3889
BDF2	150	0.005	2082368	deal.II/ Q_2Q_1	2.70991	1.14333	0.1756	0.3870
BDF2	150	0.005	4078986	deal.II/ Q_2Q_1	2.70421	1.14259	0.1761	0.3867
Saha in [45]	150	$5 \cdot 10^{-4}$			2.54		0.1665	
Saha in [46]	150				2.54	1.17, 4.24	0.167	

Table 2.3: Reynolds number 150 results

2.8.3 Reynolds number 150

As one can see from the figure 2.11 drag becomes periodic by $t = 200$ or earlier. Therefore starting averaging interval from the first maximum after $t = 200$ must lead to correct statistics.

The recirculation length on the figure 2.10 is placed according to the data in table 2.3 and indeed corresponds to a steady point of averaged velocity field in figure 2.10.

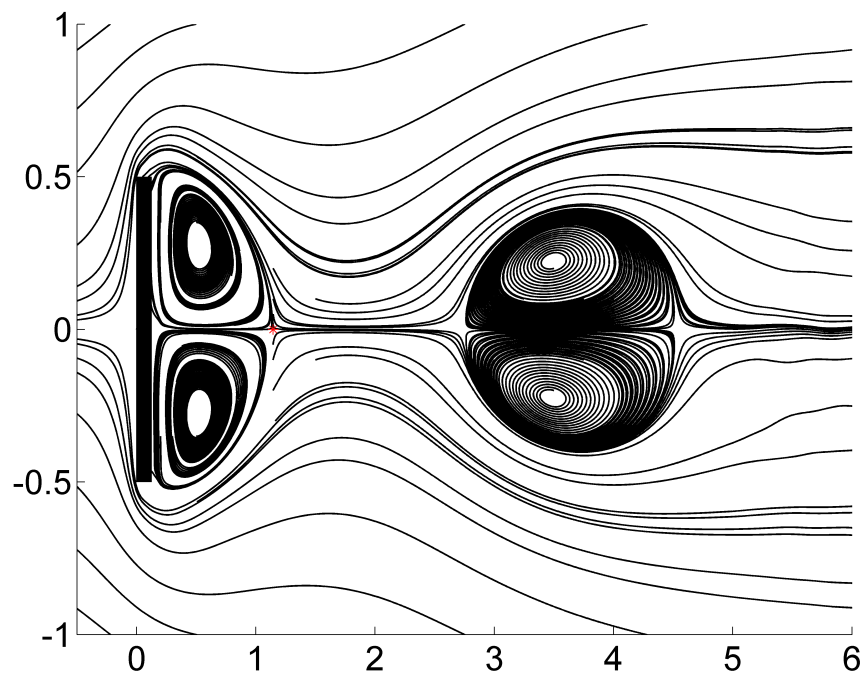


Figure 2.10: Average velocity for 290K DOF mesh, Reynolds 150.

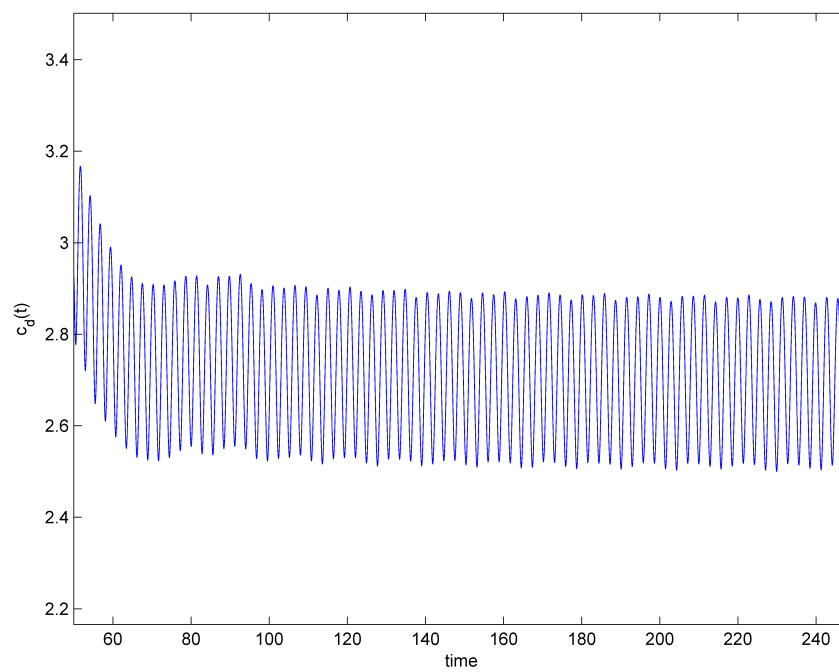


Figure 2.11: Drag for 4M DOF mesh, Reynolds 150.

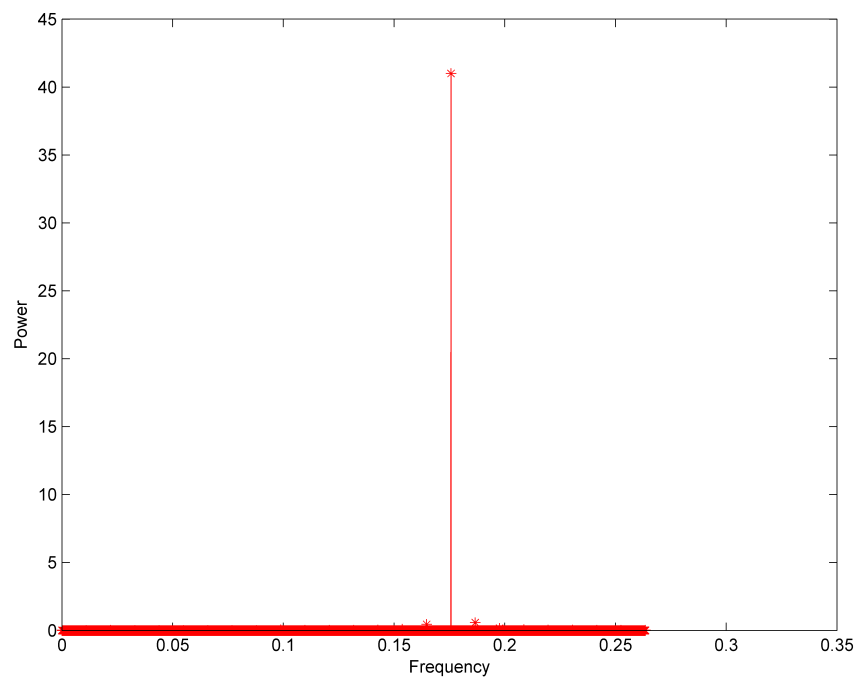


Figure 2.12: Strouhal number for 2M DOF mesh, Reynolds 150.

deal.II setup

In our C++ code we use the deal.II program library. As stated on deal.II web site [1], ‘deal.II - a name that originally meant to indicate that it is the successor to the Differential Equations Analysis Library - is a C++ program library targeted at the computational solution of partial differential equations using adaptive finite elements. It uses state-of-the-art programming techniques to offer you a modern interface to the complex data structures and algorithms required’.

Our C++ code uses BDF2 discretization scheme. The (Q_2, Q_1) finite element is used in numerical simulation. The initial condition is obtained by solving Stokes equations for the same Reynolds number and boundary conditions. Meshes used are 500K, 2 million and 4 million degrees of freedom. Mesh is finer around the flat plate and gets coarser further from the flat plate as the flow is most complicated close around the flat plate. We use the excellent block solver with grad-div preconditioner developed by Dr. Heister and Dr. Rapin, which is described in the paper [26]. The linear solver uses the iterative Krylov method (flexible GMRES) to solve the arising linear system with a preconditioner. The linear system resulting from the discretized NSE has the following block structure.

$$Mx = G,$$

with

$$M = \begin{pmatrix} A & B^T \\ B & 0 \end{pmatrix},$$
$$G = \begin{pmatrix} F \\ 0 \end{pmatrix}.$$

Instead of solving the above system directly, the right preconditioner is applied with an operator P^{-1} , and the solution is calculated as

$$x = P^{-1}y.$$

The auxiliary variable y is the solution of

$$MP^{-1}y = G.$$

P^{-1} is an implicitly defined operator given in a block-triangular way as

$$P^{-1} := \begin{pmatrix} \tilde{A} & B^T \\ 0 & \tilde{S} \end{pmatrix}^{-1} = \begin{pmatrix} \tilde{A}^{-1} & 0 \\ 0 & I \end{pmatrix} \begin{pmatrix} I & B^T \\ 0 & -I \end{pmatrix} \begin{pmatrix} I & 0 \\ 0 & \tilde{S}^{-1} \end{pmatrix},$$

where \tilde{S} is an approximation of the Schur complement

$$S = -BA^{-1}B^T,$$

and \tilde{A} is an approximation to the velocity block. We use one V-cycle of the algebraic multigrid to approximate \tilde{A}^{-1} . The preconditioner uses grad-div stabilization parameter term. As it is suggested in [11, 26, 56], the operator \tilde{S}^{-1} is approximated by the sum

$$\tilde{S}^{-1} = S_1^{-1} + S_2^{-1},$$

where

$$S_1 = \frac{1}{\nu + \gamma} M_p$$

and

$$S_2 = \frac{10^{-5}}{c} M_p + \frac{1}{c} L_p.$$

γ is grad-div stabilization parameter (we use $\gamma = 0.1$), ν is viscosity, M_p is the mass matrix in the pressure space, L_p is the stiffness matrix of the pressure Poisson problem with the Neumann boundary conditions, and

$$c = \frac{3}{2\Delta t}.$$

The actions for S_1^{-1} and S_2^{-1} are approximated by separate inner solves with GMRES preconditioned with the incomplete LU factorization respectively. The preconditioner obtained with the

incomplete LU factorization has the same sparsity pattern as the matrix itself known as ILU(0). The outer solve with flexible GMRES is stopped when the current residual is decreased 10^{-8} times relative to the starting residual. The stopping criterion for the preconditioned GMRES solves for approximating actions of S_1^{-1} and S_2^{-1} is when the ratio of the starting residual to the current residual is equal or lower than 10^{-2} . We use a flexible GMRES method for the outer solve, because we use iterative linear solvers to approximate the preconditioner. In particular the preconditioner cannot be considered as linear operator from one outer solve iteration to the next [26, 44]. We report the typical number of iterations that are needed for the inner and the outer GMRES solves in table 2.4. The number of iterations are obtained for 3D flow past a circular cylinder problem with $\gamma = 0.1$. For the number of inner iterations we report sum of the number of iterations for both S_1^{-1} and S_2^{-1} solves.

Δt	DOF	Average. Outer	Average. Inner ($S_1 + S_2$)
0.005	2 289 362	24.8	39.1
0.005	23 516 262	26.2	43.1
0.01	23 579 751	36.8	46.2
0.01	70 456 859	43.7	60.6

Table 2.4: Typical number of iterations that are needed for the inner and the outer GMRES solves.

The developed deal.II code is highly parallel, which allowed to increase degrees of freedom up to 4 million and refine time step to $\Delta t = 0.005$. Total simulation time T is about 250 (depending on the length of averaging interval), hence total number of time iterations is $250/0.005 = 50000$. The computational time for 4 million DOF mesh is over 2 weeks using 5 nodes with 24 cores each, which required a special reservation queue.

FreeFem++ setup

As stated on FreeFem++ library web site [2], ‘FreeFem++ is a partial differential equation solver. It has its own language. freefem scripts can solve multiphysics non linear systems in 2D and 3D. Problems involving PDE (2D, 3D) from several branches of physics such as fluid-structure interactions require interpolations of data on several meshes and their manipulation within one program. FreeFem++ includes a fast 2^d -tree-based interpolation algorithm and a language for the

manipulation of data on multiple meshes (as a follow up of bamg, now a part of FreeFem++). FreeFem++ is written in C++ and the FreeFem++ language is a C++ idiom.’

FreeFem++ computations are carried out using Crank-Nicolson, BDF2 and BDF3 discretization methods. Initial condition for velocity and pressure is zero. Time step is 0.005 seconds. We use UMFPACK linear solver that implements unsymmetric multiFrontal method [16]. The developed FreeFem++ code is single threaded. The (P_2, P_1) finite element is used in numerical simulation.

2.9 Evaluation of the computational results

The figures of averaged velocity for all Reynolds numbers 50, 100, 150 are very similar to corresponding figures found in the literature for the studied flat plate problem. See e.g. references [45],[46],[28]. Drag, recirculation length and Strouhal number for all Reynolds numbers 50, 100, and 150 have converged both with respect to time step refinement and with respect to mesh refinement.

We report statistics for Reynolds numbers 50, 100 and 150 obtained with the maximum space resolution in table 2.5. These statistics can be used for verification of new models and/or discretization schemes for the incompressible NSE.

Method	Re	Δt	DOF	C_d^{ave}	Recirc length	Strouhal	$c_d^{max} - c_d^{min}$ ($t > 200$)
BDF2	50	0.005	4019895	2.22485	2.03865	0.1559	0.0237
BDF2	100	0.005	4093417	2.64541	1.13728	0.1903	0.2385
BDF2	150	0.005	4078986	2.70421	1.14259	0.1761	0.3867

Table 2.5: Statistics for Reynolds numbers 50, 100, 150 obtained with 4 million DOF space resolution, with (Q_2, Q_1) finite element.

2.10 Summary

A two-dimensional flow through a channel around a vertical flat plate obstacle with a time-independent inflow was computed with three time stepping schemes (BDF2, BDF3 and Crank-Nicolson). The evolutions of the drag at the flat plate, recirculation length and Strouhal number have been studied. The code is implemented twice in two different environments for verification of

results (with Freefem++ and deal.II). New more precise reference values for the averaged drag coefficient, recirculation length, and the Strouhal number, have been derived from the computational results.

The present numerical project differs from results found in the literature in the following. Firstly, the maximum space resolution is 4 million degrees of freedom, which is much higher than for results found in the literature. For example we estimate DOF number in [46] to be about only 100 thousand DOF. For the same parameters, numerical simulations are carried out with several different meshes and different time steps. This allowed to show convergence of statistics both with respect to spatial resolution and with respect to time step refinement. All presented statistics are computed purely using software code only, i.e. no human measurement error involved. The same numerical simulation was carried out independently using deal.II and Freefem++ software and both gave very similar results. In addition both deal.II/ Q_2Q_1 and Freefem/ P_2P_1 element types were used. Finally, the averaging interval does not start until $T = 200$, that is until fluid behavior becomes fully periodic to guarantee reliable values of statistics.

Chapter 3

Energy, momentum and angular momentum conserving formulation

This chapter is from the work done by the author and collaborators in [15]. We consider formulations of the incompressible NSE, which are given in a domain $\Omega \subset \mathbb{R}^d$, $d=2$ or 3 , and for $t > 0$ by

$$u_t + (u \cdot \nabla)u + \nabla p - \nu \Delta u = f, \quad (3.1)$$

$$\operatorname{div} u = 0, \quad (3.2)$$

$$u(0) = u_0, \quad (3.3)$$

where u and p represent velocity and pressure, f is an external forcing, u_0 is the initial velocity, and ν is the kinematic viscosity. To solve this system, it must also be equipped with the boundary conditions. Finding analytical solutions of the NSE is known to be extremely difficult, and thus practitioners instead typically approximate solutions using numerical methods.

In this chapter we study conservation laws of solutions arising from discretizations of the NSE with finite element methods. In typical discretizations, e.g., with Taylor-Hood finite elements, the conservation of mass is only weakly enforced, leading to discrete solutions u_h which have

$$\operatorname{div} u_h \neq 0.$$

While convergence of the H^1 error can often be proven, leading to the bound $\|\operatorname{div} u_h\| \leq Ch^2$, the divergence error can still be significant on practical meshes (here h is a characteristic step of an underlying mesh; in practice, there is a minimum h that can produce solutions in reasonable time).

With the loss of mass conservation, it turns out that many other important conservation laws are also lost, including energy, momentum, angular momentum, and others, if steps are not taken in the development of the numerical discretization to make sure these quantities are conserved. The fact that energy conservation is lost in Galerkin discretizations of the NSE is well-known, and a fix for this problem by using the skew-symmetric or rotation forms of the nonlinearity has been known for many years [55]. A finite element formulation for energy and helicity conservation was proposed in [43], and in [40] it was discussed how an alternate (but equally valid) definition of helicity could be conserved by skew-symmetric formulations. Similar phenomena happen with other types of discretization methods, and some clever discretizations have been developed which ‘bring back’ conservation laws lost in standard discretizations, beginning decades ago by Arakawa, Fix, and others, for the NSE and related equations [3–5, 17, 20, 35, 41, 48, 52]. A common theme for all ‘enhanced-physics’ based schemes is that *the more physics is built into the discretization, the more accurate and stable the discrete solutions are, especially over longer time intervals*.

In the present chapter, we aim to develop numerical schemes/formulations that preserve even more conservation laws for the full NSE, beyond just energy. By noticing that the key to discrete conservation properties is the formulation of the nonlinear term, we are able to find a formulation of the NSE seemingly unconsidered in the literature, which conserves all of energy, momentum, and angular momentum; we call it the *Energy, Momentum, and Angular Momentum (EMA) conserving* formulation. We propose this formulation in section 3.2, and formally show these conservation properties hold. We show that the usual convective, skew-symmetric and rotational formulations all fail to conserve momentum and angular momentum. Of course, if a Galerkin solution happens to be pointwise divergence-free, then all of the formulations are equivalent and each of them would conserve all of these quantities in an appropriate sense. However, the use of such special element choices that provide pointwise divergence-free solutions (e.g. [6, 18, 24, 25, 57]) is not widespread, as they require constraints on the mesh and approximating polynomial degrees, and are not typically available in open source finite element software for large scale computing [7].

This chapter is arranged as follows. Section 3.1 presents notation and mathematical preliminaries that will allow for smoother analysis in later sections. Section 3.2 presents the *EMA*-

conserving formulation, and studies its conservation properties along with those of the convective, skew-symmetric, conservative, and rotational formulations. Section 3.3 performs several numerical experiments, which test the conservation properties and accuracy of the various schemes.

3.1 Notation and preliminaries

Consider the domain $\Omega \subset \mathbb{R}^d$, $d = 2$ or 3 , and denote (\cdot, \cdot) and $\|\cdot\|$ to be the $L^2(\Omega)$ inner product and norm on Ω . Denote

$$|u|^2 := |u(x)|^2 = u(x) \cdot u(x).$$

Consider $u, v, w \in H^1(\Omega)$, and note that we do not enforce that any of these quantities are solenoidal except for the last two equations of this section. Let $w = \text{curl } u$. Define the trilinear form $b : H^1(\Omega) \times H^1(\Omega) \times H^1(\Omega) \rightarrow \mathbb{R}$ by

$$b(u, v, w) = (u \cdot \nabla v, w). \quad (3.4)$$

We recall the following properties of b . The first two follow immediately from integration by parts, provided $u \in H_0^1(\Omega)$:

$$b(u, v, w) = -b(u, w, v) - ((\text{div } u)v, w), \quad (3.5)$$

$$b(u, w, w) = -\frac{1}{2} ((\text{div } u)w, w), \quad (3.6)$$

$$b(u, v, w) = ((\nabla v)u, w) = ((\nabla v)^T w, u). \quad (3.7)$$

We denote the symmetric part of ∇u by

$$\nabla_s u := D(u) = \frac{\nabla u + (\nabla u)^T}{2},$$

and the skew-symmetric part by

$$\nabla_n u := \frac{\nabla u - (\nabla u)^T}{2}.$$

For any $u, v \in H^1(\Omega)$ one readily checks that

$$(\nabla_n u)v = \frac{1}{2}(\text{curl } u) \times v. \quad (3.8)$$

Note that we define $\text{curl } u$ in 2D in the usual way, as the 3D curl of u extended by 0 in the third component.

Straight-forward calculations provide the following vector identities for functions $u, v \in H^1(\Omega)$:

$$(u \cdot \nabla)u = (\text{curl } u) \times u + \nabla \frac{1}{2}|u|^2 =: (\text{curl } u) \times u + \nabla q, \quad (3.9)$$

$$(\nabla u)u = (\nabla_s u)u + (\nabla_n u)u = D(u)u + \frac{1}{2}(\text{curl } u) \times u, \quad (3.10)$$

where $q := \frac{|u|^2}{2}$. Also note that identity (3.10) implies that

$$(D(u)u, u) = ((\nabla u)u, u) = b(u, u, u). \quad (3.11)$$

From (3.8)–(3.10) we obtain the following representation of the inertia term from the momentum equations:

$$(u \cdot \nabla)u = 2D(u)u - \nabla q. \quad (3.12)$$

The identity (3.12) is key to the new formulation we propose in the next section, which leads to improved discrete conservation properties.

3.2 Conservation properties and the EMA formulation for Navier-Stokes

We now consider subspaces $X \subset [H_0^1(\Omega)]^d$, $Q \subset L^2(\Omega)$ of *finite dimensions*. To be more specific, we further assume that X and Q are finite element velocity and pressure spaces corresponding to an admissible triangulation of Ω . For simplicity we assume X and Q satisfy inf-sup compatibility conditions [21]; non inf-sup stable pairs require stabilization terms that will affect

conservation properties, and should be studied separately and on a case-by-case basis. We note our analysis can be easily extended to other Galerkin methods.

In most common discretizations of the NSE and related systems, the divergence-free constraint $\operatorname{div} u = 0$ is only weakly enforced. What holds instead of the pointwise constraint is that a numerical solution u from X satisfies

$$(\operatorname{div} u, q) = 0 \quad \forall q \in Q,$$

where Q is a *finite dimensional* pressure space, for example piecewise linears which are globally continuous. Even though convergence theory of mixed finite element methods exists that guarantees $\|\operatorname{div} u\|$ converges to 0 with optimal rate, in practical computations the divergence error can be large due to the associated constants being larger than the minimum practical mesh width [12]. Enlarging the pressure space Q to ensure $\operatorname{div} X \subset Q$ is usually not possible, since it would violate (apart of a few exceptional cases) the inf-sup compatibility condition and make the method numerically unstable.

We now consider conservation properties of several common NSE formulations, along with a new one based on the identity (3.12). To this end, we write the NSE momentum equation in the generic form:

$$u_t + N(u) + \nabla p - \nu \Delta u = f, \tag{3.13}$$

with the nonlinear terms defined for each formulation by

$$\begin{aligned} \textit{convective} & : N_{conv}(u) = u \cdot \nabla u, \\ \textit{skew-symmetric} & : N_{skew}(u) = u \cdot \nabla u + \frac{1}{2}(\operatorname{div} u)u, \\ \textit{rotational} & : N_{rot}(u) = (\operatorname{curl} u) \times u, \\ \textit{conservative} & : N_{cons}(u) = \nabla \cdot (u \otimes u) = u \cdot \nabla u + (\operatorname{div} u)u. \end{aligned}$$

The convective, skew-symmetric, and rotational forms above are commonly used in CFD and

numerical analysis of fluid equations, see, e.g., [22, 55], with the convective form being, probably, the most frequent choice in computation practice.

We propose now a new formulation, which we will show conserves energy, momentum and angular momentum, which we call the *energy momentum and angular momentum (EMA) conserving form*. It is based on the following choice:

$$EMA \text{ conserving} \quad : \quad N_{emac}(u) = 2D(u)u + (\operatorname{div} u)u.$$

We remark that if we did assume the divergence constraint $\operatorname{div} u = 0$ holds pointwise, then all above formulations are equivalent; for the EMA conserving scheme, this follows from (3.12).

The Galerkin method corresponding to various forms of inertia term reads: Find $\{u, p\} \in X \times Q$ satisfying

$$\left(\frac{\partial u}{\partial t} + N(u), v \right) - (p, \operatorname{div} v) + (q, \operatorname{div} u) + \nu(\nabla u, \nabla v) = (f, v) \quad (3.14)$$

for all $v \in X, q \in Q$.

For both the *rotational* and *EMA-conserving* formulations, the pressure p is modified and includes a velocity contribution. To our knowledge, the *EMA-conserving* formulation has yet to be considered in the literature, and our motivation for using it comes from Proposition 3.2.1 below, which says that of these five formulations, only the *EMA-conserving* formulation exactly conserves energy, momentum and angular momentum when the divergence constraint is not strongly enforced.

3.2.1 Energy, momentum and angular momentum

We now prove a result regarding conservation laws for (3.14). Our interest first is the conservation of energy, momentum and angular momentum:

$$\begin{aligned} \text{Kinetic energy} \quad E &= \frac{1}{2}(u, u) := \frac{1}{2} \int_{\Omega} |u|^2 dx; \\ \text{Linear momentum} \quad M &:= \int_{\Omega} u \, dx; \\ \text{Angular momentum} \quad M_x &:= \int_{\Omega} u \times x \, dx. \end{aligned}$$

Most useful boundary conditions alter the balance of these quantities, as they should in the presence of walls and interfaces. Moreover, the numerical treatment of boundaries, e.g. by enforcing conditions strongly or in a weak form, also affect this balance. In this study, we isolate the effect of the treatment of the nonlinearity on the quantities of interest from the contribution of the boundary conditions. For this reason, we assume in section 3.2 that *the finite element solution u and p is supported in some subset $\widehat{\Omega} \subsetneq \Omega$ of the computational domain Ω* , i.e., there is a strip $S = \Omega \setminus \widehat{\Omega}$ along $\partial\Omega$ where u is zero. The same is assumed for the source term f . We note this implies there is a strip of elements along the boundary where u , p , and f vanish. The prototypical scenario is the evolution of an isolated vortex in a self-induced flow.

Proposition 3.2.1. *Assuming $(\operatorname{div} u, q) = 0$ for all $q \in Q$, but $\operatorname{div} u \neq 0$, the skew-symmetric, rotational, and EMA-conserving formulations conserve kinetic energy (for $\nu = 0$, $f = 0$), and only the EMA-conserving and conservative formulations conserve momentum (for f with zero linear momentum) and angular momentum (for f with zero angular momentum). Hence, the EMA-conserving is the only one of the the formulations that conserves all three quantities.*

We divide the proof of this proposition into several subsections.

3.2.1.1 Kinetic energy

For energy conservation, testing (3.14) with $v = u$, $q = p$ gives

$$\frac{1}{2} \frac{d}{dt} \|u\|^2 + (NL(u), u) + \nu \|\nabla u\|^2 = (f, u).$$

Thus, kinetic energy will be preserved for $\nu = 0$, $f = 0$ if

$$(NL(u), u) = 0. \tag{3.15}$$

For the *skew-symmetric* formulation, we use (3.6) to get

$$(NL_{skew}(u), u) = b(u, u, u) + \frac{1}{2}((\operatorname{div} u)u, u) = 0,$$

and for the *rot* formulation we use that the cross of two vectors is perpendicular to each of them,

$$(NL_{rot}(u), u) = ((\operatorname{curl} u) \times u, u) = 0.$$

For the *EMA-conserving* formulation, we use (3.11) and then (3.6) to obtain

$$(NL_{emac}(u), u) = 2(D(u)u, u) + ((\operatorname{div} u)u, u) = 2b(u, u, u) + ((\operatorname{div} u)u, u) = 0.$$

For the *convective* formulation, the nonlinear term does not vanish in general:

$$(NL_{conv}(u), u) = b(u, u, u) = -\frac{1}{2}((\operatorname{div} u)u, u),$$

and thus kinetic energy will not be typically conserved by the *convective* formulation whenever $\operatorname{div} u \neq 0$. Lastly, for the *conservative* formulation, we use the same identity as in the *convective* case, and find that

$$(NL_{cons}(u), u) = b(u, u, u) + ((\operatorname{div} u)u, u) = \frac{1}{2}((\operatorname{div} u)u, u),$$

and thus this formulation will not conserve kinetic energy in general.

3.2.1.2 Linear Momentum

Next, we consider momentum conservation in the formulations. Let $e_1 = (1, 0, 0)^T$, $e_2 = (0, 1, 0)^T$ and $e_3 = (0, 0, 1)^T$. We cannot test (3.14) with $v = e_i$ since this function is not in X . Thanks to the assumption that $u \neq 0$ only in some strictly interior subdomain $\widehat{\Omega}$, we can define the restriction $\chi(g) \in X$ of an arbitrary function g by setting $\chi(g) = g$ in $\widehat{\Omega}$ and $\chi(g)$ arbitrary defined on $S = \Omega \setminus \widehat{\Omega}$ to satisfy zero boundary conditions. We test (3.14) with $v = \chi(e_i) \in X$ and $q = 0$, which gives

$$\frac{d}{dt}(u, e_i) + (N(u), e_i) = (f, e_i),$$

because the solution is zero on S . Thus, momentum conservation is obtained if $(f, e_i) = 0$ and $(N(u), e_i) = 0$. Thus we consider the latter for the different formulations. In the *convective* formulation, we use (3.5) and that e_i is constant to find that

$$\begin{aligned} (N_{conv}(u), e_i) &= b(u, u, e_i) = -b(u, e_i, u) - ((\operatorname{div} u)u, e_i) \\ &= -((\operatorname{div} u)u, e_i) \neq 0 \end{aligned}$$

in general. Linear momentum is NOT conserved.

For the *skew-symmetric* form we get

$$(N_{skew}(u), e_i) = b(u, u, e_i) + \frac{1}{2}((\operatorname{div} u)u, e_i) = -\frac{1}{2}((\operatorname{div} u)u, e_i) \neq 0$$

in general. Linear momentum is NOT conserved. For *rotational* form, we use the vector identity

$$u \cdot \nabla u = (\operatorname{curl} u) \times u + \frac{1}{2} \nabla |u|^2$$

to obtain

$$\begin{aligned}(N_{rot}(u), e_i) &= ((\text{curl } u) \times u, e_i) = b(u, u, e_i) - \frac{1}{2}(\nabla |u|^2, e_i) \\ &= (u \cdot \nabla u, e_i) = -((\text{div } u)u, e_i) \neq 0\end{aligned}$$

in general. Linear momentum is NOT conserved. For the *EMA-conserving* formulation, however, the nonlinear term does vanish. By expanding the rate of deformation tensor and using

$$(u \cdot \nabla u, e_i) = -((\nabla \cdot u)u, e_i),$$

and then (3.7), we find that

$$\begin{aligned}(N_{emac}(u), e_i) &= 2(D(u)u, e_i) + ((\text{div } u)u, e_i) \\ &= b(u, u, e_i) + b(e_i, u, u) + ((\text{div } u)u, e_i) \\ &= b(e_i, u, u) \\ &= 0,\end{aligned}$$

since e_i is divergence-free.

The *conservative* form also conserves momentum, as using the same identity as in the *convective* case, we obtain

$$(N_{cons}(u), e_i) = b(u, u, e_i) + ((\text{div } u)u, e_i) = -((\text{div } u)u, e_i) + ((\text{div } u)u, e_i) = 0.$$

3.2.1.3 Angular momentum

We consider next angular momentum conservation in the formulations; that is, whether or not they conserve $(M_x)_i := (u, \phi_i)$, $\phi_i := x \times e_i$, $i = 1, 2, 3$.

Let $x = \begin{pmatrix} x \\ y \\ z \end{pmatrix}$. Direct computation shows:

$$\phi_1 = \begin{pmatrix} 0 \\ z \\ -y \end{pmatrix}, \phi_2 = \begin{pmatrix} -z \\ 0 \\ x \end{pmatrix}, \phi_3 = \begin{pmatrix} y \\ -x \\ 0 \end{pmatrix}. \quad (3.16)$$

This implies

$$\nabla \phi_1 = \begin{pmatrix} 0 & 0 & 0 \\ 0 & 0 & -1 \\ 0 & 1 & 0 \end{pmatrix}, \quad (3.17)$$

$$\nabla \phi_2 = \begin{pmatrix} 0 & 0 & 1 \\ 0 & 0 & 0 \\ -1 & 0 & 0 \end{pmatrix}, \quad (3.18)$$

$$\nabla \phi_3 = \begin{pmatrix} 0 & -1 & 0 \\ 1 & 0 & 0 \\ 0 & 0 & 0 \end{pmatrix}. \quad (3.19)$$

Note that $\operatorname{div} \phi_i = 0$ and $\Delta \phi_i = 0$. Setting $v = \chi(\phi_i)$, $q = 0$ in (3.14) gives

$$\left(\frac{\partial u}{\partial t}, \phi_i \right) + (N(u), \phi_i) + \nu(\nabla u, \nabla \phi_i) = (f, \phi_i).$$

Whether angular momentum is conserved comes down, once again, to whether it is preserved by the nonlinear term, i.e. whether or not $(N(u), \phi_i) = 0$. For the *EMA-conserving* formulation, since

$\operatorname{div} \phi_i = 0$ we have that

$$\begin{aligned}
(N_{emac}(u), \phi_i) &= 2(D(u)u, \phi_i) + ((\operatorname{div} u)u, \phi_i) \\
&= b(u, u, \phi_i) + b(\phi_i, u, u) + ((\operatorname{div} u)u, \phi_i) \\
&= b(u, u, \phi_i) + ((\operatorname{div} u)u, \phi_i) \\
&= -b(u, \phi_i, u),
\end{aligned}$$

with the last step coming from (3.5). From here, expanding out the terms immediately reveals that $b(u, \phi_i, u) = 0$, and thus the *EMA-conserving* formulation does conserve angular momentum.

Similarly for the *conservative* formulation,

$$\begin{aligned}
(N_{cons}(u), \phi_i) &= b(u, u, \phi_i) + ((\operatorname{div} u)u, \phi_i) \\
&= -b(u, \phi_i, u) \\
&= 0.
\end{aligned}$$

For the *convective* formulation, similar identities reveal

$$(N_{conv}(u), \phi_i) = b(u, u, \phi_i) = -((\operatorname{div} u)u, \phi_i) \neq 0$$

in general, and for the *skew-symmetric* formulation we use these same identities to obtain

$$(N_{skew}(u), \phi_i) = b(u, u, \phi_i) + \frac{1}{2}((\operatorname{div} u)u, \phi_i) = -\frac{1}{2}((\operatorname{div} u)u, \phi_i),$$

which will not be zero in general either. For the *rotational* formulation, we again use the vector identity

$$u \cdot \nabla u = (\operatorname{curl} u) \times u + \frac{1}{2} \nabla |u|^2,$$

which provides since $\operatorname{div} \phi_i = 0$,

$$(N_{rot}(u), \phi_i) = ((\operatorname{curl} u) \times u, \phi_i) = (u \cdot \nabla u, \phi_i) = -((\operatorname{div} u)u, \phi_i),$$

which is the same as for the *convective* formulation.

3.2.2 Discussion

We have now established that the *EMA-conserving* formulation does indeed conserve kinetic energy, linear momentum and angular momentum. One may question if the *EMA-conserving* formulation is the only one or the ‘simplest’ one which conserves all quantities listed above. We do not have an ultimate answer to these questions. Nevertheless, attempting to address it let us comment on the way we deduce this formulation: we can write the momentum equation with linear combinations of different forms of the inertia terms from (3.4), (3.9), (3.10) and additional divergence terms. The *EMA-conserving* formulation is then found to be the unique combination that conserves discrete kinetic energy, momentum, and angular momentum.

3.3 Numerical Experiments

We now provide results of several numerical experiments that test and compare the different NSE formulations. The specific formulations we test are (for the case of homogeneous Dirichlet boundary conditions):

Find $(u_h, p_h) \in (X_h, Q_h)$ such that for every $(v_h, q_h) \in (X_h, Q_h)$,

Convective formulation (CONV)

$$\begin{aligned} ((u_h)_t, v_h) + (u_h \cdot \nabla u_h, v_h) - (p_h, \operatorname{div} v_h) + \nu(\nabla u_h, \nabla v_h) &= (f, v_h), \\ (\operatorname{div} u_h, q_h) &= 0. \end{aligned}$$

Skew-symmetric formulation (SKEW)

$$\begin{aligned} ((u_h)_t, v_h) + (u_h \cdot \nabla u_h, v_h) + \frac{1}{2}((\operatorname{div} u_h)u_h, v_h) - (p_h, \operatorname{div} v_h) + \nu(\nabla u_h, \nabla v_h) &= (f, v_h), \\ (\operatorname{div} u_h, q_h) &= 0. \end{aligned}$$

Conservative formulation (CONS)

$$\begin{aligned} ((u_h)_t, v_h) + (u_h \cdot \nabla u_h, v_h) + ((\operatorname{div} u_h)u_h, v_h) - (p_h, \operatorname{div} v_h) + \nu(\nabla u_h, \nabla v_h) &= (f, v_h), \\ (\operatorname{div} u_h, q_h) &= 0. \end{aligned}$$

Rotational formulation (ROT)

$$\begin{aligned} ((u_h)_t, v_h) + ((\operatorname{curl} u_h) \times u_h, v) - (p_h, \operatorname{div} v_h) + \nu(\nabla u_h, \nabla v_h) &= (f, v_h), \\ (\operatorname{div} u_h, q_h) &= 0. \end{aligned}$$

Energy, momentum, and angular momentum conserving formulation (EMAC)

$$\begin{aligned} ((u_h)_t, v_h) + 2(D(u_h)u_h, v_h) + ((\operatorname{div} u_h)u_h, v_h) - (p_h, \operatorname{div} v_h) + \nu(\nabla u_h, \nabla v_h) &= (f, v_h), \\ (\operatorname{div} u_h, q_h) &= 0. \end{aligned}$$

For the temporal discretizations, our tests employ several temporal discretizations, including Crank-Nicolson method for the Gresho problem described below (since here we test for integral invariants), BDF2, and BDF3. The choice of Taylor-Hood velocity-pressure elements is used throughout, which is (P_2, P_1) on triangular meshes, and (Q_2, Q_1) on quadrilateral meshes. No stabilization was used in any of the 2D simulations, however for the (Q_2, Q_1) computations, grad-div stabilization [39] with a small parameter ($\gamma = 0.1$) was used since it is an integral part of the preconditioner used for the linear solves. We recognize that different element choices and different stabilizations can improve these schemes to varying degrees; future studies certainly could include various stabilization and element choices. In all of our tests, we solve the full nonlinear problem, for each formulation, at each time step in the simulations using a Newton method, and we converge the nonlinear iteration up to 10^{-8} . For the channel flow problems with an outflow, we weakly enforce the zero-traction boundary condition $(-\nu \nabla u + pI) \cdot n|_{\Gamma_{out}} = 0$. For the convective and conservative formulations, this becomes a ‘do-nothing’ condition. For the rest of the formulations, it requires a nonlinear boundary integral at the outflow. To illustrate the conservation properties of the various formulations, we

choose several test problems: For the first one, the quantities of interest are exactly conserved, while other test cases represent more realistic scenarios of viscous fluid flows passing streamlined or bluff bodies. In the latter case, viscous and boundary effects perturb all conservation laws. We include these test cases in the attempt to give the first assessment of other properties of the EMAC form such as numerical stability and accuracy.

3.3.1 Gresho Problem

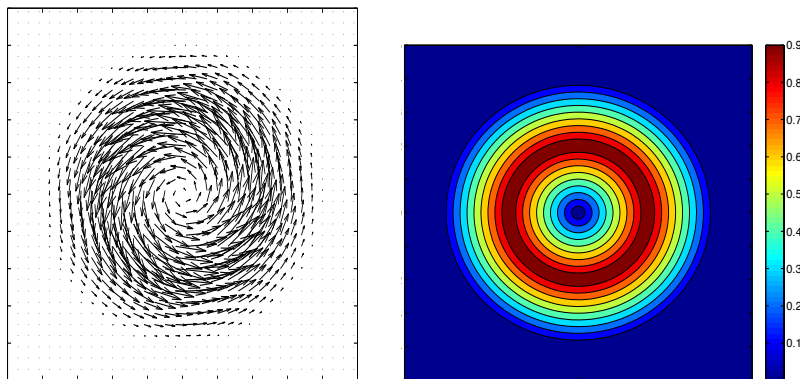


Figure 3.1: Shown above is the true velocity solution for the Gresho problem as a vector figure (left) and speed contour figure (right).

We consider first the Gresho problem, which is often referred to as the ‘standing vortex problem’ [22, 34, 53]. The problem is defined by starting with an initial condition u_0 that is an exact solution of the steady Euler equations. On $\Omega = (-.5, .5)^2$, with $r = \sqrt{x^2 + y^2}$, the velocity

and pressure solutions are defined by

$$\begin{aligned} r \leq 0.2 : & \begin{cases} u = \begin{pmatrix} -5y \\ 5x \end{pmatrix} \\ p = 12.5r^2 + C_1 \end{cases} , \\ r > 0.4 : & \begin{cases} u = \begin{pmatrix} 0 \\ 0 \end{pmatrix} \\ p = 0 \end{cases} , \\ 0.2 \leq r \leq 0.4 : & \begin{cases} u = \begin{pmatrix} \frac{2y}{r} + 5y \\ \frac{2x}{r} - 5x \end{pmatrix} \\ p = 12.5r^2 - 20r + 4\log(r) + C_2 \end{cases} , \end{aligned}$$

where

$$C_2 = (-12.5)(0.4)^2 + 20(0.4)^2 - 4\log(0.4), \quad C_1 = C_2 - 20(0.2) + 4\log(0.2).$$

The vorticity ($w = u_{2x} - u_{1y}$) can be calculated to be $w = 10$ when $r \leq 0.2$, $w = 2/r - 10$ on $0.2 \leq r \leq 0.4$, and $w = 0$ when $r > 0.4$. This is an interesting problem because it is an exact solution of the steady Euler equations, i.e.

$$u \cdot \nabla u + \nabla p = 0.$$

Since we choose the initial condition to be this steady Euler solution, an accurate scheme should preserve the solution in time. Moreover, it is also a good test for a numerical scheme's ability to conserve certain quantities such as energy, momentum and angular momentum, since no viscosity or forcing is present, and the boundaries do not play a role (unless significant error causes nonzero velocity to creep out to the boundary). A plot of the true velocity solution is shown in Figure 3.1.

We compute solutions to the Gresho problem using the different formulations, together with Crank-Nicolson time stepping (using Newton's method to solve the nonlinear problem at each time step), with $f = 0$, $\nu = 0$, and no-penetration boundary conditions up to $T = 4$. We computed

using (P_2, P_1) Taylor-Hood elements on a 24x24 uniform mesh and a time step of $\Delta t = 0.01$.

Plots of energy, momentum, angular momentum, and L^2 velocity error versus time are shown in Figure 3.2.

3.3.1.1 Summary of results

EMAC, skew-symmetric and rotational schemes conserve kinetic energy. EMAC and skew-symmetric schemes conserve linear momentum. EMAC is the *only scheme to conserve angular momentum to $t = 4$* . EMAC scheme has significantly better $L^2(\Omega)$ error than all the other methods. The *conservative* scheme gives by far the worst results. Kinetic energy of *conservative* and *convective* formulations are blowing up, which causes the nonlinear solver to fail. We note that all the results for conserved quantities are consistent with the theory of the previous section, and in particular the EMAC scheme is the only one to conserve each of energy, momentum and angular momentum.

3.3.2 Channel flow around a cylinder

Our next experiment tests the algorithms above on the flow around a cylinder benchmark problem, taken from [28, 50]. The domain for the problem is a 2.2×0.41 rectangular channel with a circle (cylinder) of radius 0.05 centered at $(0.2, 0.2)$, see Figure 3.3.

No slip boundary conditions are enforced on the walls and cylinder, and the time dependent inflow profile is taken to be

$$\begin{aligned} u_1(0, y, t) &= u_1(2.2, y, t) = \frac{6}{0.41^2} \sin(\pi t/8) y(0.41 - y), \\ u_2(0, y, t) &= u_2(2.2, y, t) = 0, \end{aligned}$$

and a zero-traction outflow condition is weakly enforced. The viscosity is set as $\nu = 10^{-3}$ and there is no external force, $f = 0$.

This problem is well studied, and it is known that as the flow rate increases, two vortices start to develop by $T = 4$ behind the cylinder. They then separate into the flow, and soon after a vortex street forms which can be visible through $t = 8$. Reference values for lift and drag coefficients,

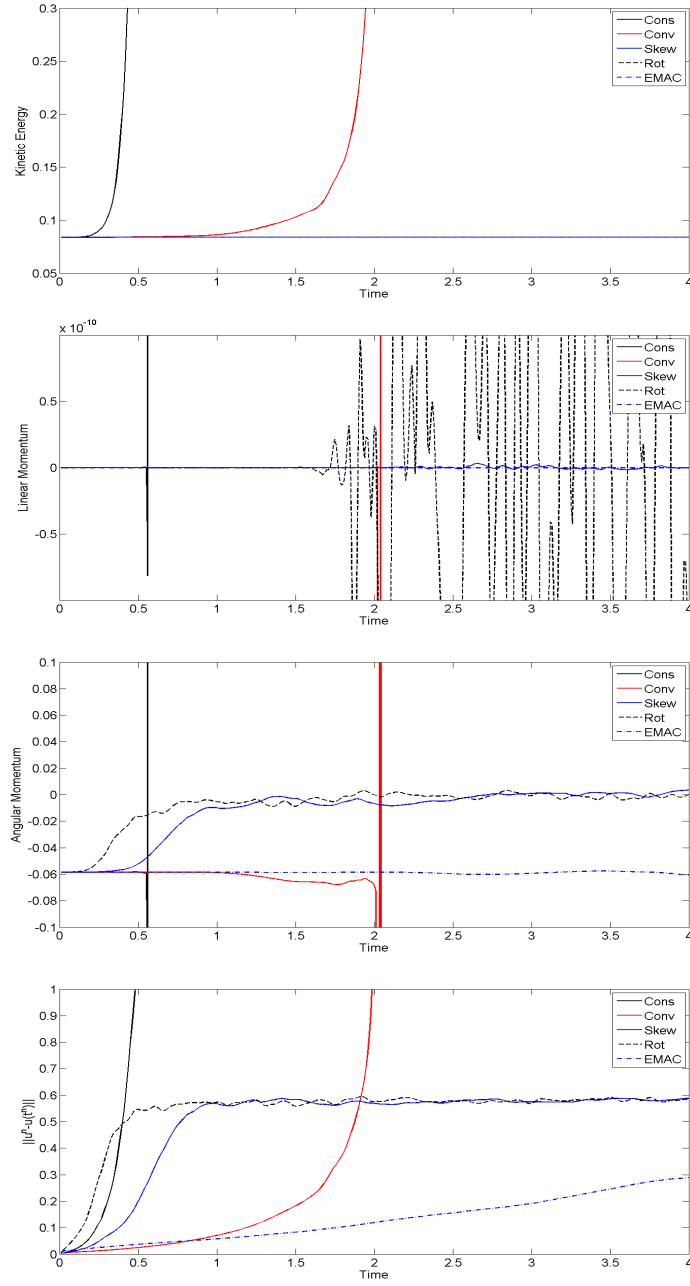


Figure 3.2: Shown above are figures of time versus kinetic energy, linear momentum, angular momentum, and $L^2(\Omega)$ velocity error, for the various formulations in the Gresho problem.

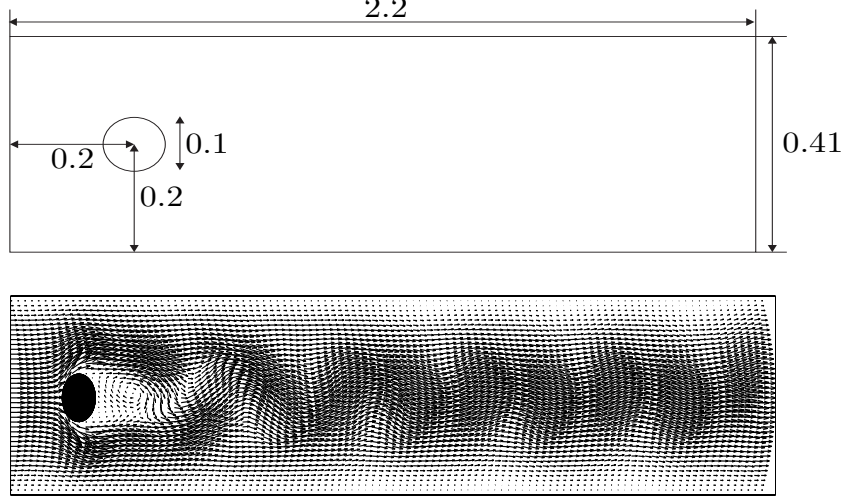


Figure 3.3: Shown above is the channel flow around a cylinder domain (top), and a resolved velocity field at $t = 6$.

and for pressure drop across the cylinder at $t = 8$ are given in [28] as

$$c_{d,max}^{ref} = 2.95092, \quad c_{l,max}^{ref} = 0.47795, \quad \Delta p^{ref} = -0.11160.$$

Method	$\dim(X_h)$	Δt	c_d^{max}	$ error $	c_l^{max}	$ error $	$\Delta p(8)$	$ error $
ROT	34,762	0.005	2.94442	6.48E-3	0.412069	6.59E-2	-0.11168	8.20E-5
CONV	34,762	0.005	2.94672	4.18E-3	0.470062	7.94E-3	-0.11176	1.62E-4
SKEW	34,762	0.005	2.94678	4.12E-3	0.467538	1.05E-2	-0.11177	1.70E-4
CONS	34,762	0.005	2.94667	4.25E-3	0.450239	2.77E-2	-0.11179	1.90E-4
EMAC	34,762	0.005	2.94819	2.71E-3	0.525675	4.77E-2	-0.11166	5.68E-5
ROT	61,694	0.005	2.94638	4.52E-3	0.484486	6.49E-3	-0.11139	2.10E-4
CONV	61,694	0.005	2.94893	1.97E-3	0.478282	2.82E-4	-0.11159	1.13E-5
SKEW	61,694	0.005	2.94892	1.98E-3	0.477249	7.51E-4	-0.11158	2.15E-5
CONS	61,694	0.005	2.94891	1.99E-3	0.477013	9.37E-4	-0.11149	1.10E-4
EMAC	61,694	0.005	2.94961	1.29E-3	0.490655	1.27E-2	-0.11119	4.06E-4
ROT	95,738	0.005	2.94919	1.71E-3	0.480021	2.02E-3	-0.11186	2.64E-4
CONV	95,738	0.005	2.94966	1.24E-3	0.478567	5.67E-4	-0.11155	5.00E-5
SKEW	95,738	0.005	2.94966	1.24E-3	0.478106	1.06E-4	-0.11154	6.04E-5
CONS	95,738	0.005	2.94966	1.24E-3	0.477831	1.19E-4	-0.11155	5.00E-5
EMAC	95,738	0.005	2.94986	1.04E-3	0.484425	6.43E-3	-0.11141	1.93E-4

Table 3.1: The Maximum lift and drag coefficients, and the pressure drop across the cylinder at $t = 8$, for the various formulations, using (P_2, P_1) elements.

We computed solutions using several meshes with Taylor-Hood elements, BDF3 time step-

ping, and time step $\Delta t = 0.005$ (we also used $\Delta t = 0.01$ and obtained very similar results). Results for the maximum lift and drag, as well as for the $t = 8$ pressure drop are shown in Table 3.1. For each mesh, the best errors are made bold for each statistic. We observe that in each case, the EMAC formulation provides the best prediction of the maximum drag coefficient, convective and skew-symmetric forms provide the best maximum lift coefficient prediction, and the EMAC, convective and conservative provide the best predictions of pressure drop error. Overall, the methods give rather similar predictions, and it is fair to say the methods are comparable for this test problem with these discretizations.

3.3.3 Channel flow past a flat plate at Re=100

Our next test is for channel flow past a flat plate with Re=100, following [45, 46]. The domain of this test problem is a $[-7, 20] \times [-10, 10]$ rectangle channel with a 0.125×1 flat plate placed 7 units into the channel, and vertically centered. The inflow velocity is set as $u_{in} = \langle 1, 0 \rangle$, we use a zero-traction outflow, and there is no forcing, $f = 0$. No-slip conditions are enforced on the walls and plate. A diagram of the test setup is shown in Figure 3.4.

We compute results using the convective, conservative, skew-symmetric, rotational, and the EMAC formulations, with BDF3 time stepping. The simulations all used BDF3 time stepping, a Delaunay mesh with (P_2, P_1) elements (which provided 58,485 total degrees of freedom) for each simulation. This is a fairly coarse mesh, and we use it to observe differences between the formulations (since as $h \rightarrow 0$, the formulations will all converge to each other). The simulations all used the same time step size of $\Delta t = 0.02$, and were started from rest, ran until a periodic-in-time state was reached, and then ran for an additional 16 periods. Periods were determined using the drag coefficient

$$C_d(t^m) = \frac{2}{\rho L U_{max}^2} \int_S \left(\rho \nu \frac{\partial u_{t_S}(t^m)}{\partial n} n_y - p_h^m n_x \right) ds.$$

Here, S is the plate, $n = \langle n_x, n_y \rangle$ is the outward normal vector, $u_{t_S}(t^m)$ is the tangential velocity of u_h^m , the density $\rho = 1$, the max velocity at the inlet $U_{max} = 1$, and $L = 1$ is the length of the plate.

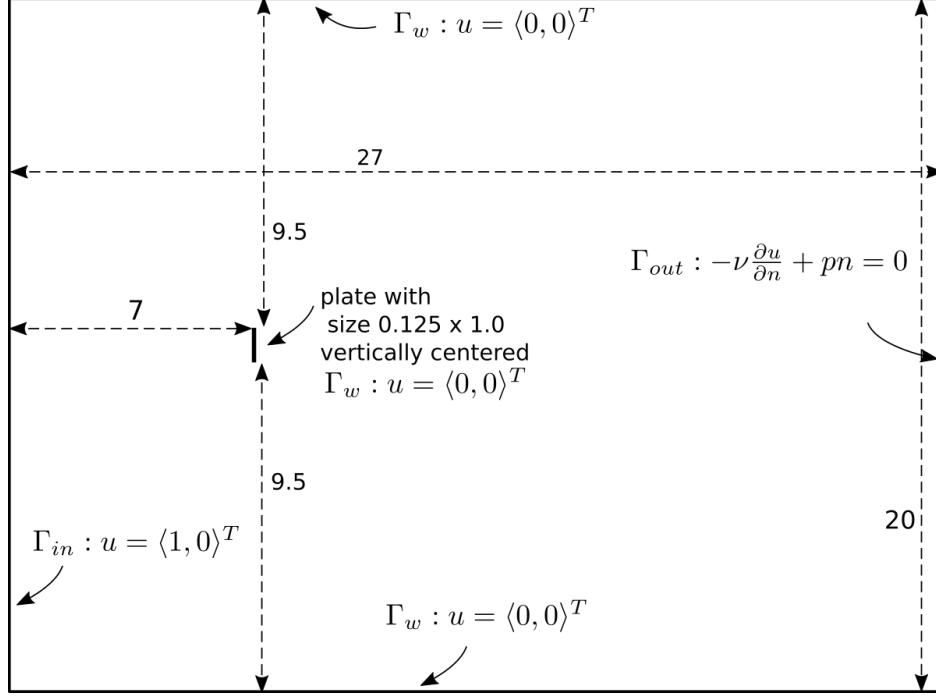


Figure 3.4: Setup for the flow past a normal flat plate.

The statistics of interest are the average drag coefficient, and the recirculation point of the time averaged velocity; all averages were taken over the last 16 periods. Results for these statistics are shown in table 3.2, along with results from a very fine discretization we obtained using the deal.II software [7] and (Q_2, Q_1) elements with the convective formulation and BDF2, using $\Delta t = 0.005$ and 4,019,895 total degrees of freedom (for which we assume is a convergent result, since it was very similar to results computed with $\Delta t = 0.01$ and about 2 million total degrees of freedom). For further comparison, we also give results of Saha from [45, 46], who used a MAC scheme with 426x162 cells (16x50 grid points on the plate surface), and a typical time step size of 5E-4.

We note first that the rotational and conservative schemes did not run to completion: the rotational simulation became unstable around $T = 25$, and before $T = 26$ the energy grows to 1E+100; similarly, the conservative scheme gives energy blowup at about $T = 78$. The EMAC solution's average drag most closely matches that of the very fine discretization, and is significantly closer than that of the convective and skew-symmetric solutions. For the recirculation point, the convective, EMAC, and skew-symmetric formulations give results with similar accuracy.

Formulation	Re	Average C_d	Recirculation point
CONV	100	2.5434	1.1577
EMAC	100	2.6598	1.1648
SKEW	100	2.5903	1.1565
ROT	100	failed: energy blows up at $T = 25$	
CONS	100	failed: energy blows up at $T = 78$	
Very fine discretization	100	2.6454	1.1373
Saha [46]	100	2.43	1.11
Saha [45]	100	2.60	(not given)

Table 3.2: Shown above are the average drag coefficient and x-coordinate of the recirculation point for simulations of flow past a flat plate with varying formulations, together with reference values from a DNS and from [45, 46].

3.4 Conclusions

We have developed a new discrete formulation for the incompressible NSE, named the *EMA-conserving* (EMAC) formulation herein, which conserves energy, momentum, angular momentum, when the solenoidal constraint on the velocity is enforced only weakly. Moreover, we show that none of the commonly used *convective*, *conservative*, *rotational*, and *skew-symmetric* formulations conserve each of energy, momentum, and angular momentum. Results of several numerical experiments have been provided which verify the discrete conservation properties of the EMAC scheme, and also show that it performs at least as good, or better, than the commonly used formulations.

Chapter 4

3D Channel Flows Past Cylinder

4.1 The test problem

The domain Ω is a 3D box with dimensions $0.41 \times 0.41 \times 2.5\text{m}$, and the obstacle is a circular cylinder with the diameter $D = 0.1\text{m}$. A diagram is shown in the figure 4.1. Here, we denote Γ_{walls} to be the bottom, left, right and top walls of the channel and the boundary of the cylinder, Γ_{in} to be the left boundary of the channel (inlet), and Γ_{out} to be the right boundary (outlet).

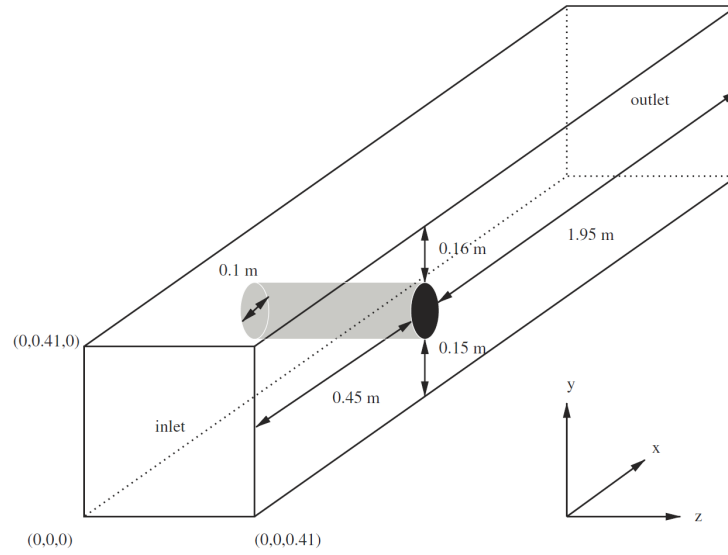


Figure 4.1: The channel with the circular cylinder.

4.2 Statistics of interest

In the paper [49], the Reynolds number for this problem is defined as

$$Re = \frac{\bar{U}D}{\nu}, \quad (4.1)$$

where

$$\bar{U} = \frac{4}{9}U_{max}$$

is mean inflow velocity, and ν is the kinematic viscosity of the fluid. In the definition of drag and lift coefficients we follow the paper [49]. The drag coefficient is defined as

$$c_d(t) = \frac{2}{\rho H \bar{U}^2 D} \int_S \left(\rho \nu \frac{\partial u_{t_s}(t)}{\partial n} n_y - p(t) n_x \right) dS$$

where $H = 0.41\text{m}$ is the height and the width of the channel, S denotes the boundaries of an obstacle, $n = (n_x, n_y)^T$ is normal vector on S directing into domain, $t_S = (n_y, -n_x)^T$ is a tangential vector on S , u_{t_S} is a tangential velocity ($u_{t_S} := t \cdot u$), where t is a tangent vector to S .

The lift coefficient is defined as

$$c_l(t) = -\frac{2}{\rho H \bar{U}^2 D} \int_S \left(\rho \nu \frac{\partial u_{t_s}(t)}{\partial n} n_x + p(t) n_y \right) dS$$

We compute the pressure drop in the way suggested in the paper [49],

$$\Delta P = P(x_a, y_a, z_a) - P(x_e, y_e, z_e), \quad (4.2)$$

where $(x_a, y_a, z_a) = (0.45, 0.20, 0.205)$ and $(x_e, y_e, z_e) = (0.55, 0.20, 0.205)$.

4.3 Sine inflow past circular cylinder

In the present section we consider the channel flow with circular cylinder and sine inflow boundary condition (the case “3D-3Z” described in [49]).

Consider the incompressible NSE:

$$\begin{aligned}
u_t - \nu \Delta u + (u \cdot \nabla)u + \nabla p &= f \text{ on } (0, T] \times \Omega, \\
\nabla \cdot u &= 0 \text{ on } (0, T] \times \Omega, \\
u(0, x) &= 0 \text{ on } \Omega, \\
(\nu \nabla u - pI) \cdot n|_{\Gamma_{out}} &= 0 \text{ on } (0, T], \\
u|_{\Gamma_{walls}} &= 0 \text{ on } (0, T],
\end{aligned}$$

where u is velocity, p is pressure, ν is the kinematic viscosity, f is an external force applied to the fluid, $U_m = 2.25$ m/s, $H = 0.41$ m. The time interval for numerical simulation is $0 < t \leq 8$ s.

The inlet flow profile is given for $0 \leq t \leq 8$ (the times of interest) as

$$u_x(0, y, z, t)|_{\Gamma_{in}} = \frac{16U_my z(H-y)(H-z)}{H^4} \sin\left(\frac{\pi t}{8}\right),$$

where $U_m = 2.25$ m/s, $H = 0.41$ m, and we enforce no slip boundary conditions on the walls and cylinder, and use a zero traction condition at the outflow. That the inlet is being forced periodically in time leads to $0 \leq Re(t) \leq 100$. We use the zero traction boundary condition at the outflow instead of a generally used Dirichlet boundary condition, because it is physically more correct. Thus it means that the total stress which the outflow boundary exerts on the fluid is equal to zero. Also in contrast to the Dirichlet boundary condition, the zero traction boundary condition makes no assumption on the velocity of a fluid at the outflow. The initial condition was taken to be the flow at rest, which corresponds to $t = 0$.

We compute with $((Q_2)^3, Q_1)$ elements on a quadrilateral mesh refined heavily around the cylinder. Next we discuss the choice of grad-div stabilization parameter γ . When grad-div parameter γ is significantly larger than 0.1, this makes it difficult to converge for the inner solve of the Schur complement. However, with grad-div parameter γ significantly larger than 0.1, this makes it difficult to converge for the outer solve of the Schur complement. Therefore a choice of grad-div parameter of $\gamma = 0.1$ seems to be reasonable, and was used for all simulations. The

runs take up to 72 hours, using between 120 and 1460 cores on the Palmetto cluster at Clemson University.

4.3.1 Newton method derivation

We solve full nonlinear NSE problem at every time iteration. For this, we linearize the NSE using Newton method. In this section we derive the Newton iteration equations for the NSE.

Denote by $X = \begin{pmatrix} u \\ p \end{pmatrix}$. Let $N(u)$ denotes the nonlinear term in the NSE. We will use this general notation below, because derivation for all 5 schemes are very similar. Denote Navier-Stokes operator with BDF2 approximation of the time-derivative term $F(\cdot)$ by

$$F(X) = \begin{pmatrix} \frac{1}{\Delta t} \left(\frac{3}{2}u - 2u^n + \frac{1}{2}u^{n-1} \right) + N(u) - \nu \Delta u + \nabla p - f^{n+1} \\ \nabla \cdot u \end{pmatrix}, \quad (4.3)$$

where the upper index denotes time step number, and the lower index denotes Newton method iteration number. The Newton iteration is defined in the following way:

$$X_{k+1} = X_k - [\nabla F(X_k)]^{-1} F(X_k). \quad (4.4)$$

Denote

$$\delta X := X_{k+1} - X_k. \quad (4.5)$$

Multiply by $\nabla F(X_k)$ on both sides to get

$$[\nabla F(X_k)] \delta X = -F(X_k). \quad (4.6)$$

By definition of directional derivative,

$$\nabla F(X) \delta X := \lim_{\epsilon \rightarrow 0} \frac{F(X + \epsilon \delta X) - F(X)}{\epsilon}, \quad (4.7)$$

and now we obtain

$$F(X + \epsilon \delta X) - F(X) = \epsilon \begin{pmatrix} \frac{3}{2\Delta t}(\delta u) - \nu \Delta(\delta u) + \nabla(\delta p) + \frac{1}{\epsilon} [N(u + \epsilon \delta u) - N(u)] \\ \nabla \cdot (\delta u) \end{pmatrix}. \quad (4.8)$$

For convective form

$$\begin{aligned} N(u + \epsilon \delta u) - N(u) &:= (u + \epsilon \delta u) \cdot \nabla(u + \epsilon \delta u) - u \cdot \nabla u \\ &= \epsilon [u \cdot \nabla(\delta u) + (\delta u) \cdot \nabla u + \epsilon(\delta u) \cdot \nabla(\delta u)]. \end{aligned}$$

From above we obtain for convective form:

$$\nabla F(X_k) \delta X = \begin{pmatrix} \frac{3}{2\Delta t}(\delta u) - \nu \Delta(\delta u) + \nabla(\delta p) + u_k \cdot \nabla(\delta u) + (\delta u) \cdot \nabla u_k \\ \nabla \cdot (\delta u) \end{pmatrix}. \quad (4.9)$$

Thus for convective form and BDF2 approximation of the NSE, Newton method equations become the following:

$$\begin{aligned} \frac{3}{2\Delta t} u_{k+1} - \nu \Delta u_{k+1} + \nabla p_{k+1} + u_k \cdot \nabla u_{k+1} + u_{k+1} \cdot \nabla u_k \\ = u_k \cdot \nabla u_k + \frac{1}{\Delta t} \left(-2u^n + \frac{1}{2}u^{n-1} \right), \\ \nabla \cdot u_{k+1} = 0. \end{aligned}$$

Let $\phi_{p,i}$ be velocity test function, $\phi_{u,i}$ be pressure test function. Then the equations for Newton method for the NSE in weak form for the convective form becomes:

$$\begin{aligned} \frac{3}{2\Delta t} (\phi_{p,i}, u_{k+1}) + \nu (\nabla \phi_{p,i}, \nabla u_{k+1}) - (\nabla \cdot \phi_{p,i}, p_{k+1}) + (\phi_{p,i}, u_k \cdot \nabla u_{k+1} + u_{k+1} \cdot \nabla u_k) \\ - (\phi_{u,i}, \nabla \cdot u_{k+1}) = (\phi_{p,i}, u_k \cdot \nabla u_k) - (\phi_{p,i}, \frac{1}{\Delta t} (-2u^n + \frac{1}{2}u^{n-1})), \\ (\phi_{u,i}, \nabla \cdot u_{k+1}) = 0. \end{aligned}$$

Newton method equations for the NSE for other formulations are derived in a very similar way, by replacing the nonlinear term $N(u)$.

4.3.2 Discretization details

The elements used in our simulations are the lowest order Taylor-Hood [54], which are a very common choice. In deal.II these are (Q_2, Q_1) on quadrilateral meshes. We note these finite elements are known to be inf-sup stable [10].

4.3.2.1 Mesh generated with Gmsh software

The very first mesh we used was generated with software tool called 'Gmsh'. As one can see on figures 4.2, 4.3, this mesh leads to significant pressure fluctuations around the cylinder. We believe this is caused by a high disproportion between the sizes of cells, especially in those around the circular cylinder. Due to this issue we switched to another mesh generated with our C++ code, which we will discuss in the next section.

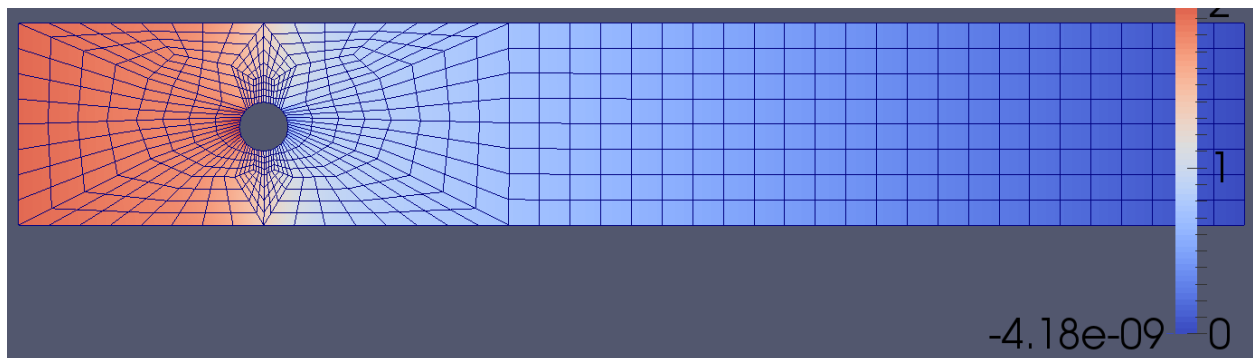


Figure 4.2: Mesh generated with Gmsh software on midplane.

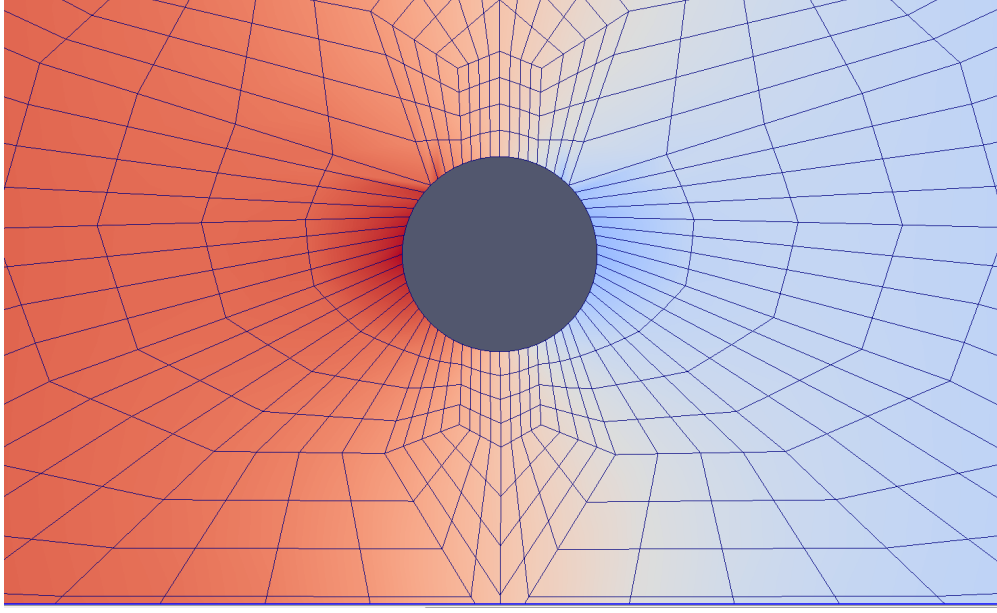


Figure 4.3: Mesh generated with Gmsh software, around circular cylinder.

4.3.2.2 Mesh Refinement algorithm

We start with coarse 2D mesh generated in C++ code shown on figure 4.4. Next we

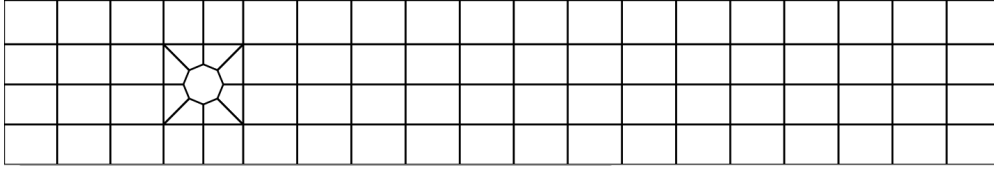


Figure 4.4: Coarse 2D mesh.

extrude the 2D mesh into 3D mesh, which is shown on figure 4.5. Then we refine cells around the cylinder 1 time. Next we carry out 2 global refinements of obtained 3D mesh. Finally, we carry out adaptive mesh refinement ‘on the fly’, that is at the second, third, and forth time steps using the solution obtained at previous time step. Introducing adaptive mesh refinement ‘on the fly’ significantly improved simulation accuracy at relatively low computational cost (by refining approximately 30% of cells per time step), comparing to global refinements.

The mesh on the midplane around the cylinder obtained by this approach is shown in figures 4.6 and 4.7. As one can see, side lengths of cells are now similar to each other, which is an advantage for example for linear solver and solution error. Cells are much smaller at the top

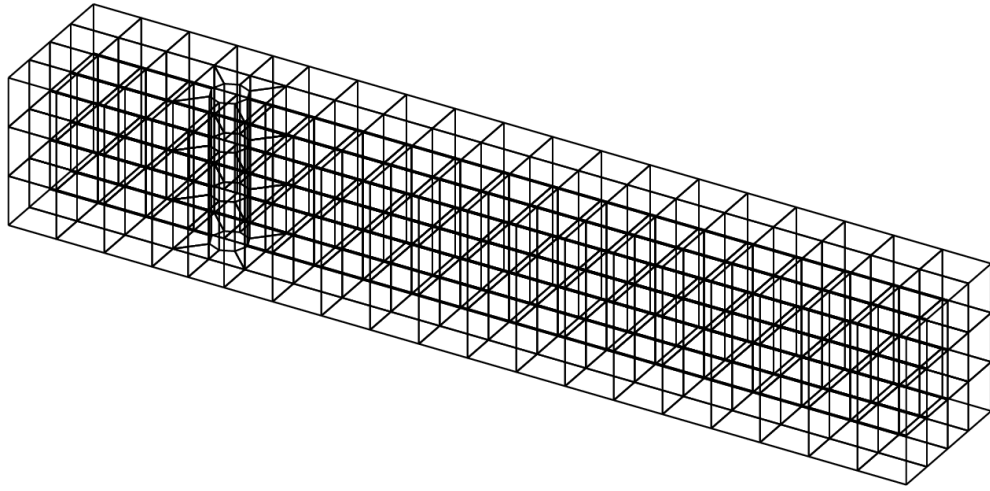


Figure 4.5: 3D mesh after extrusion.

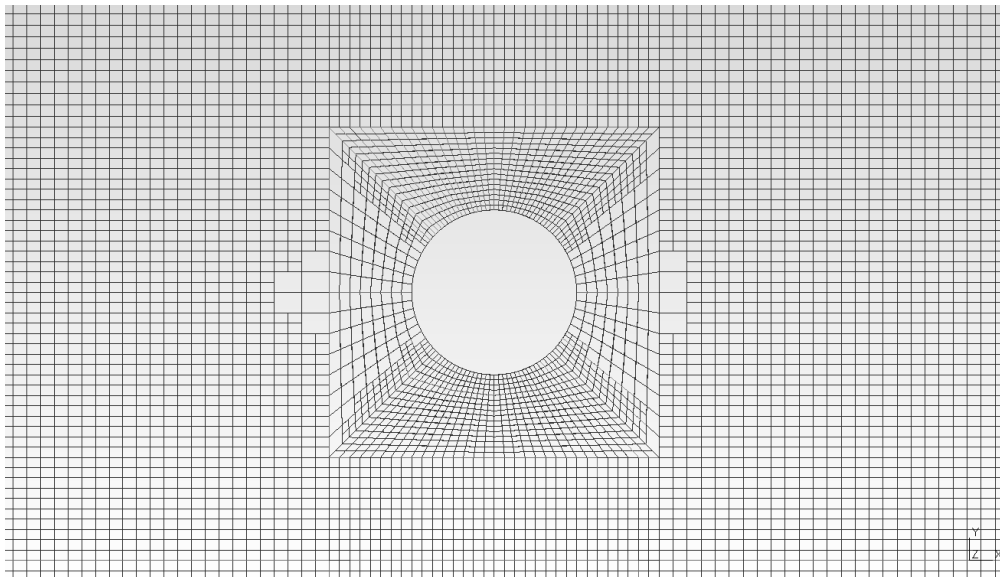


Figure 4.6: Refined mesh on midplane around the circular cylinder.

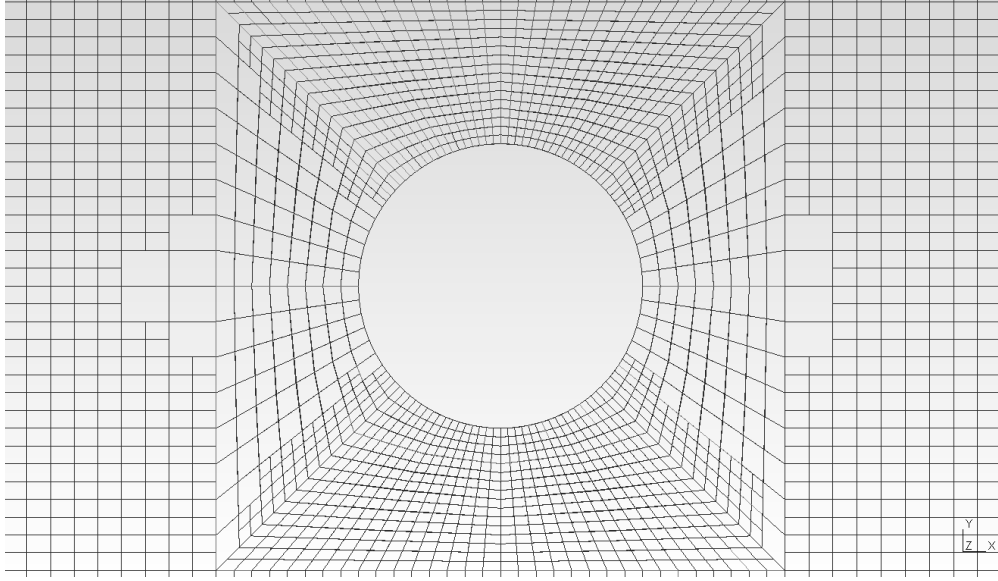


Figure 4.7: Refined mesh on midplane around the circular cylinder (closer to the cylinder).

and bottom of the cylinder, which is expected as we use adaptive refinement and norm of velocity gradient is larger there. The mesh is finer around the circular cylinder and gets coarser further from the circular cylinder, since the flow is most complicated close around the cylinder obstacle. For sine inflow boundary condition we carried out computational experiments for meshes with 23.5 million, 7.4 million and 2.29 million degrees of freedom.

4.3.3 Reference values from literature for sine inflow

In table 4.1 we report reference values for 3D channel flow past circular cylinder problem with sine inflow that we have found in the literature.

4.3.4 Computational results for sine inflow

In this section we show results obtained by numerical experiments for 3D channel flow past circular cylinder obstacle with sine inflow boundary condition.

4.3.4.1 All forms results with finest mesh

We report statistics for all five formulations computed with 23.5 million degrees of freedom in table 4.2, and statistics computed with 7.4 million degrees of freedom in table 4.3. The statistics

Scheme	Δt	DOF (K)	max drag	max lift	min lift
Lehrenfeld & Schöberl 2016, polynomial degree 5 [33]. Time-discretization: modified fractional-step- θ -scheme	0.004	939	3.29798	0.00278	-0.011054
Bayraktar, Mierka, Turek 2012. 3 rd order method [8] (Q_2/P_1^{disk})	0.005	89,760	3.2978	0.0028	-0.010999
Volker, John 2006 [29]		7,036	3.2968		-0.011
Schafer, Turek 1996 [49] (several research groups with different numerical methods)	Depends on research group	Depends on research group	[3.2, 3.3]	[0.002, 0.004]	

Table 4.1: Reference values from literature for 3D-3Z case

for 23.5 million degrees of freedom are very similar between the different formulations. Interestingly, even with 23.5 million degrees of freedom, the simulations appear to be not fully resolved spatially, as max drag and lift from [8, 33] predict max drag and lift to be ~ 3.2978 and 0.0028, respectively, and minimum lift to be -0.010999 using 3,145,728 cells (with 90 million total DOF) and $\Delta t = 0.005$. However, our goal here is to rather study how a choice of a scheme affects on the statistics. EMAC's scheme maximum drag is the closest to literature values both for 23.5 and 7.4 million degrees of freedom mesh. Maximum lift, minimum lift and minimum drag are almost the same for all schemes. They also match well corresponding statistics from the literature. However there are no reference values for minimum and maximum pressure drop.

Scheme	Δt	max drag	min drag	max lift	min lift	max ΔP	min ΔP
CONSERV	0.005	3.2716	-0.17081	0.002756	-0.01123	3.351	-0.1033
CONVECT	0.005	3.2727	-0.17082	0.002756	-0.0113	3.352	-0.1032
EMAC	0.005	3.2784	-0.17094	0.002755	-0.01164	3.356	-0.1029
ROT	0.005	3.2724	-0.17081	0.002756	-0.01106	3.345	-0.1034
SKEW	0.005	3.2722	-0.17082	0.002756	-0.01126	3.352	-0.1033

Table 4.2: Statistics for the 5 formulations, where the nonlinear problem is fully resolved at each time step. 23.5 million mesh DOF. $\Delta t = 0.005$. Results that are closest to literature values are in bold.

4.3.4.2 Results by scheme

In this section we show computational results for each of 5 schemes separately.

Scheme	max drag	min drag	min lift	max lift	ΔP_{max}	ΔP_{min}
CONS	3.24648	-0.170774	-0.01022	0.002753	3.345	-0.103599
CONV	3.24388	-0.170789	-0.01020	0.002753	3.346	-0.103568
EMAC	3.25593	-0.170797	-0.01035	0.002753	3.351	-0.103541
ROT	3.24108	-0.170805	-0.01012	0.002753	3.336	-0.103574
SKEW	3.24519	-0.170781	-0.01021	0.002753	3.345	-0.103583

Table 4.3: Statistics for the 5 formulations, where the nonlinear problem is fully resolved at each time step. 7.42 million mesh DOF. $\Delta t = 0.005$. Results that are closest to literature values are in bold.

outflow BC	Δt	DOF	C_d^{max}	C_d^{min}	C_l^{max}	C_l^{min}
No stress	0.01	7410378	3.2351	-0.1733	0.002752	-0.0100
No stress	0.01	23576690	3.2691	-0.1732	0.002756	-0.0110
No stress	0.005	2289362	3.2296	-0.1708	0.002751	-0.0099
No stress	0.005	7419803	3.2411	-0.1708	0.002753	-0.0101
No stress	0.005	23516262	3.2724	-0.1708	0.002756	-0.0111
No stress	0.0025	7422017	3.2617	-0.1683	0.002757	-0.0111
No stress	0.00125	7413223	3.2651	-0.1690	0.002757	-0.0111
Dirichlet	0.005	7409020	3.2426	-0.1709	0.002753	-0.0102

Table 4.4: Statistics for the rotational formulation only, for different Δt and DOF, where the nonlinear problem is fully resolved at each time step. Part 1

outflow BC	Δt	DOF	ΔP_{max}	ΔP_{min}	drag range	lift range	$\Delta P_{max} - \Delta P_{min}$
No stress	0.01	7410378	3.334	-0.1056	3.4083	0.013	3.440
No stress	0.01	23576690	3.345	-0.1054	3.4423	0.014	3.450
No stress	0.005	2289362	3.333	-0.1035	3.4004	0.013	3.437
No stress	0.005	7419803	3.336	-0.1036	3.4119	0.013	3.440
No stress	0.005	23516262	3.345	-0.1034	3.4432	0.014	3.448
No stress	0.0025	7422017	3.344	-0.1014	3.4301	0.014	3.445
No stress	0.00125	7413223	3.343	-0.1019	3.4341	0.014	3.445
Dirichlet	0.005	7409020	3.336	-0.1037	3.4135	0.013	3.440

Table 4.5: Statistics for the rotational formulation only, for different Δt and DOF, where the nonlinear problem is fully resolved at each time step. Part 2.

In tables 4.4 and 4.5 we collect results for the rotational formulation only. From table 4.4 it follows that for the rotational formulation, the maximum drag converged in at least 2 digits, the minimum drag converged in 2 digits (after the decimal), the maximum lift converged in 5 digits (after the decimal), and the minimum lift converged in 3 digits (after the decimal). From table 4.5 it appears, that maximum pressure converged in 3 digits, minimum pressure converged in 2 digits (after the decimal).

outflow BC	Δt	DOF	C_d^{max}	C_d^{min}	C_l^{max}	C_l^{min}
No stress	0.01	7410802	3.2396	-0.1732	0.00275	-0.0100
No stress	0.01	23579480	3.2686	-0.1732	0.00276	-0.0112
No stress	0.005	2289362	3.2349	-0.1708	0.00275	-0.0100
No stress	0.005	7419112	3.2452	-0.1708	0.00275	-0.0102
No stress	0.005	23516262	3.2722	-0.1708	0.00276	-0.0113
No stress	0.0025	7422017	3.2622	-0.1683	0.00276	-0.0110
Dirichlet	0.005	7409020	3.2468	-0.1709	0.00275	-0.0103

Table 4.6: Statistics for the skew-symmetric formulation only, for different Δt and DOF, where the nonlinear problem is fully resolved at each time step.

outflow BC	Δt	DOF	ΔP_{max}	ΔP_{min}	drag range	lift range	$\Delta P_{max} - \Delta P_{min}$
No stress	0.01	7410802	3.344	-0.1056	3.4128	0.013	3.449
No stress	0.01	23579480	3.352	-0.1053	3.4418	0.014	3.457
No stress	0.005	2289362	3.342	-0.1035	3.4056	0.013	3.446
No stress	0.005	7419112	3.345	-0.1036	3.4160	0.013	3.449
No stress	0.005	23516262	3.352	-0.1033	3.4430	0.014	3.455
No stress	0.0025	7422017	3.352	-0.1015	3.4305	0.014	3.453
Dirichlet	0.005	7409020	3.345	-0.1037	3.4177	0.013	3.449

Table 4.7: Statistics for the skew-symmetric formulation only, for different Δt and DOF, where the nonlinear problem is fully resolved at each time step.

In tables 4.6 and 4.7 we show results for the skew-symmetric formulation only. From table 4.6 it follows, that for the skew-symmetric formulation the maximum drag converged in at least 2 digits, minimum drag converged in 2 digits (after the decimal), maximum lift converged in 4 digits (after the decimal), and minimum lift converged in 3 digits (after the decimal). From table 4.7 it appears, that maximum pressure converged in 3 digits, minimum pressure converged in 2 digits (after the decimal).

In tables 4.8 and 4.9 we show results for the convective formulation only. From table 4.8 it

outflow BC	Δt	DOF	C_d^{max}	C_d^{min}	C_l^{max}	C_l^{min}
No stress	0.01	7410177	3.2379	-0.1733	0.00275	-0.0100
No stress	0.01	23579288	3.2688	-0.1732	0.00276	-0.0112
No stress	0.005	2289362	3.2330	-0.1708	0.00275	-0.0100
No stress	0.005	7419112	3.2439	-0.1708	0.00275	-0.0102
No stress	0.005	23516262	3.2727	-0.1708	0.00276	-0.0113
No stress	0.0025	7422017	3.2622	-0.1683	0.00276	-0.0110
Dirichlet	0.005	7409020	3.2454	-0.1709	0.00275	-0.0102

Table 4.8: Statistics for the convective formulation only, for different Δt and DOF, where the nonlinear problem is fully resolved at each time step. Part 1.

outflow BC	Δt	DOF	ΔP_{max}	ΔP_{min}	drag range	lift range	$\Delta P_{max} - \Delta P_{min}$
No stress	0.01	7410177	3.344	-0.1056	3.4112	0.013	3.449
No stress	0.01	23579288	3.352	-0.1053	3.4420	0.014	3.457
No stress	0.005	2289362	3.343	-0.1035	3.4038	0.013	3.446
No stress	0.005	7419112	3.346	-0.1036	3.4147	0.013	3.449
No stress	0.005	23516262	3.352	-0.1032	3.4435	0.014	3.456
No stress	0.0025	7422017	3.352	-0.1015	3.4305	0.014	3.454
Dirichlet	0.005	7409020	3.345	-0.1037	3.4163	0.013	3.449

Table 4.9: Statistics for the convective formulation only, for different Δt and DOF, where the nonlinear problem is fully resolved at each time step. Part 2

follows that for the convective formulation, the maximum drag converged in at least 2 digits, the minimum drag converged in 2 digits (after the decimal), the maximum lift converged in 4 digits (after the decimal), and the minimum lift converged in 3 digits (after the decimal). From table 4.9 it appears, that maximum pressure converged in 3 digits, minimum pressure converged in 2 digits (after the decimal).

outflow BC	Δt	DOF	C_d^{max}	C_d^{min}	C_l^{max}	C_l^{min}
No stress	0.01	7410234	3.2411	-0.1732	0.00275	-0.0100
No stress	0.01	23579751	3.2685	-0.1732	0.00276	-0.0112
No stress	0.01	70456859	3.2859	-0.1737	0.00277	-0.0112
No stress	0.005	2289362	3.2366	-0.1708	0.00275	-0.0100
No stress	0.005	7419112	3.2465	-0.1708	0.00275	-0.0102
Dirichlet	0.005	7409032	3.2481	-0.1709	0.00275	-0.0103
No stress	0.005	23516262	3.2716	-0.1708	0.00276	-0.0112
No stress	0.0025	7422017	3.2621	-0.1683	0.00276	-0.0110

Table 4.10: Statistics for the conservative formulation only, for different Δt and DOF, where the nonlinear problem is fully resolved at each time step.

outflow BC	Δt	DOF	ΔP_{max}	ΔP_{min}	drag range	lift range	$\Delta P_{max} - \Delta P_{min}$
No stress	0.01	7410234	3.344	-0.1056	3.4144	0.013	3.449
No stress	0.01	23579751	3.351	-0.1053	3.4417	0.014	3.457
No stress	0.01	70456859	3.341	-0.1054	3.4597	0.014	3.446
No stress	0.005	2289362	3.342	-0.1035	3.4074	0.013	3.446
No stress	0.005	7419112	3.345	-0.1036	3.4172	0.013	3.449
Dirichlet	0.005	7409032	3.345	-0.1037	3.4190	0.013	3.449
No stress	0.005	23516262	3.351	-0.1033	3.4425	0.014	3.455
No stress	0.0025	7422017	3.351	-0.1015	3.4304	0.014	3.453

Table 4.11: Statistics for the conservative formulation only, for different Δt and DOF, where the nonlinear problem is fully resolved at each time step.

In tables 4.10 and 4.11 we show results for the conservative formulation only. From table 4.10 it follows that for the conservative formulation, maximum drag converged in at least 2 digits, minimum drag converged in 2 digits (after the decimal), maximum lift converged in 4 digits (after the decimal), and minimum lift converged in 3 digits (after the decimal). From table 4.11 it appears that maximum pressure converged in 3 digits, and minimum pressure converged in 2 digits (after the decimal).

In tables 4.12 and 4.13 we show results for the EMAC formulation only. From table 4.12 it follows, that for the EMAC formulation maximum drag converged in at least 2 digits, minimum drag converged in 2 digits (after the decimal), maximum lift converged in 4 digits (after the decimal), and minimum lift converged in 3 digits (after the decimal). From table 4.13 it appears, that for the EMAC scheme the maximum pressure converged in 3 digits, the minimum pressure converged in 2 digits (after the decimal).

outflow BC	Δt	DOF	C_d^{max}	C_d^{min}	C_l^{max}	C_l^{min}
No stress	0.01	7410216	3.2501	-0.1733	0.00275	-0.0101
No stress	0.01	23579573	3.2749	-0.1733	0.00276	-0.0115
No stress	0.005	2289362	3.2459	-0.1708	0.00275	-0.0101
No stress	0.005	7419112	3.2559	-0.1708	0.00275	-0.0104
No stress	0.005	23516526	3.2784	-0.1709	0.00276	-0.0116
No stress	0.0025	7422017	3.2678	-0.1683	0.00276	-0.0110
Dirichlet	0.005	7409210	3.2576	-0.1709	0.00275	-0.0104

Table 4.12: Statistics for the EMAC formulation only, for different Δt and DOF, where the nonlinear problem is fully resolved at each time step. Part 1.

outflow BC	Δt	DOF	ΔP_{max}	ΔP_{min}	drag range	lift range	$\Delta P_{max} - \Delta P_{min}$
No stress	0.01	7410216	3.349	-0.1055	3.4234	0.013	3.455
No stress	0.01	23579573	3.356	-0.1050	3.4483	0.014	3.461
No stress	0.005	2289362	3.348	-0.1034	3.4167	0.013	3.451
No stress	0.005	7419112	3.351	-0.1035	3.4267	0.013	3.455
No stress	0.005	23516526	3.356	-0.1029	3.4493	0.014	3.459
No stress	0.0025	7422017	3.356	-0.1014	3.4361	0.014	3.458
Dirichlet	0.005	7409210	3.351	-0.1036	3.4285	0.013	3.455

Table 4.13: Statistics for the EMAC formulation only, for different Δt and DOF, where the nonlinear problem is fully resolved at each time step. Part 2

4.3.4.3 Evolution of statistics in time

Here we show how statistics (including drag, pressure drop, lift) change with respect to simulation time. Figure 4.8 shows evolution in time of the drag coefficient for the EMAC scheme

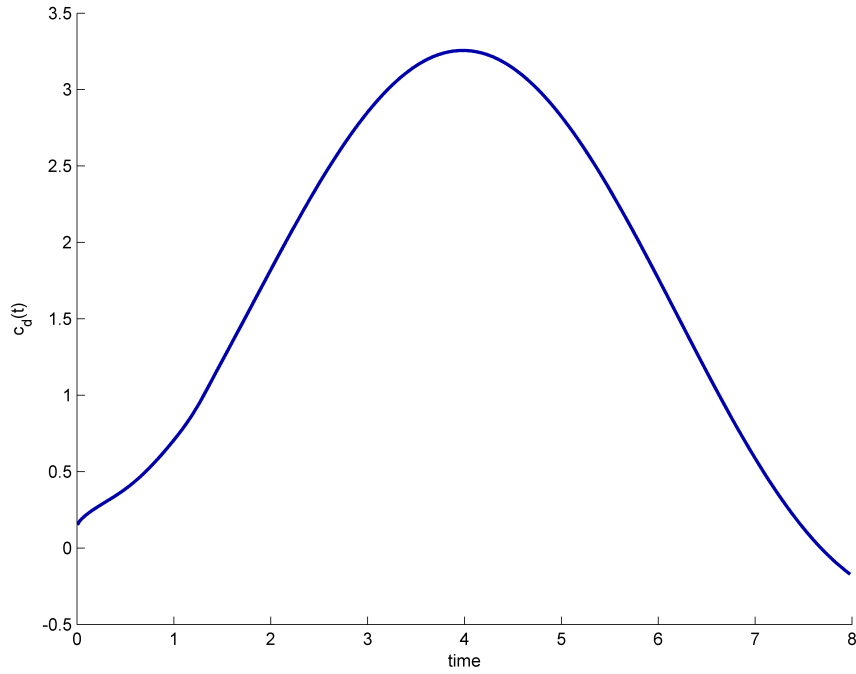


Figure 4.8: The drag coefficient in time for the EMAC scheme, $\Delta t = 0.005$.

with $\Delta t = 0.005$, and without a limit on the number of Newton iterations. Figure 4.9 shows evolution in time of the drag coefficient for the EMAC scheme with $\Delta t = 0.005$, and without a limit on the number of Newton iterations. Figure 4.10 shows evolution in time of pressure drop

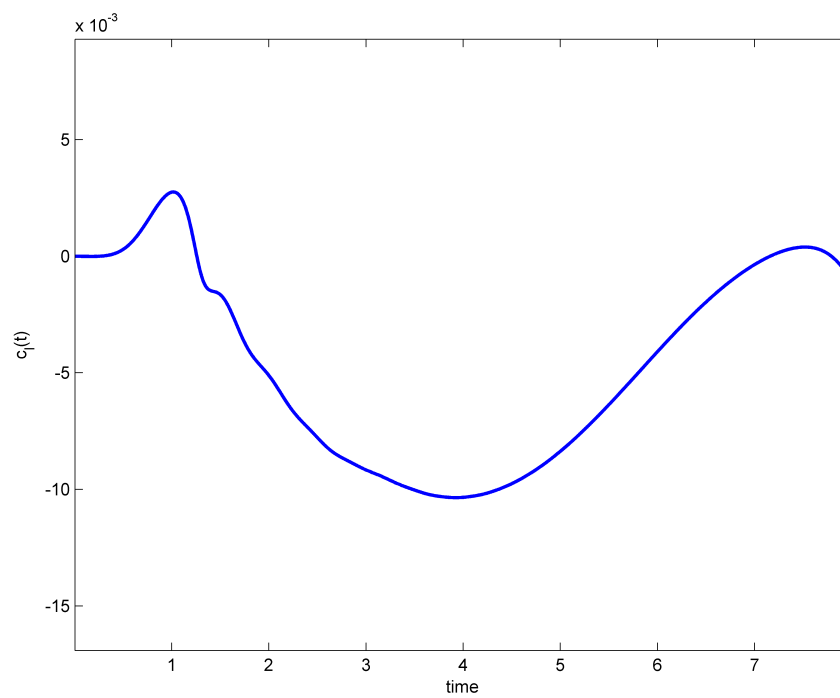


Figure 4.9: The lift coefficient in time for the EMAC scheme, $\Delta t = 0.005$.

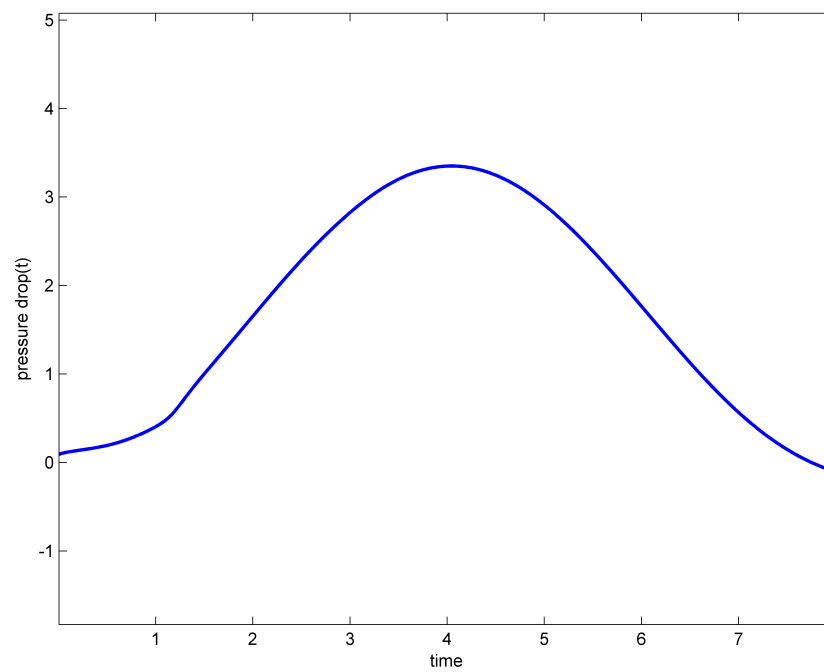


Figure 4.10: Pressure drop in time for the EMAC scheme, $\Delta t = 0.005$.

for EMAC scheme with $\Delta t = 0.005$, and without a limit on the number of Newton iterations. These figures match well with corresponding figures found in the literature (see for example paper of Schafer, Turek 1996 [49]).

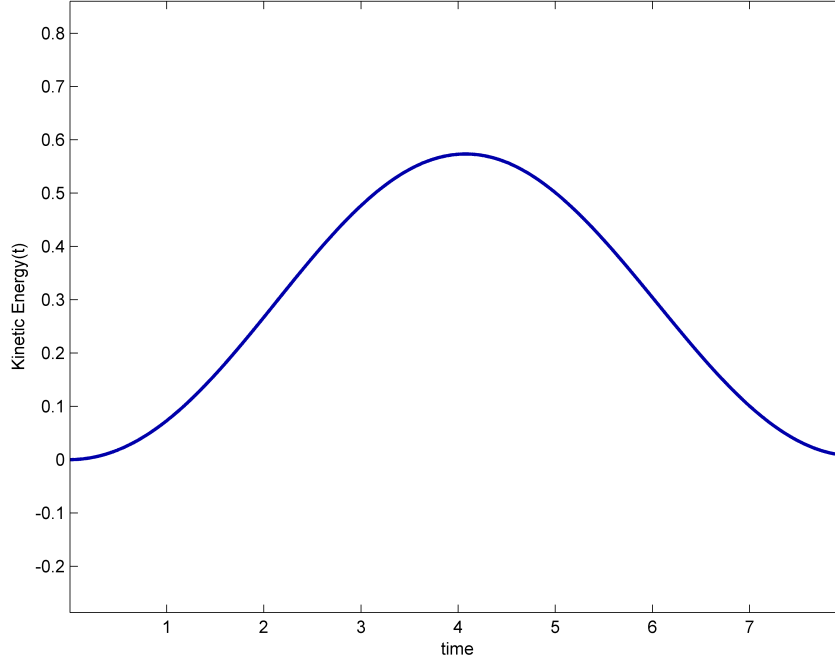


Figure 4.11: Kinetic Energy in time for the EMAC scheme, $\Delta t = 0.005$.

Figure 4.11 shows evolution in time of kinetic energy for EMAC scheme with $\Delta t = 0.005$, and without a limit on the number of Newton iterations. Kinetic energy is zero at $T = 0$ and $T = 8$, which matches well with sin inflow boundary condition, which is zero both at $T = 0$ and $T = 8$. Also from figure 4.11 one can see that kinetic energy is maximum at $T = 4$, which corresponds to the maximum inflow boundary condition.

Figure 4.12 shows evolution in time of linear momentum, and figure 4.13 shows evolution in time of angular momentum for EMAC scheme with $\Delta t = 0.005$.

Next we collect and compare statistics for all 5 schemes on line figures. On figure 4.14 we show the maximum drag coefficient for meshes with 2.29, 7.4 and 23.5 million degrees of freedom, and for all of EMAC, conservative, convective, rotational and skew-symmetric formulations. Paper [33] reports the maximum drag to be ~ 3.29798 computed with div-free finite elements of order 5,

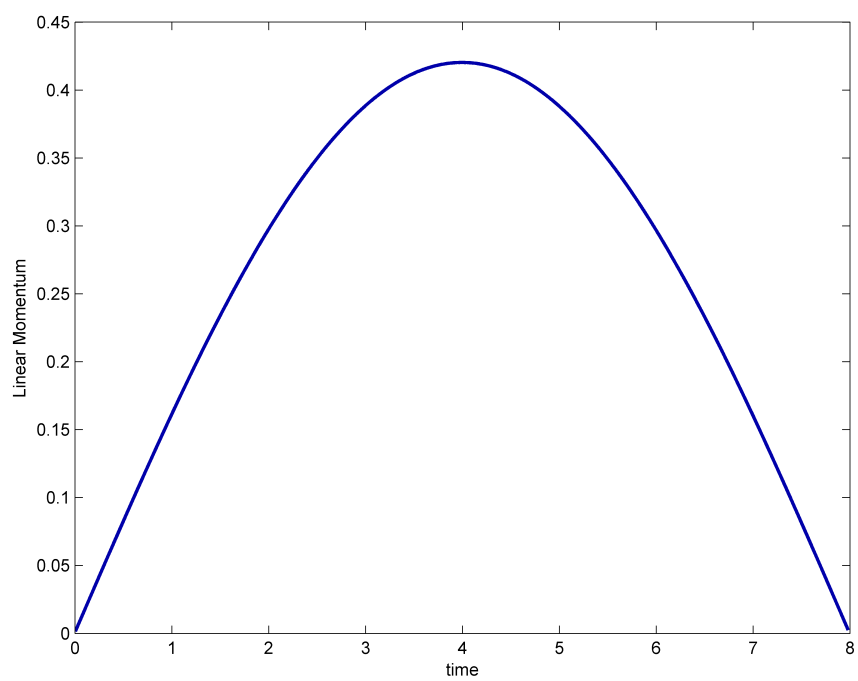


Figure 4.12: Linear Momentum in time for the EMAC scheme, $\Delta t = 0.005$.

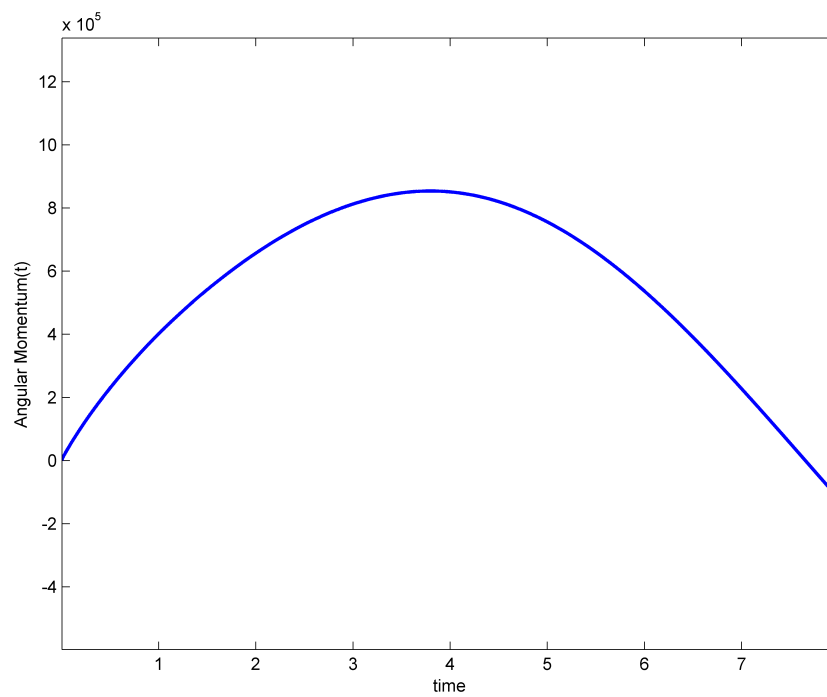


Figure 4.13: Angular Momentum in time for the EMAC scheme, $\Delta t = 0.005$.

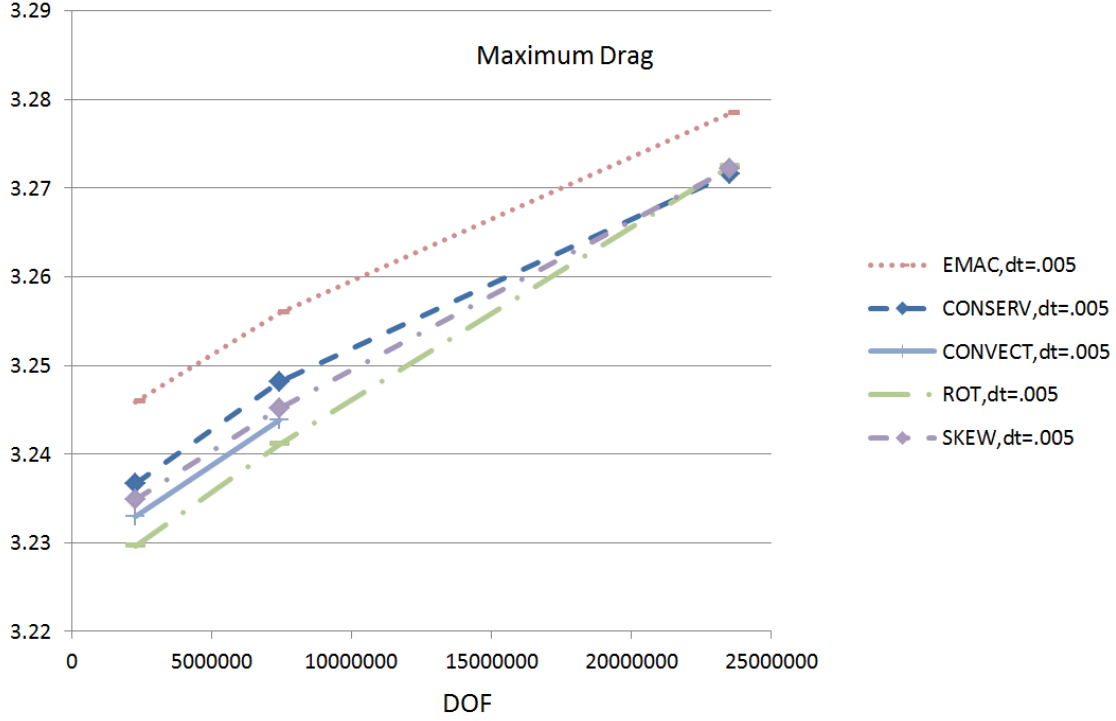


Figure 4.14: The maximum drag coefficient for all 5 schemes, for different meshes.

and paper [8] reports maximum drag to be ~ 3.2978 (with 90 million total degrees of freedom and $\Delta t = 0.005$). EMAC's prediction of the maximum drag coefficient is the closest of all 5 formulations to the above reference values for all meshes. For each mesh, the maximum drag coefficient of all 5 formulations differs only within 0.02. With the increase of mesh degrees of freedom to 23.5 million, the interval for the maximum of drag coefficient for all 5 formulations decreases to under 0.01.

On figure 4.15 we show the maximum lift coefficient for meshes with 2.29, 7.4 and 23.5 million degrees of freedom, and for all of EMAC, conservative, convective, rotational and skew-symmetric formulations. The maximum lift coefficient is almost the same for each particular mesh for all formulations. Paper [33] reports the maximum lift to be ~ 0.00278 computed with div-free finite element of order 5. Paper [8] reports the maximum lift to be ~ 0.0028 with 90 million total degrees of freedom and $\Delta t = 0.005$. All formulations predict the maximum lift coefficient with very similar precision. The maximum lift coefficient changes only in sixth digit with the increase of mesh degrees of freedom from 2.3 to 23.5 million.

On figure 4.16 we show the maximum pressure drop for meshes with 2.29, 7.4 and 23.5

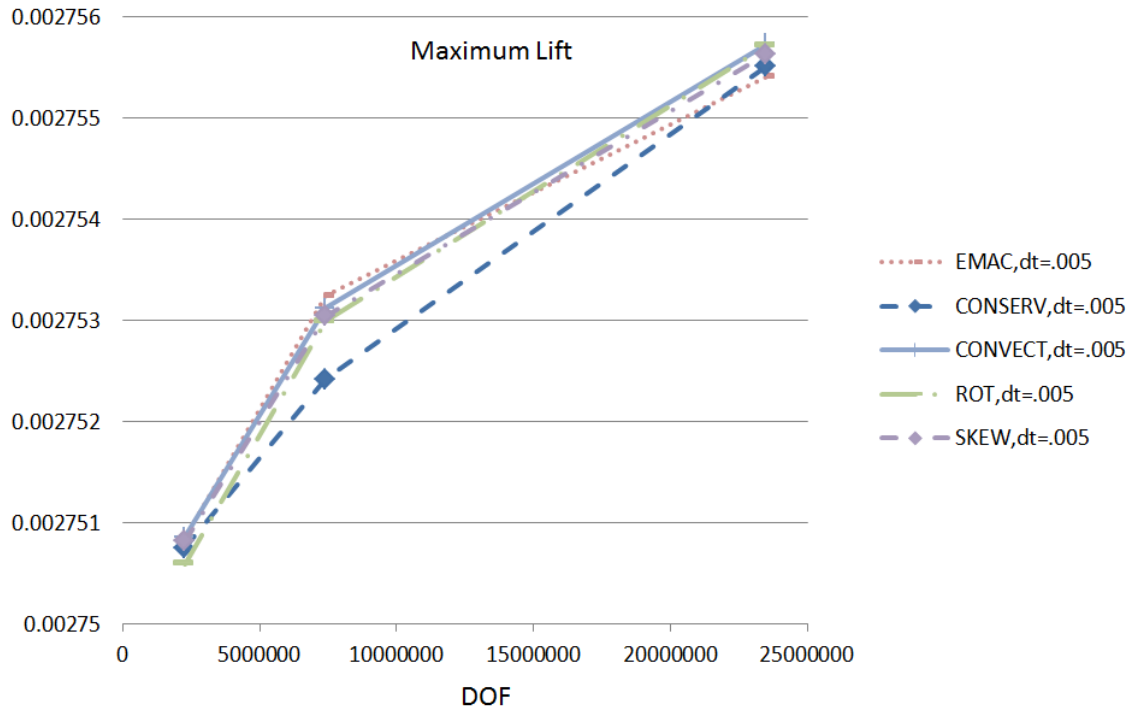


Figure 4.15: The maximum lift coefficient for all 5 schemes, for different meshes.

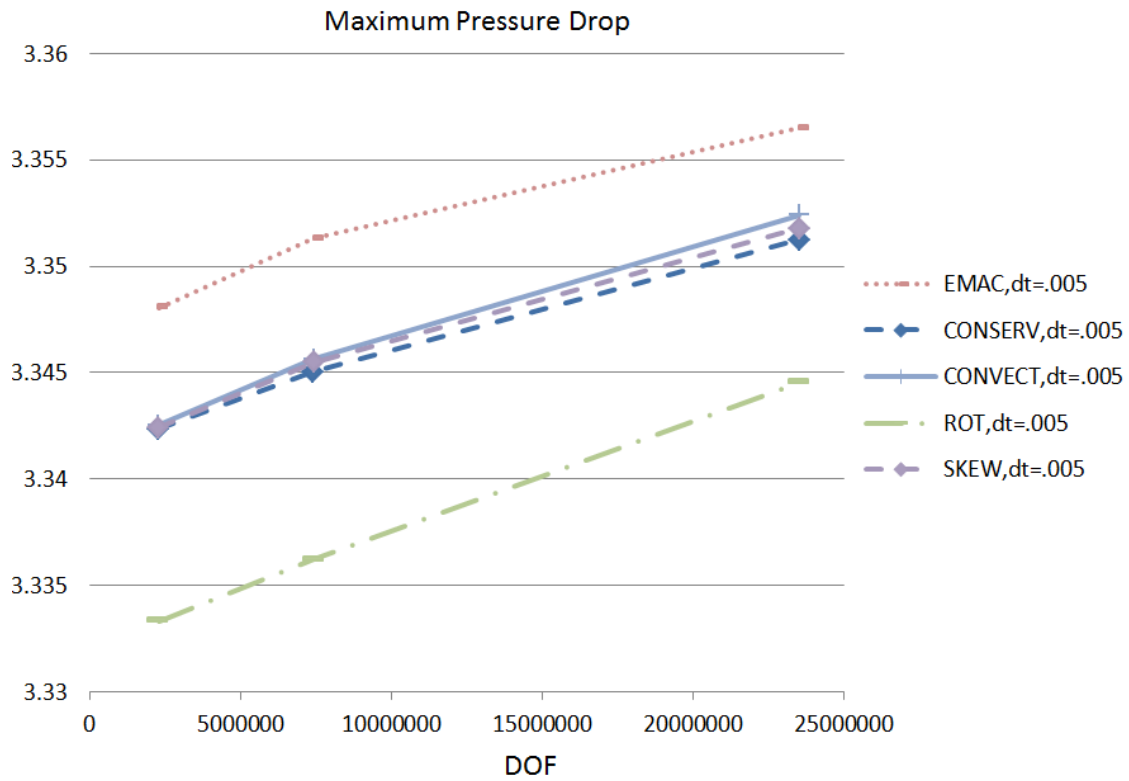


Figure 4.16: Maximum pressure drop for all 5 schemes, for different meshes.

million degrees of freedom, and for all of EMAC, conservative, convective, rotational and skew-symmetric formulations. Reference values for maximum pressure drop are not found in the literature. Therefore for evaluation of maximum pressure drop results, we will use maximum pressure drop from conservative scheme we computed with 70 million degrees of freedom (presented in table 4.11), which is 3.341. All schemes seems to perform equally comparing to this value.

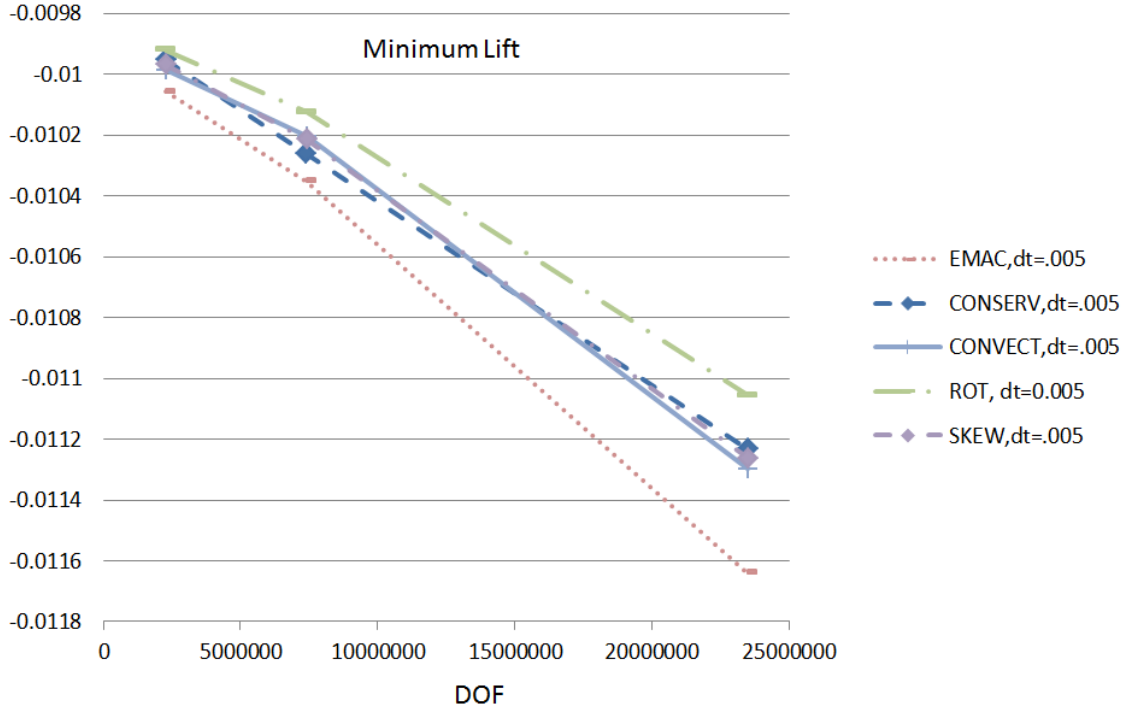


Figure 4.17: Minimum lift for all 5 schemes, for different meshes.

On figure 4.17 we show the minimum lift coefficient for meshes with 2.29, 7.4 and 23.5 million degrees of freedom, and for all of EMAC, conservative, convective, rotational and skew-symmetric formulations. Reference values for the minimum lift coefficient for 3D cylinder with sin inflow are not found in the literature. Therefore for evaluation of the minimum lift coefficient results, we will use the minimum lift coefficient from conservative scheme we computed with 70 million degrees of freedom, which is -0.1054 . All schemes seems to perform very similar comparing to this value.

Figure 4.18 shows iso-surfaces of vorticity magnitude in 3D together with streamlines that show trajectories of particles in time. Coloring is based on pressure. Iso-surfaces are chosen for the

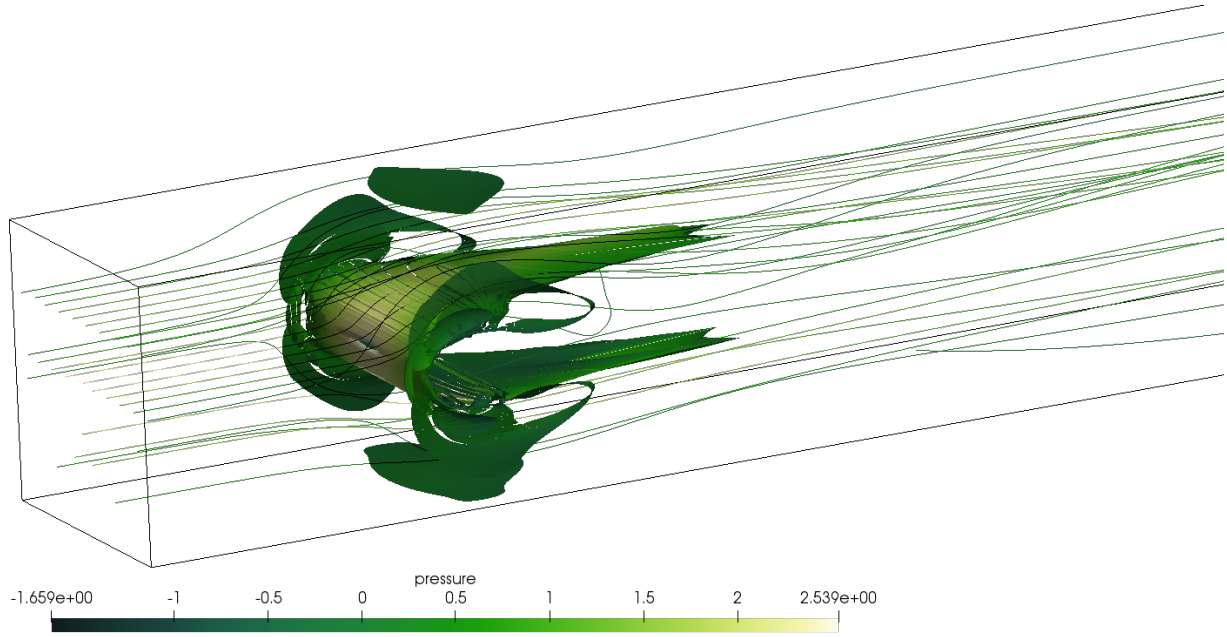


Figure 4.18: Vorticity iso-contours with streamlines at $T = 5$ sec for EMAC form. $\Delta t = 0.005$.

following vorticity magnitude values: 0, 54.625, 109.25, 163.875, 218.5, 273.125, 327.75, 382.375, 437, 491.625.

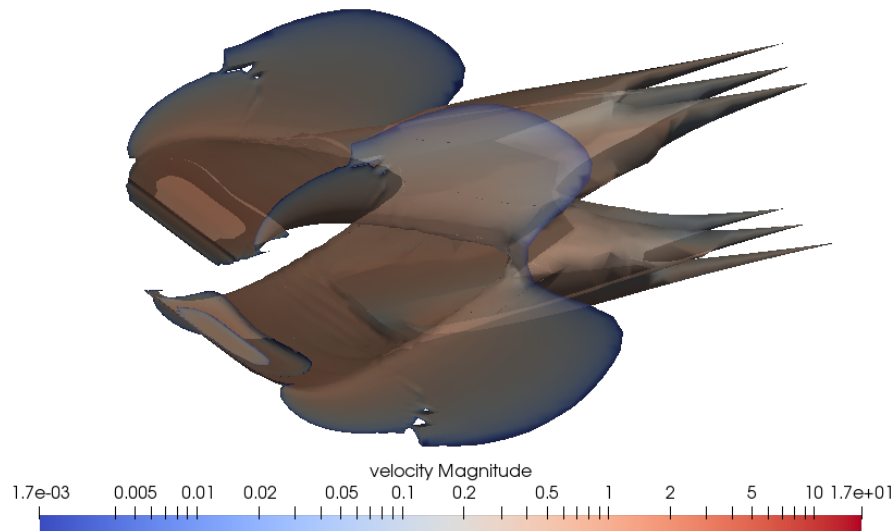


Figure 4.19: Pressure iso-contours in 3D

Figure 4.19 shows iso-surfaces of pressure in 3D at $T = 5$ sec for EMAC form with coloring based on velocity. Iso-surfaces are chosen for the following values of pressure: -1.698, -1.2237, -0.7495, -0.275.

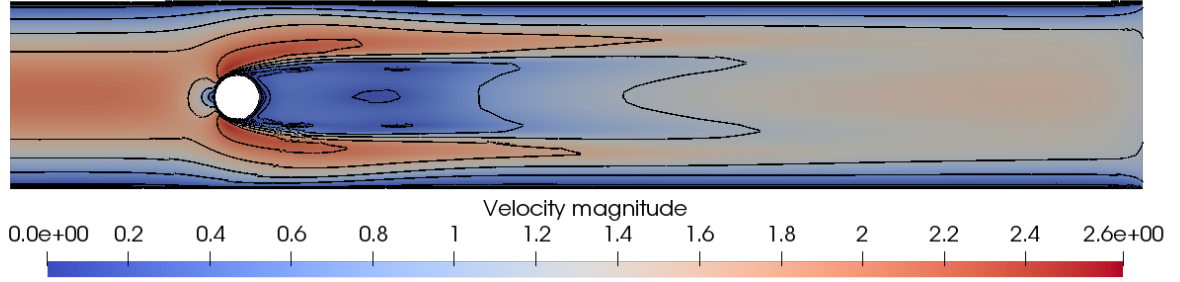


Figure 4.20: Velocity magnitude iso-contours on midplane at $T = 5$ sec.

Figure 4.20 magnitude of velocity iso-contours on midplane at $T = 5$ sec for EMAC form with coloring based on pressure. The midplane is passing through the center of the circular cylinder and is perpendicular to the axis of the cylinder. Iso-contours are chosen for the following values of velocity magnitude: 0.1975, 0.6708, 1.144, 1.617, 2.091, 0.1, 0.05, 0.02.

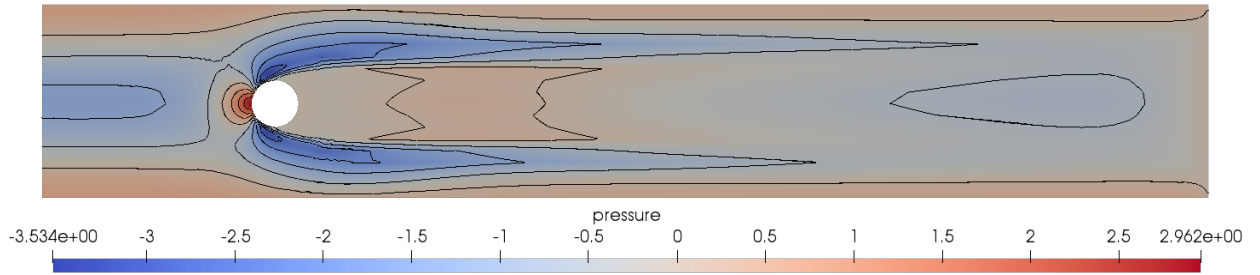


Figure 4.21: Pressure iso-contours on midplane.

Figure 4.21 pressure iso-contours on midplane at $T = 5$ sec for EMAC form with coloring based on pressure, and $\Delta t = 0.005$. Iso-contours are chosen for the following values of pressure: -3.534, -2.812, -2.09, -1.37, -0.646, 0.075, 0.797, 1.519, 2.24, 2.96.

4.3.4.4 EMAC linearizations

This section is from the work done by the author and collaborators in [14]. An important direction is to consider more efficient treatments of the *EMA-conserving* formulation. That is,

in this study, we have considered schemes that solve the nonlinear problem at each time step. However, it is typical with the more commonly used formulations to linearize the nonlinear term at each time step by approximating one of the velocities using previous time step solutions; such schemes need only one linear solve per time step, whereas schemes that resolve the full nonlinear problem with Newton’s method often require two or three.

We report statistics for the different limits on the number of nonlinear Newton iterations for EMAC formulation in table 4.14. It appears to be enough to do 2 Newton steps for the EMAC scheme, while a single Newton steps produces small variations in the statistics.

Scheme (EMAC)	max drag	min drag	min lift	max lift	ΔP_{max}	ΔP_{min}
Full nonlinear	3.25594	-0.17080	-0.01035	0.002753	3.351321	-0.103541
2-step Newton	3.25594	-0.17080	-0.01035	0.002753	3.351321	-0.103541
1-step Newton	3.25962	-0.17087	-0.00992	0.002762	3.352163	-0.103532

Table 4.14: EMAC statistics for 1, 2, and ‘as many as necessary’ Newton steps take at each time steps. 7.42 million mesh DOF. $\Delta t = 0.005$

Interestingly, at most 2 Newton iterations required to achieve the required solution tolerance for the full nonlinear EMAC problem. This explains why the statistics for ‘Full nonlinear’ and ‘2-step Newton’ are the same.

4.3.4.5 Mesh refinement algorithm, second approach

Statistics we obtained with numerical computations in the last section match very close the values found in the literature. Thus the maximum drag coefficient matches those found in the literature in 3 significant digits, but is about 0.01 different even when we used mesh with 70 million degrees of freedom (for conservative formulation), see for example paper of Braack and Richter [9]. Therefore we also carried numerical computations with another approach to mesh refinement, which leads to smaller cells right at the boundary of the circular cylinder, and is described below. First, we extrude code generated coarse 2D mesh into 3D mesh. Than we carry out 1 global refinement. Than we make several refinements of cells right at the boundary of the cylinder. Next we carry out an adaptive mesh refinement ‘on the fly’, that is we carry the adaptive mesh refinement at the second time iteration using the solution obtained at the first time iteration.

As one can notice, in this approach we changed the order of global mesh refinement and refinements of cells right at the boundary of the cylinder. Also we now carry out several refinements of cells right at the boundary of the cylinder, comparing to one such mesh refinement in the previous section. This approach allows to obtain cells with a very small diameter at the boundary of the cylinder while keeping total degrees of freedom relatively low.

Table 4.15 shows statistics computed with 22.5 million degrees of freedom, where mesh around the circular cylinder was refined 5 times.

Scheme	DOF	C_d^{max}	C_l^{max}	C_l^{min}	ΔP_{max}
CONSERV	22485976	3.3011	0.00277	-0.0112	3.344
CONVECT	22483776	3.3019	0.00277	-0.0113	3.348
EMAC	22564844	3.3045	0.00277	-0.0112	3.342
ROT	22492148	3.3041	0.00277	-0.0114	3.346
SKREW	22483792	3.3015	0.00277	-0.0113	3.346

Table 4.15: Statistics for the 5 formulations, where the nonlinear problem is fully resolved at each time step. Around 22.5 million mesh DOF. $\Delta t = 0.005$. Results that are closest to the literature values are in bold.

From table 4.15 we conclude that the maximum drag obtained by the current approach to mesh refinement with 22.5 million degrees of freedom, has difference from the maximum drag value obtained by Bayraktar, Mierka, Turek 2012 [8] with 3^{rd} order method with 90 million degrees of freedom has maximum difference among all 5 schemes at most 0.006688497. This difference with the maximum drag value in the literature is several times smaller than results obtained by previous approach to mesh refinement with 23.5 million degrees of freedom. Furthermore, the maximum drag values obtained by all 5 schemes lie within the narrow interval [3.301148455, 3.304488497]. We conclude that the accuracy of drag coefficient depends heavily on the size of cells right at the boundary of cylinder obstacle, even when total degrees is similar in different meshes. On the other hand, reference values for the maximum drag from the literature shown in table 4.1 are not consistent between authors in the third digit after the decimal. Due to above it is possible that the maximum drag values obtained by our computations is as close (or possibly closer) to the (unknown) true value of the maximum drag for this problem as the values from the literature. Based on results obtained with the approach to mesh refinement presented in the present and last section we give the following reference interval for the maximum drag [3.2716, 3.3045].

The maximum lift values obtained by all 5 schemes lie within the narrow interval $[0.002767976, 0.00277314]$. Thus the maximum lift for all 5 schemes coincide in 5 digits. Minimum lift values obtained by all 5 schemes lie within the interval $[-0.011394966, -0.01116685]$. Thus minimum lift for all 5 schemes coincide in 3 digits. Pressure drop values obtained by all 5 schemes lie within the interval $[3.341756726, 3.347657548]$.

4.3.5 Summary

A three-dimensional flow through a channel around a circular cylinder obstacle with time-independent inflow has been studied for all of rotational, skew-symmetric, convective, conservative and EMAC formulations. The evolution in time of the drag coefficient at the circular cylinder obstacle, the lift coefficient and the pressure drop have been studied.

In the present section, we obtained reference intervals for the maximum drag, the maximum lift and the pressure drop for the channel flow past circular cylinder with sin inflow and Reynolds number varying from 0 to 100. We carried out numerical computations with multiple meshes obtained by two completely different approaches to mesh refinement, and different time steps.

Our numerical results obtained by the first approach to mesh refinement matches very well with statistics obtained by the second approach to mesh refinement. Our results also match well with the corresponding statistics reported in the literature (see e.g. table 4.1).

4.4 Constant inflow past circular cylinder

In the present chapter we study channel flow with the same circular cylinder obstacle as in the previous chapter, but now sin inflow boundary condition is replaced with constant in time inflow boundary condition. The $Re = 20$ problem with constant inflow has been studied in [9, 29, 49], where this problem is shown to give a steady solution. We consider the case “3D-2Z” (described in [49]) with the inlet being forced constant in time leading to a $Re = 100$. In this section we compute and compare statistics for all of EMAC, conservative, convective, rotational and skew-symmetric schemes, for several different meshes and with different time steps. We will also study if a higher Reynolds number 100 lead to a time dependent solution.

Consider the incompressible NSE:

$$\begin{aligned}
u_t - \nu \Delta u + (u \cdot \nabla)u + \nabla p &= f \text{ on } (0, T] \times \Omega, \\
\nabla \cdot u &= 0 \text{ on } (0, T] \times \Omega, \\
u(0, x) &= 0 \text{ on } \Omega, \\
(\nu \nabla u - pI) \cdot n|_{\Gamma_{out}} &= 0 \text{ on } (0, T], \\
u(0, y, z, t)|_{\Gamma_{in}} &= \frac{16U_m yz(H-y)(H-z)}{H^4} \text{ on } (0, T], \\
u|_{\Gamma_{walls}} &= 0 \text{ on } (0, T],
\end{aligned}$$

where u is velocity, p is pressure, ν is kinematic viscosity, f is external force applied to the fluid, $U_m = 2.25$ m/s, $H = 0.41$ m. The time interval is $0 < t \leq 8$ s.

The inlet flow profile is given for $0 \leq t \leq 8$ (the times of interest) as

$$u_x(0, y, z, t)|_{\Gamma_{in}} = \frac{16U_m yz(H-y)(H-z)}{H^4},$$

where $U_m = 2.25$ m/s, $H = 0.41$ m, and we enforce no slip boundary conditions on the walls and cylinder, and use a zero traction condition at the outflow.

4.4.1 Computational results

4.4.1.1 All forms results with finest mesh

We report statistics for all five formulations computed at the last time iteration with ≈ 22.4 million degrees of freedom in table 4.16, and statistics computed with ≈ 7.2 million degrees of freedom in table 4.17.

Scheme	Δt	Mesh DOF	Drag at last time step	Lift at last time step	Pressure drop at last time step
CONSERV	0.005	22405401	3.291	-0.0099	3.349
SKEW	0.005	22394113	3.291	-0.0100	3.350
EMAC	0.005	22425516	3.291	-0.0103	3.349
CONVECT	0.005	22405303	3.291	-0.0100	3.350
ROT	0.005	22259684	3.289	-0.0100	3.350

Table 4.16: Statistics for the 5 formulations, where the nonlinear problem is fully resolved at each time step. 22.4 million mesh DOF. $\Delta t = 0.005$.

Scheme	Δt	Mesh DOF	Drag at last time step	Lift at last time step	Pressure drop at last time step
EMAC	0.005	7131438	3.281	-0.0109	3.369
ROT	0.005	7133772	3.280	-0.0107	3.351
CONSERV	0.005	7199301	3.283	-0.0102	3.350
CONVECT	0.005	7203358	3.283	-0.0103	3.350
SKEW	0.005	7206569	3.283	-0.0102	3.350

Table 4.17: Statistics for the 5 formulations, where the nonlinear problem is fully resolved at each time step. 7.2 million mesh DOF. $\Delta t = 0.005$.

Drag, lift and pressure drop at the last time iteration are almost the same for all schemes both for 22 and 7.2 million of degrees of freedom. Drag values computed by several research groups, and reported in the paper of Schäfer and Turek, 1996 [49], range from 3.225 to 3.792. Thus for 22.4 million degrees of freedom computed drag at last time iteration for all schemes belong to an interval from 3.2888 to 3.2915.

The lift coefficient values reported in [49], range from -0.0210 to 0.048. The drag and lift coefficient values we obtained with computed both with 22.4 million and 7.2 million degrees of freedom, and with all schemes are within the above intervals. Thus for 22.4 million degrees of freedom computed lift at last time iteration for all schemes belong to an interval from -0.0099 to -0.0103.

The computed pressure drop at the last time iteration for 22.4 million degrees of freedom for all schemes belong to an interval from 3.349 to 3.350. There are no reference values for $Re = 100$ for pressure drop for this problem with constant inflow in the literature.

4.4.1.2 Results by scheme

In this section we show computational results for each of 5 schemes separately. In table 4.18 we collect results for the conservative formulation only. From table 4.18 it follows, that for conservative formulation drag at the last time iteration converged in at least 2 digits. Thus increase of mesh degrees of freedom from 2.3 million to 22.4 million changed drag by less than 0.02. Lift at the last time iteration converged in 5 digits (after the decimal), and pressure drop converged in 3 digits.

Δt	Mesh DOF	Drag at last iteration	Lift at last iteration	Pressure drop at last iteration
0.005	2295555	3.274	-0.0099	3.358
0.0025	2282303	3.273	-0.0096	3.376
0.005	7199301	3.283	-0.0102	3.350
0.0025	7116164	3.281	-0.0103	3.366
0.005	22405401	3.291	-0.0099	3.349

Table 4.18: Statistics for the conservative formulation only for several different Δt and DOF, where the nonlinear problem is fully resolved at each time step.

In table 4.19 we collect results for the EMAC formulation only. From table 4.19 it follows, that for EMAC formulation drag at the last time iteration converged in at least 2 digits, lift at the last time iteration converged in 5 digits (after the decimal), and pressure drop converged in 3 digits.

Δt	Mesh DOF	Drag at last iteration	Lift at last iteration	Pressure drop at last iteration
0.005	2306538	3.273	-0.0100	3.391
0.0025	2293396	3.272	-0.0107	3.389
0.005	7131438	3.281	-0.0109	3.369
0.0025	7163775	3.280	-0.0103	3.353
0.005	22425516	3.291	-0.0103	3.349

Table 4.19: Statistics for the EMAC formulation only for several different Δt and DOF, where the nonlinear problem is fully resolved at each time step.

In table 4.20 we collect results for the rotational formulation only. From table 4.20 it follows, that

for rotational formulation drag at the last time iteration converged in at least 2 digits, lift at the last time iteration converged in 5 digits (after the decimal), and pressure drop converged in 3 digits.

Δt	Mesh DOF	Drag at last iteration	Lift at last iteration	Pressure drop at last iteration
0.005	2296327	3.274	-0.0102	3.357
0.0025	2285315	3.274	-0.0100	3.363
0.005	7133772	3.280	-0.0107	3.351
0.0025	7179341	3.281	-0.0104	3.350
0.005	22259684	3.289	-0.0100	3.350

Table 4.20: Statistics for the rotational formulation only for several different Δt and DOF, where the nonlinear problem is fully resolved at each time step.

In table 4.21 we collect results for the skew-symmetric formulation only. From table 4.21 it follows, that for skew-symmetric formulation drag at the last time iteration converged in at least 2 digits, lift at the last time iteration converged in 5 digits (after the decimal), and pressure drop converged in 3 digits.

Δt	Mesh DOF	Drag at last iteration	Lift at last iteration	Pressure drop at last iteration
0.005	2293693	3.273	-0.0099	3.358
0.0025	2281566	3.273	-0.0096	3.375
0.005	7206569	3.283	-0.0102	3.350
0.0025	7127873	3.281	-0.0101	3.366
0.005	22394113	3.291	-0.0100	3.350

Table 4.21: Statistics for the skew-symmetric formulation only for several different Δt and DOF, where the nonlinear problem is fully resolved at each time step.

As we already indicated, statistics for each scheme are converging, and furthermore statistics for all schemes seem to converge to the same values for drag, lift and pressure drop.

4.4.1.3 Evolution of statistics in time

In this section we show how statistics (including drag and lift coefficient, pressure drop) change with respect to simulation time.

Figure 4.22 shows the evolution in time of the drag coefficient for all schemes starting from $T = 0$, with $\Delta t = 0.005$, without a limit on the number of Newton iterations. Figure 4.23 shows the same

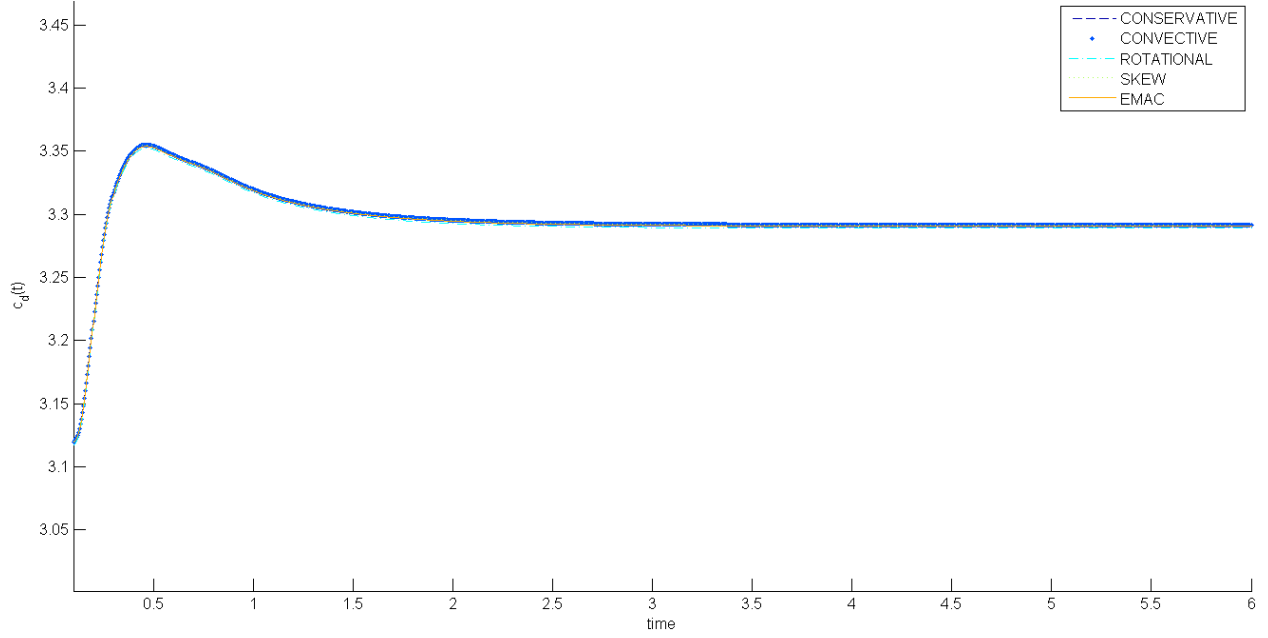


Figure 4.22: The drag coefficient for all schemes, start time $T = 0$

evolution in time of the drag coefficient, but starting from time $T = 1$. The evolution in time of the drag coefficient for all 5 schemes is very similar. Figure 4.22 shows that the drag coefficient becomes constant for all schemes at $T = 3.5s$. Figure 4.24 shows evolution in time of the lift

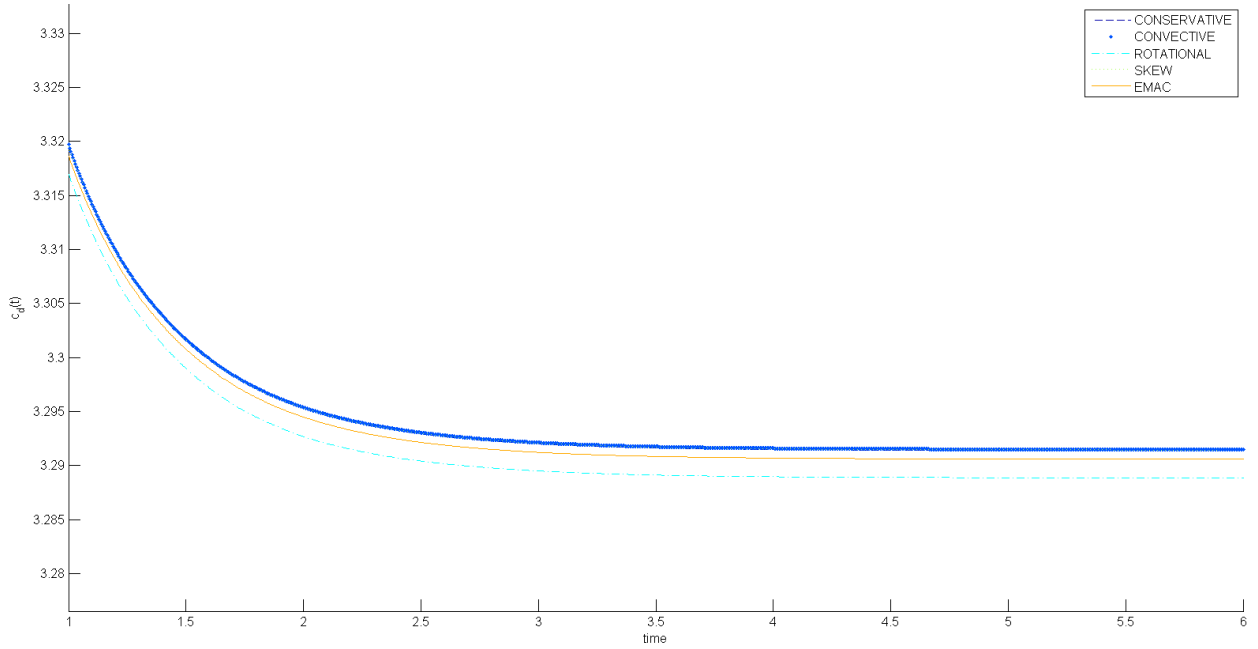


Figure 4.23: The drag coefficient for all 5 schemes, start time $T = 1$

coefficient for all schemes starting from $T = 0$, with $\Delta t = 0.005$, without a limit on the number of Newton iterations. Figure 4.25 shows the same evolution in time of the lift coefficient, but starting from time $T = 1$. The evolution in time of the lift coefficient for all 5 schemes is very similar. Figure 4.25 shows that the lift coefficient becomes constant for all schemes at $T = 3.5s$.

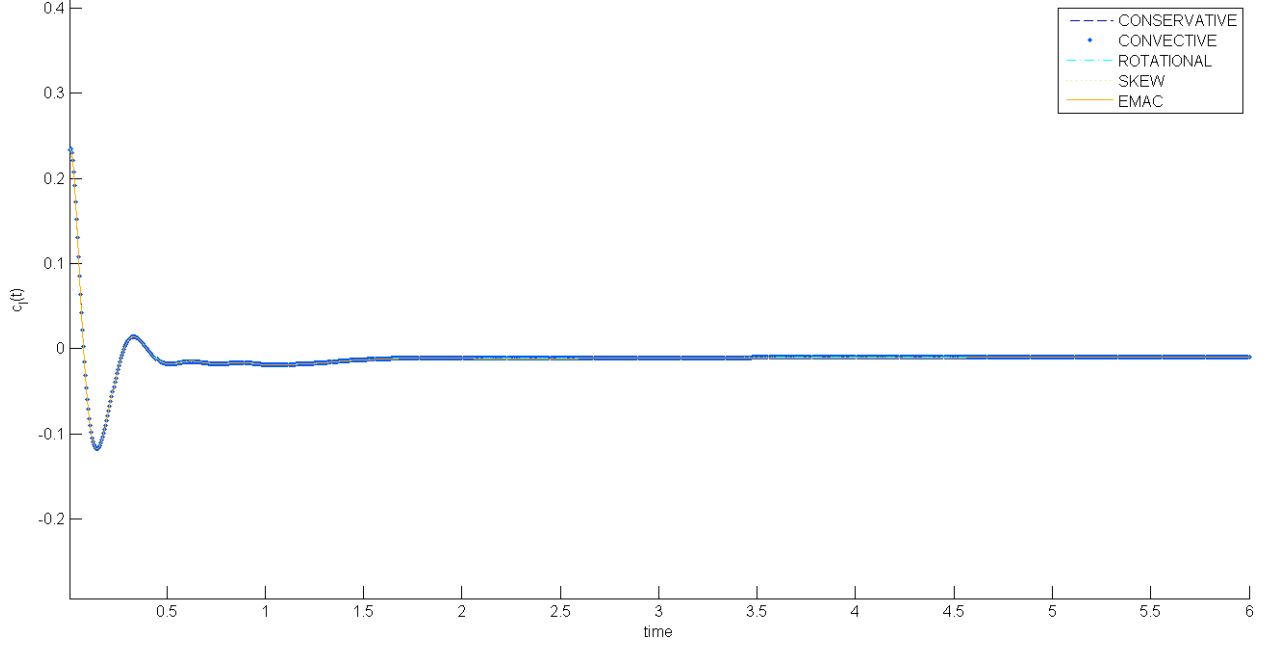


Figure 4.24: The lift coefficient for all 5 schemes, start time $T = 0$

Figure 4.26 shows the evolution in time of the pressure drop for all schemes starting from $T = 0$, with $\Delta t = 0.005$, without a limit on the number of Newton iterations. Figure 4.27 shows the same evolution in time of the pressure drop, but starting from time $T = 1$. The evolution in time of pressure drop for all 5 schemes is very similar. Figure 4.27 shows that the pressure drop becomes constant for all schemes at $T = 3.5s$.

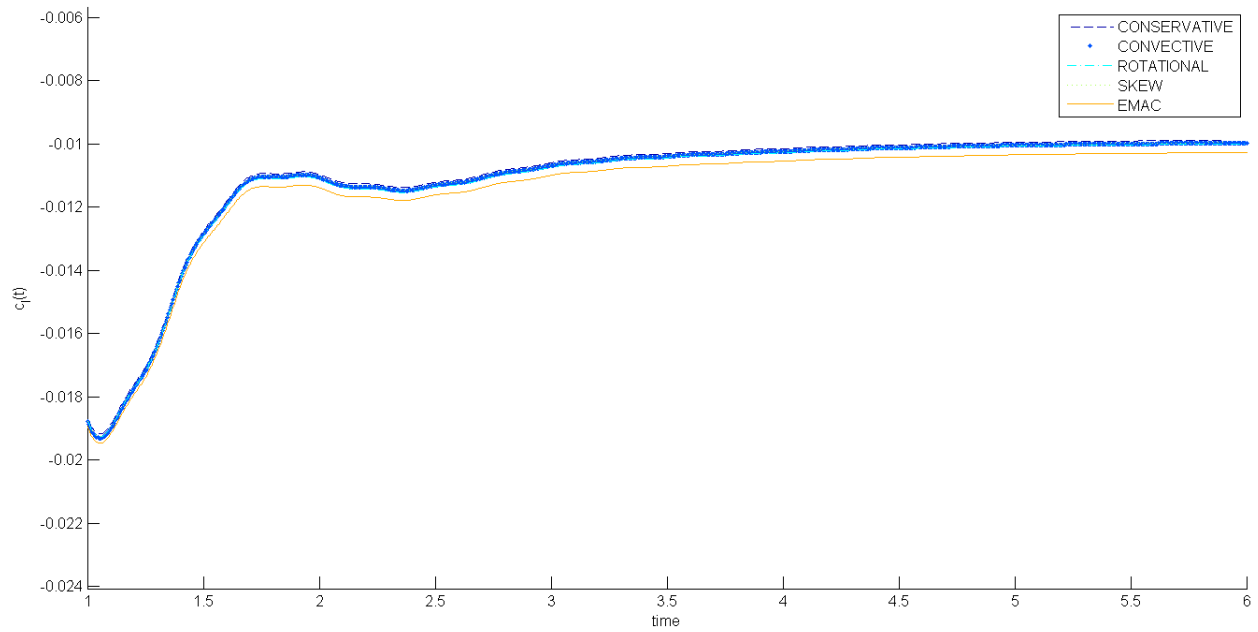


Figure 4.25: The lift coefficient for all 5 schemes, start time $T = 1$

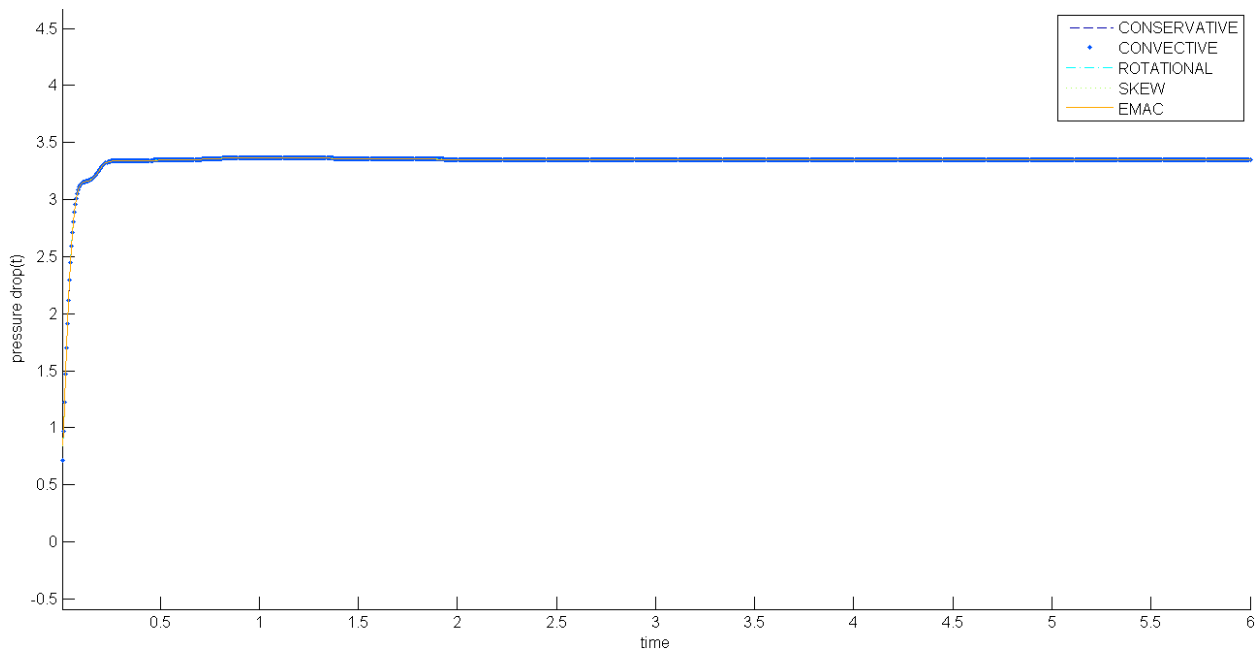


Figure 4.26: Pressure drop for all 5 schemes, start time $T = 0$

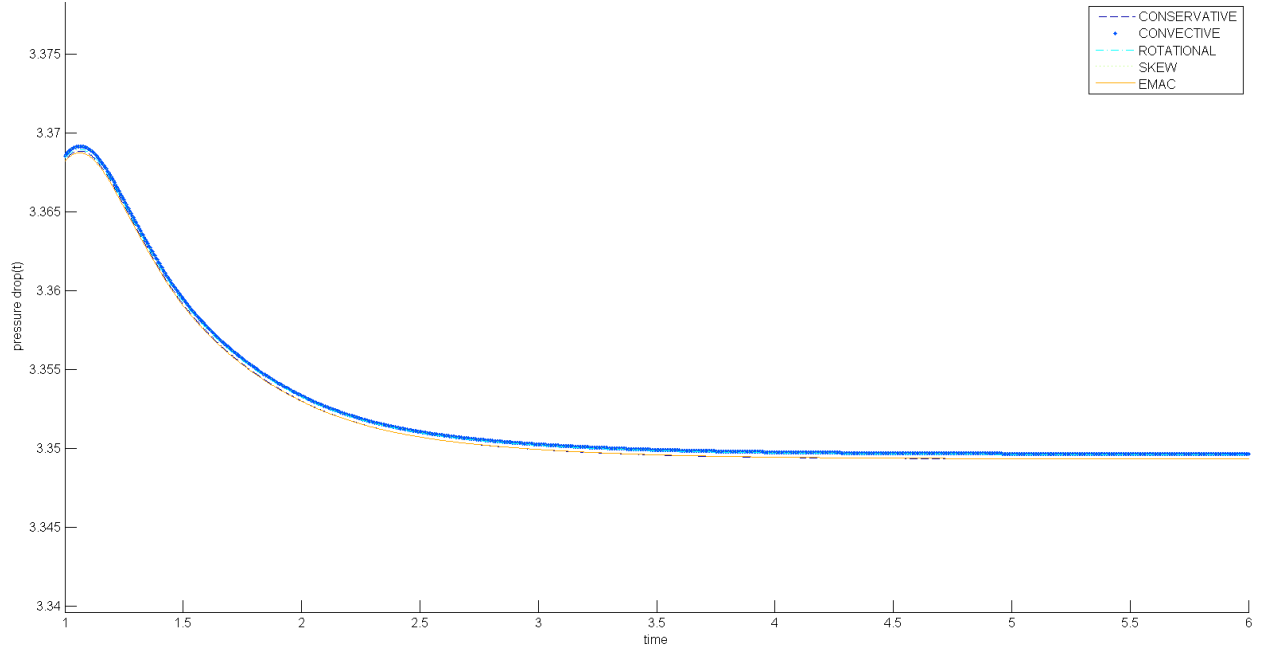


Figure 4.27: Pressure drop for all 5 schemes, start time $T = 1$

4.4.1.4 Charts

Next we collect and compare statistics for all 5 schemes on line figures. On figure 4.28 we show the drag coefficient for meshes with 2.29, 7.2 and 22.4 million degrees of freedom, and for all of EMAC, conservative, convective, rotational and skew-symmetric formulations. For each mesh the drag coefficient of all 5 formulations differs only within 0.02. With the increase of mesh degrees of freedom to 22.4, the interval for the drag coefficient for all 5 formulations decreases to under 0.01. The drag coefficient is almost the same for all schemes (for each particular mesh).

On figure 4.29 we show the maximum lift coefficient for meshes with 2.29, 7.2 and 22.4 million degrees of freedom, and for all of EMAC, conservative, convective, rotational and skew-symmetric formulations. The maximum lift coefficient is almost the same for each particular mesh for all formulations. The maximum lift coefficient changes only in the sixth digit with the increase of mesh degrees of freedom from 2.3 to 22.4 million.

On figure 4.30 we show maximum pressure drop for meshes with 2.29, 7.2 and 22.4 million degrees of freedom, and for all of EMAC, conservative, convective, rotational and skew-symmetric formulations. Reference values for pressure drop for flow past circular cylinder with constant inflow

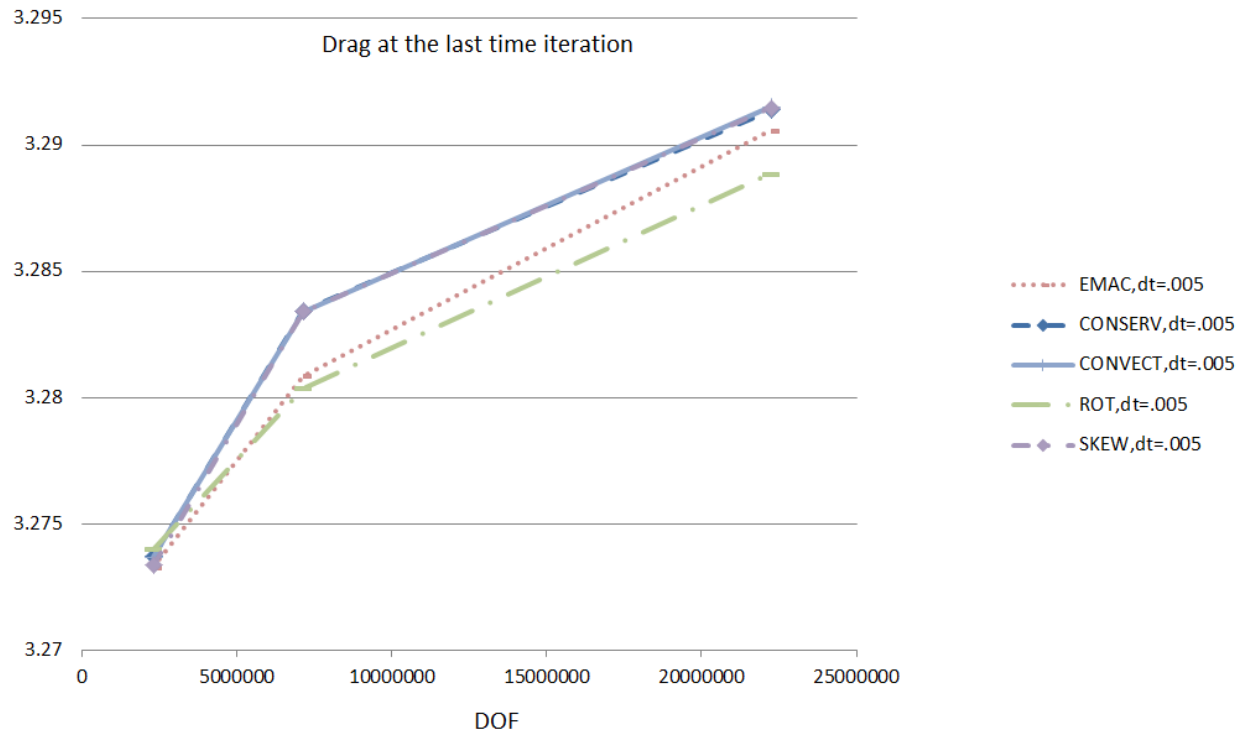


Figure 4.28: The drag coefficient for all 5 schemes at the last time iteration, for different meshes.

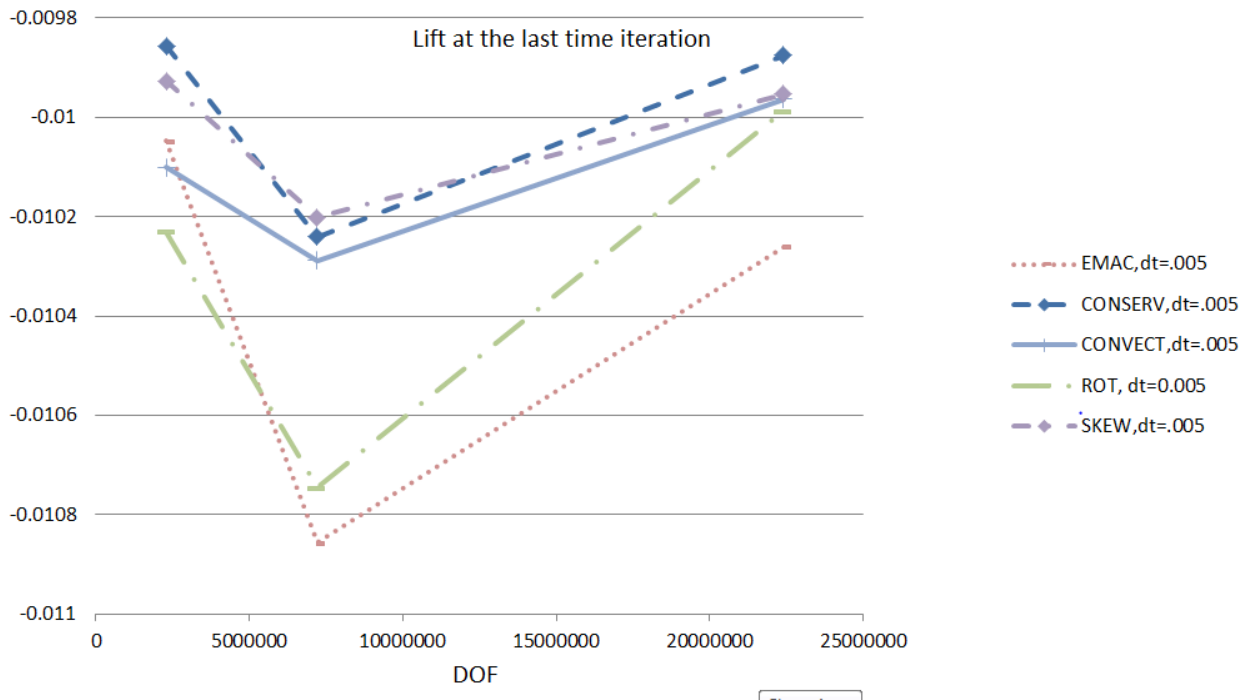


Figure 4.29: The lift coefficient for all 5 schemes at the last time iteration, for different meshes.

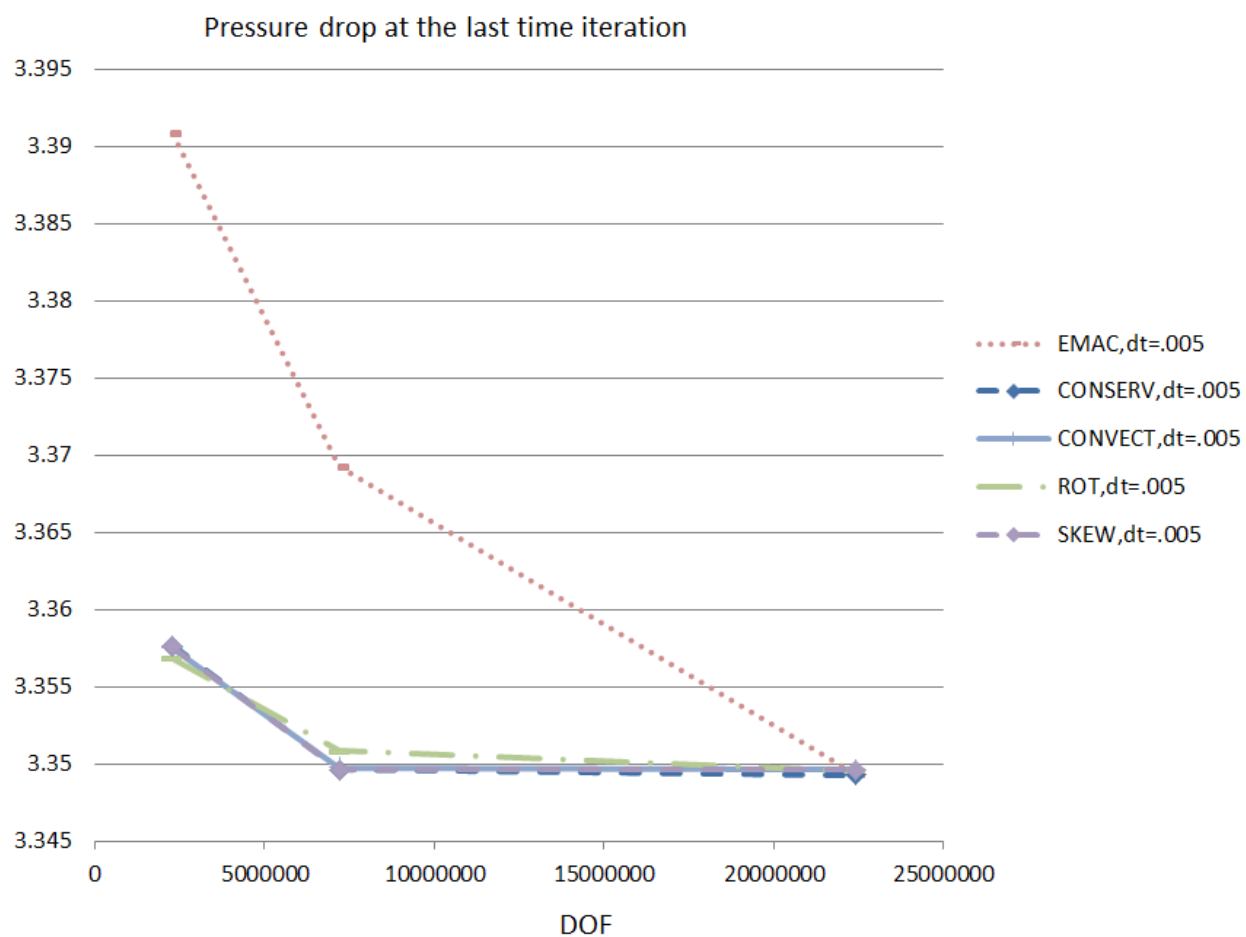


Figure 4.30: Pressure drop for all 5 schemes at the last time iteration, for different meshes.

are not found in the literature.

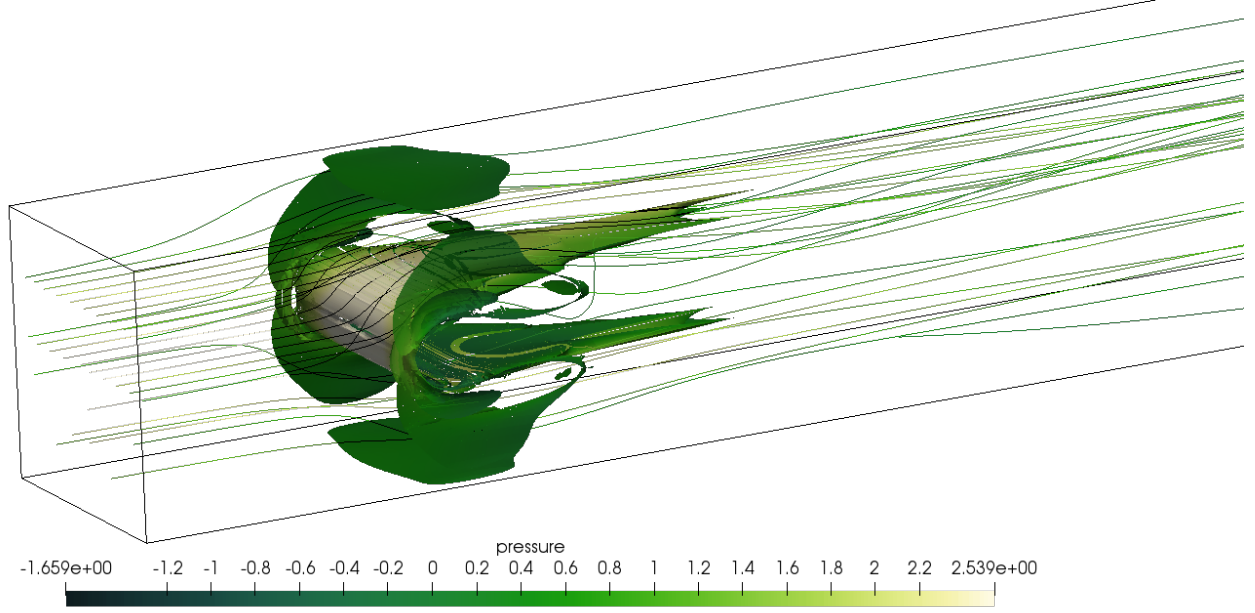


Figure 4.31: Vorticity iso-contours with streamlines at $T = 5$ sec for EMAC form. $\Delta t = 0.005$. Constant inflow.

Figure 4.31 shows iso-surfaces of vorticity magnitude in 3D together with streamlines that show trajectories of particles in time. Coloring is based on pressure. Iso-surfaces are chosen for the following vorticity magnitude values: 0, 54.625, 109.25, 163.875, 218.5, 273.125, 327.75, 382.375, 437, 491.625.

Figure 4.32 shows iso-surfaces of pressure in 3D at $T = 5$ sec for EMAC form with coloring based on velocity. Iso-surfaces are chosen for the following values of pressure: -1.698, -1.2237, -0.7495, -0.275.

Figure 4.33 shows magnitude of velocity iso-contours on midplane at $T = 5$ sec for EMAC form with coloring based on pressure. The midplane is passing through the center of the circular cylinder and is perpendicular to the axis of the cylinder. Iso-contours are chosen for the following values of velocity magnitude: 0.1975, 0.6708, 1.144, 1.617, 2.091, 0.1, 0.05, 0.02.

Figure 4.34 shows pressure iso-contours on midplane at $T = 5$ sec for EMAC form with coloring based on pressure, and $\Delta t = 0.005$. Iso-contours are chosen for the following values of pressure: -3.534, -2.812, -2.09, -1.37, -0.646, 0.075, 0.797, 1.519, 2.24, 2.96.

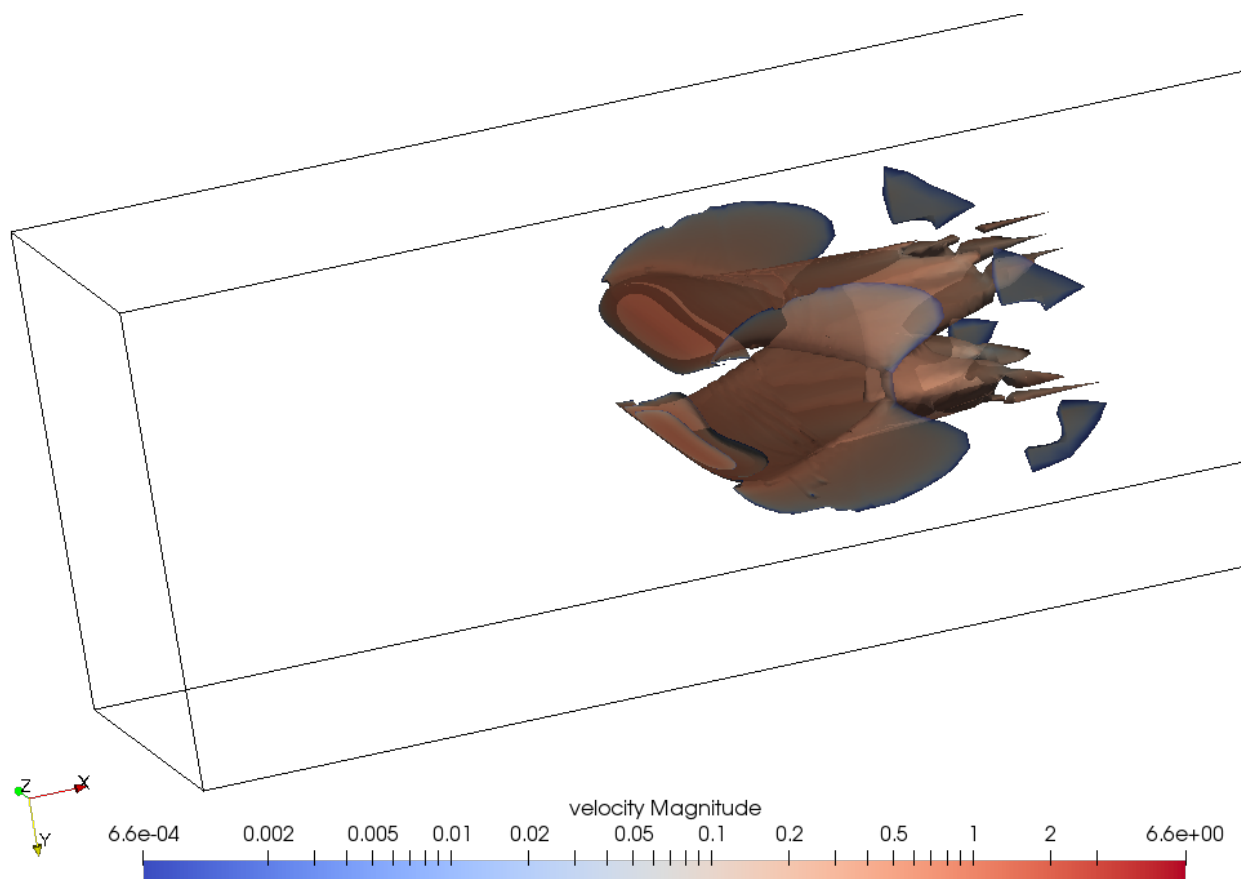


Figure 4.32: Pressure iso-contours in 3D. Constant inflow.

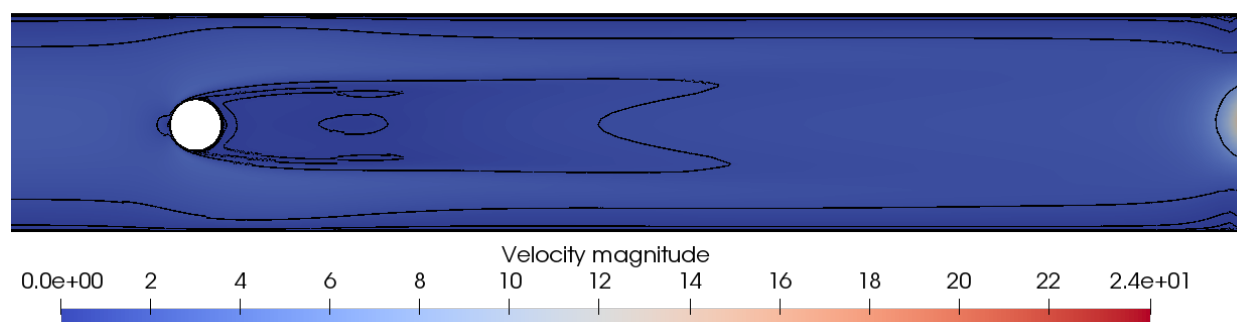


Figure 4.33: Velocity magnitude iso-contours on midplane at $T = 5$ sec. Constant inflow.

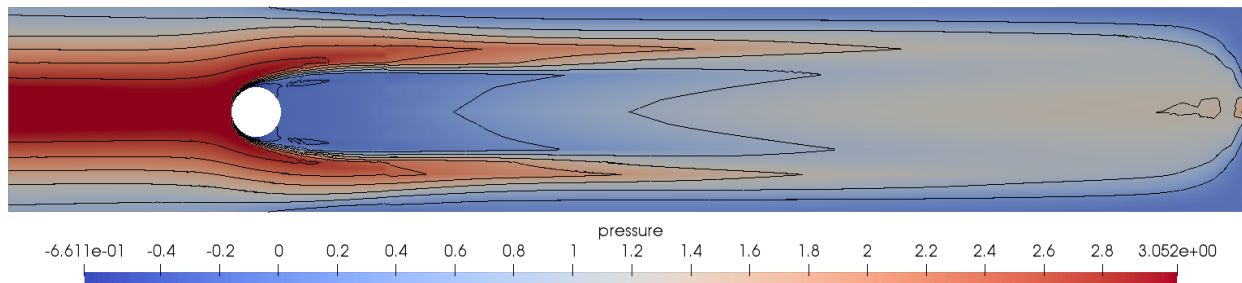


Figure 4.34: Pressure iso-contours on midplane at $T = 5$ sec.

4.4.2 Summary

We computed new and more precise reference values for $Re = 100$ problem for 3D channel flow past circular cylinder with constant inflow for drag and lift coefficient, and pressure drop. We compared the performance of EMAC, conservative, convective, rotational and skew-symmetric formulations for different meshes with up to 22.4 million degrees of freedom. EMAC formulation performed very similar to other formulations. Based on evolution in time figures of all of drag and lift coefficient, and pressure drop we conclude that fluid flow becomes stable/constant at about $T = 3.5s$, which indicates that $Re = 100$ with constant inflow is a stationary problem.

Statistics at the last time iteration	Interval
Drag	[3.2888, 3.2915]
Lift	[−0.0099, −0.0103]
Pressure drop	[3.349, 3.350]

Table 4.22: Interval obtained with 5 formulations, where the nonlinear problem is fully resolved at each time step. 22.4 million mesh DOF. $\Delta t = 0.005$.

We summarize the statistics obtained with the maximum space resolution with all of EMAC, conservative, convective, rotational and skew-symmetric formulations, and $\Delta t = 0.005$ as intervals in table 4.22. These statistics can be used for verification of new models and/or discretization schemes for the incompressible NSE. We note that the drag coefficient changes in the third digit when we increase space resolution of the mesh from 7.2 million to 22.4 million degrees of freedom.

Conclusions and Directions for Future Research

In chapter 2 of the present thesis we have computed reference values for a two-dimensional flow through a channel around a vertical flat plate obstacle with a time-independent inflow problem. New, more precise reference values for the averaged drag coefficient, recirculation length, and the Strouhal number have been derived from the computational results. These statistics have been verified by numerical computations with three time stepping schemes (BDF2, BDF3 and Crank-Nicolson). The same numerical simulations were carried out independently using deal.II and Freefem++ software and both gave very similar results. In addition both deal.II/ Q_2Q_1 and Freefem/ P_2P_1 element types were used to verify the results. For the same parameters, numerical simulations are carried out with several different meshes and different time step sizes. This allowed us to show convergence of statistics both with respect to spatial resolution and with respect to time step refinement.

In chapter 3 we have developed a new discrete formulation for the incompressible NSE, named the *EMA-conserving* (EMAC) formulation, which conserves energy, momentum, angular momentum, when the solenoidal constraint on the velocity is enforced only weakly. Moreover, we have shown that none of the commonly used *convective*, *conservative*, *rotational*, and *skew-symmetric* formulations conserve each of energy, momentum, and angular momentum (for a general finite element choice). Results of several numerical experiments have been provided which verify the discrete conservation properties of the EMAC scheme, and also show that it performs at least as good, or better, than the commonly used formulations. In chapter 3 we have used statistics obtained in chapter 2 to compare the performance of the novel EMAC scheme with 4 most commonly used formulations (rotational, skew-symmetric, convective and conservative). The EMAC formulation seems to significantly outperform all of rotational, skew-symmetric, conservative and convective formulations when the number of degrees of freedom is ‘relatively low’ (see Gresho problem in chapter 3 for example). ‘Relatively low’ of course depends on the dimension of the problem and on Reynolds number.

In section 4.3 of the present thesis we have computed reference values for three-dimensional channel flow past circular cylinder obstacle with **sin inflow**. We have studied numerically fully nonlinear schemes, which we linearized using Newton method. We also compared the performance of the EMAC scheme with 4 most commonly used formulations (rotational, skew-symmetric, convective and conservative) for three-dimensional channel flow past circular cylinder with time-dependent inflow problem. Statistics computed with time-dependent inflow and the EMAC formulation match very well with those found in the literature. In section 4.3 we also studied the performance of the EMAC formulation for 1, 2 and ‘as many as necessary’ number of Newton iterations. Interestingly, at most 2 Newton iterations required to achieve the required solution tolerance for the full nonlinear EMAC problem.

In section 4.4 we have computed reference values for three-dimensional channel flow past circular cylinder obstacle with **constant inflow**. Drag, lift and pressure drop obtained by numerical computations with the EMAC formulation for three-dimensional channel flow past circular cylinder problem are very similar to the corresponding statistics computed with rotational, skew-symmetric, convective and conservative formulations.

In all our numerical computations the EMAC formulation provides at least as accurate or better results than rotational, skew-symmetric, convective and conservative formulations.

Based on the above results, we conclude that the energy, momentum, angular momentum formulation/scheme (*EMAC*) is a very promising method and it should be studied further. It has been well-known for decades that more physically accurate schemes are more stable and accurate, especially over long times, and our computational study of the EMAC formulation indicates this is true here also.

For future research directions, we think it is necessary to carry out more numerical tests with the novel EMAC formulation, which has been developed in the present thesis. Our numerical simulations for three-dimensional flow past circular cylinder with constant inflow and Reynolds number 100 have showed that it results in a stationary flow (i.e. no vortices). We think it is important to perform numerical computations with a similar geometry but for unsteady (periodic) flows that generate vortices, for example numerical simulation of three-dimensional flow past circular

cylinder problem with a Reynolds number higher than 100. It is also an open question at which lowest Reynolds number this problem generates vortices.

All of our numerical computations with three-dimensional flows were carried out with grad-div stabilization term. We think it is necessary to carry out numerical computations with three-dimensional flows and without grad-div stabilization term, since it might show more difference between the performance of EMAC and the other four commonly used formulations. However this in its turn would require another linear solver, because the linear solver we use for three-dimensional simulations uses a preconditioner that requires the grad-div stabilization term.

In the present thesis we have showed that for the incompressible NSE our novel EMAC formulation conserves kinetic energy, linear and angular momentums. However many fluids cannot be described by the incompressible NSE. Therefore we believe a theoretical study of EMAC conservation properties in terms of physical quantities (kinetic energy, linear and angular momentums) for the incompressible NSE and/or fluids with variable density is needed also, which will likely result in a significant effort in analysis.

There is a need for numerical simulations and theoretical analysis of whether physical conservation laws hold in case of a non-Dirichlet boundary conditions for the EMAC formulation. Since non-Dirichlet boundary conditions usually means there is a fluid inflow/outflow, which in its turn affects such physical quantities as kinetic energy, linear and angular momentums. In this case, one would have to consider the conservation of more general physical quantities that take into account fluid inflow/outflow.

Our computational tests for the two-dimensional channel flow past vertical flat plate show that vertices appear with EMAC formulation for a Reynolds number lower than with the other commonly used formulations. We believe this fact is related to a better conservation properties of physical quantities of EMAC formulation. It would be interesting to determine the lowest Reynolds number at which vertices appear in three-dimensional flow past circular cylinder with constant inflow for all formulations of the NSE.

Another potential research direction is to study the performance of the EMAC formulation with turbulent flows. Numerical simulation of turbulent flows has always been a difficult area for

example due to the following. It was discovered by Kolmogorov in 1941 [30] (and further analyzed in [?]) that for large Reynolds numbers, the smallest stable eddy has length scale of order $O(Re^{-\frac{3}{4}})$. Therefore for a numerical simulation to capture the smallest possible eddy, one needs to choose a mesh with

$$\Delta x = \Delta y = \Delta z = O(Re^{-\frac{3}{4}}).$$

Hence the number of mesh points in a 3D simulation must be of order $Re^{9/4}$ in order to capture all the physics. Since turbulent flows have very high Reynolds number, such numerical computations are not feasible even on the current supercomputers. Therefore we think that the application of the EMAC formulation to turbulent flows is especially interesting due to the conservation properties of the EMAC formulation.

Bibliography

- [1] deal.II library web site. <https://www.dealii.org/>, October 2018.
- [2] FreeFem++ library web site. <http://www.freefem.org>, October 2018.
- [3] R.V. Abramov and A.J. Majda. Discrete approximations with additional conserved quantities: deterministic and statistical behavior. *Methods Appl. Anal.*, 10(2):151–190, 2003.
- [4] A. Arakawa. Computational design for long-term numerical integration of the equations of fluid motion: Two dimensional incompressible flow, Part I. *J. Comput. Phys.*, 1:119–143, 1966.
- [5] A. Arakawa and V. Lamb. A potential enstrophy and energy conserving scheme for the shallow water equations. *Monthly Weather Review*, 109:18–36, 1981.
- [6] D. Arnold and J. Qin. Quadratic velocity/linear pressure Stokes elements. In *Advances in Computer Methods for Partial Differential Equations VII*, pages 28–34. IMACS, 1992.
- [7] W. Bangerth, D. Davydov, T. Heister, L. Heltai, G. Kanschat, M. Kronbichler, M. Maier, B. Turcksin, and D. Wells. The deal.II library, version 8.4. *Journal of Numerical Mathematics*, DOI: 10.1515/jnma-2016-1045.
- [8] E. Bayraktar, O. Mierka, and S. Turek. Benchmark computations of 3D laminar flow around a cylinder with CFX, OpenFOAM and FeatFlow. *International Journal of Computational Science and Engineering*, 7(3):253–266, 2012.
- [9] M. Braack and T. Richter. Solutions of 3D Navier–Stokes benchmark problems with adaptive finite elements. *Computers & fluids*, 35(4):372–392, 2006.
- [10] S. Brenner and R. Scott. Series: Texts in applied mathematics. *The mathematical theory of finite element methods*, 15, 2008.
- [11] J. Cahouet and J-P. Chabard. Some fast 3D finite element solvers for the generalized Stokes problem. *International Journal for Numerical Methods in Fluids*, 8(8):869–895, 1988.
- [12] M. Case, V. Ervin, A. Linke, and L. Rebholz. A connection between Scott-Vogelius elements and grad-div stabilization. *SIAM Journal on Numerical Analysis*, 49(4):1461–1481, 2011.
- [13] Y. A. Cengel, A. J. Ghajar, and H. Ma. *Heat and Mass Transfer: Fundamentals & Applications*, 4e. McGraw-Hill, 2011.
- [14] S. Charnyi, T. Heister, M. A. Olshanskii, and L. G. Rebholz. Efficient discretizations for the EMAC formulation of the incompressible Navier-Stokes equations. *arXiv preprint arXiv:1712.00857*, 2017.
- [15] S. Charnyi, T. Heister, M. A. Olshanskii, and L. G. Rebholz. On conservation laws of Navier–Stokes Galerkin discretizations. *Journal of Computational Physics*, 337:289–308, 2017.

- [16] T. Davis. UMFPACK - an unsymmetric-pattern multifrontal method with a column pre-ordering strategy. *ACM Trans. Math. Software*, 30(204):196–199, 2004.
- [17] J. Evans and T.J.R. Hughes. Isogeometric divergence-conforming B-splines for the unsteady Navier-Stokes equations. *Journal of Computational Physics*, 241:141–167, 2013.
- [18] R. Falk and M. Neilan. Stokes complexes and the construction of stable finite element methods with pointwise mass conservation. *SIAM Journal on Numerical Analysis*, 51(2):1308–1326, 2013.
- [19] C. L. Fefferman. Existence and smoothness of the Navier-Stokes equation. *The millennium prize problems*, 57:67, 2006.
- [20] G. Fix. Finite element models for ocean circulation problems. *SIAM Journal on Applied Mathematics*, 29(3):371–387, 1975.
- [21] V. Girault and P.-A. Raviart. *Finite element methods for Navier-Stokes equations: theory and algorithms*. Springer-Verlag, 1986.
- [22] P. Gresho. On the theory of semi-implicit projection methods for viscous incompressible flow and its implementation via finite-element method that also introduces a nearly consistent mass matrix: Part 2: Applications. *Int. J. Numer. Methods Fluids*, 11:621–659, 1990.
- [23] M. D. Gunzburger. *Finite element methods for viscous incompressible flows: a guide to theory, practice, and algorithms*. Elsevier, 1989.
- [24] J. Guzmán and M. Neilan. Conforming and divergence-free Stokes elements in three dimensions. *IMA Journal of Numerical Analysis*, 34(4):1489–1508, 2013.
- [25] J. Guzman and M. Neilan. Conforming and divergence-free Stokes elements on general triangular meshes. *Mathematics of Computation*, 83:15–36, 2014.
- [26] T. Heister and G. Rapin. Efficient augmented Lagrangian-type preconditioning for the Oseen problem using grad-div stabilization. *International Journal for Numerical Methods in Fluids*, 71(1):118–134, 2013.
- [27] V. John. Higher order finite element methods and multigrid solvers in a benchmark problem for the 3D Navier-Stokes equations. *International Journal for Numerical Methods in Fluids*, 40(6):775–798, 2002.
- [28] V. John. Reference values for drag and lift of a two-dimensional time-dependent flow around a cylinder. *International Journal for Numerical Methods in Fluids*, 44(7):777–788, 2004.
- [29] V. John. On the efficiency of linearization schemes and coupled multigrid methods in the simulation of a 3D flow around a cylinder. *Int. J. Numer. Methods Fluids*, 50:845–862, 2006.
- [30] A. N. Kolmogorov. The local structure of turbulence in incompressible viscous fluid for very large Reynolds numbers. In *Dokl. Akad. Nauk SSSR*, volume 30, pages 301–305. JSTOR, 1941.
- [31] W. Layton. *An Introduction to the Numerical Analysis of Viscous Incompressible Flows*. SIAM, Philadelphia, 2008.

- [32] W. Layton, C. Manica, M. Neda, and L. Rebholz. The joint helicity-energy cascade for homogeneous, isotropic turbulence generated by approximate deconvolution models. *Advances and Applications in Fluid Mechanics*, 4(1):1–46, 2008.
- [33] C. Lehrenfeld and J. Schöberl. High order exactly divergence-free hybrid DG methods for unsteady incompressible flows. *Computer Methods in Applied Mechanics and Engineering*, 307:339–361, 2016.
- [34] R. Liska and B. Wendroff. Comparison of several difference schemes on 1D and 2D test problems for the Euler equations. *SIAM Journal on Scientific Computing*, 25:995–1017, 2003.
- [35] J. Liu and W. Wang. Energy and helicity preserving schemes for hydro and magnetohydrodynamics flows with symmetry. *J. Comput. Phys.*, 200:8–33, 2004.
- [36] M. Marion and R. Temam. Navier-Stokes equations: Theory and approximation. *Handbook of Numerical Analysis*, VI:503–688, 1998.
- [37] F. Najjar and S. Vanka. Simulations of the unsteady separated flow past a normal flat plate. *International journal for numerical methods in fluids*, 21(7):525–547, 1995.
- [38] K. D. Nikitin, M. A. Olshanskii, K. M. Terekhov, Y. V. Vassilevski, and R. Yanbarisov. An adaptive numerical method for free surface flows passing rigidly mounted obstacles. *arXiv preprint arXiv:1609.05423*, 2016.
- [39] M. Olshanskii and A. Reusken. Grad-div stabilization for Stokes equations. *Math. Comp.*, 73(248):1699–1718, 2004.
- [40] M.A. Olshanskii and L.G. Rebholz. A note on helicity balance of the Galerkin method for the 3D Navier–Stokes equations. *Computer Methods in Applied Mechanics and Engineering*, 199:1032–1035, 2010.
- [41] A. Palha and M. Gerritsma. A mass, energy, enstrophy and vorticity conserving (MEEVC) mimetic spectral element discretization for the 2D incompressible Navier-Stokes equations. *Submitted*, 2016.
- [42] N. A. Phillips. An example of non-linear computational instability. *The Atmosphere and the Sea in motion*, 501, 1959.
- [43] L. G. Rebholz. An energy-and helicity-conserving finite element scheme for the Navier-Stokes equations. *SIAM Journal on Numerical Analysis*, 45(4):1622–1638, 2007.
- [44] Y. Saad. *Iterative methods for sparse linear systems*, volume 82. SIAM, 2003.
- [45] A. K. Saha. Far-wake characteristics of two-dimensional flow past a normal flat plate. *Physics of Fluids (1994-present)*, 19(12):128110, 2007.
- [46] A. K. Saha. Direct numerical simulation of two-dimensional flow past a normal flat plate. *Journal of Engineering Mechanics*, 139(12):1894–1901, 2013.
- [47] R. Salmon. A general method for conserving energy and potential enstrophy in shallow-water models. *Journal of the Atmospheric Sciences*, 64(2):515–531, 2007.

- [48] R. Salmon and L.D. Talley. Generalizations of Arakawa's Jacobian. *J. Comput. Phys.*, 83:247–259, 1989.
- [49] M. Schäfer, S. Turek, F. Durst, E. Krause, and R. Rannacher. *Benchmark computations of laminar flow around a cylinder*. Springer, 1996.
- [50] M. Schäfer and S. Turek. The benchmark problem 'flow around a cylinder' flow simulation with high performance computers II. in *E.H. Hirschel (Ed.), Notes on Numerical Fluid Mechanics*, 52, Braunschweig, Vieweg:547–566, 1996.
- [51] H. Sohr. *The Navier-Stokes equations: An elementary functional analytic approach*. Springer Science & Business Media, 2012.
- [52] C. Sorgentone, S. La Cognata, and J. Nordstrom. A new high order energy and enstrophy conserving Arakawa-like Jacobian differential operator. *Journal of Computational Physics*, 301:167–177, 2015.
- [53] S. Ray T. Tezduyar, S. Mittal and R. Shih. Incompressible flow computations with stabilized bilinear and linear equal order interpolation velocity-pressure elements. *Computer Methods in Applied Mechanics and Engineering*, 95:221–242, 1992.
- [54] C. Taylor and P. Hood. A numerical solution of the Navier-Stokes equations using the finite element technique. *Computers and Fluids*, 1(1):73 – 100, 1973.
- [55] R. Temam. *Navier-Stokes equations*. Elsevier, North-Holland, 1991.
- [56] S. Turek. *Efficient Solvers for Incompressible Flow Problems: An Algorithmic and Computational Approache*, volume 6. Springer Science and Business Media, 1999.
- [57] S. Zhang. A new family of stable mixed finite elements for the 3D Stokes equations. *Mathematics of Computation*, 74:543–554, 2005.